Memoirs of the Faculty of Engineering, Nagoya University
Vol.42, No.1 (1990)

SOLID STATE CHEMISTRY OF NUCLEAR REACTOR MATERIALS AT HIGH TEMPERATURE

Keiji NAITO, Toshihide TSUJI, Tsuneo MATSUI and Masaaki MAGARA

Department of Nuclear Engineering

(Received May 31,1990)

Abstract

A review on the studies of the solid state chemistry of nuclear materials at high temperatures carried out in our laboratory since 1968 is given. The studies contain several aspects of research; studies on phase equilibria and defect structures, diffusion, chemical reaction and calorimetry.

Phase equilibria and defect structures were studied on many material systems; $UO_{2\pm x}$ and doped $UO_{2\pm x}$, $U_4O_{9\pm y}$, U_3O_{8-z}, $(U,Pu)O_{2+x}$ and $PuO_{2\pm x}$, $(U,Th)O_{2+x}$, Nd_2O_{3+x}, *Pr-O* system, *Nb-O* system, *V-O* system, TiO_x solid solution, $Cr_2O_{3\pm x}$, MoO_2 and MoO_3, $MnFe_2O_{4\pm x}$, $Cu_{1-x}Ni_xCr_2O_4$, $Ba_2YCu_3O_{7-x}$, Th_3N_4 and Th_2N_2O, *U-Zr* and *U-Mo* alloys, *Mo-Ru-Pd(Rh)* alloys, *Pd-Zr* alloy.

Diffusion studies were made by using several methods; tracer sectioning method, Mössbauer line-broadening methods, thermogravimetric and electrochemical relaxation method, etc. The self-diffusion coefficients were measured for iron and cobalt in *Cr*-doped hematite and magnetite, iron in $Fe_{1-x}S$, iron in iron tellurides. The chemical diffusion coefficients were measured for oxygen in $(Th,U)O_{2+x}$, niobium vacancy in $Nb_{1-x}O_2$ and oxygen in $Ba_2YCu_3O_{7-x}$.

Some oxidation reactions were investigated for *UC*, iron base alloys and noble metal alloys, and reaction between iron base allay and tellurium was also studied. Crystal growth of UO_{2+x}, $(U,Th)O_2$ and $ThSiO_4$ by means of chemical transport reaction and that of *ZrC* by chemical vapor deposition are also discussed.

Contents

I. Introduction

The nuclear power plant is designed so as to have a good performance at high temperatures, since the thermal efficiency is increased as temperature increases. The materials, however, become unstable and reactive at high temperatures, and then may results in the failure of integrity of the materials. It is recognized that the knowledge of materials chemistry at high temperature is of much importance in the research and development of nuclear power reactors.

The study on the solid state chemistry of several kinds of materials at high temperatures has been carried out extensively in our laboratory since 1968. The study includes some aspects of research such as phase equilibrium and defect structure, calorimetry, diffusion, chemical reaction, etc.

The present paper is prepared to review these research activities of our laboratory during the past about twenty years, which were made by the collaboration with many colleagues and students. We have already published a review on calorimetric study in our laboratory from point of similar view in this Memoirs in 1983.[1] Hence, the description of the calorimetric studies before 1983 is not given in this review to avoid overlapping but just take note of the original publications.

II. Studies on phase equilibria

2. 1. Apparatus and method

An apparatus used for the studies on the phase equilibria of some oxides is shown schematically in Fig. 1. The oxygen partial pressures were prepared mainly by the gas mixture methods: the Ar/O_2 or CO_2/H_2 (or CO_2/CO) mixing ratio was adjusted by using calibrated flowmeters; the former is called the direct gas control and the latter the buffer gas control methods. However, there are two regions of oxygen partial pressure where the control by the gas mixture method is difficult; one is a region between the direct gas control (Ar/O_2) and the buffer gas control (CO_2/H_2) regions (10^{-10}-10^{2} *Pa* at 1023 K), and the other is a very low oxygen partial pressure region below the buffer gas control region ($<10^{-20}$ *Pa* at 1023 K). The precise method for controlling two oxygen partial pressure regions mentioned above was developed in our laboratory by using a stabilized zirconia cell[2-4] as shown in Fig. 2. The control of very low oxygen partial pressures in the range of 10^{-21}-10^{-24} *Pa* at 1023 K[2] and that of intermediate range from 10^{-1} to 10^{2} *Pa*[2,3] were obtained by pumping oxygen with a stabilized zirconia cell into the purified hydrogen and argon stream, respectively.

The determination of oxygen partial pressure in the resulting mixture was also developed in our laboratory and carried out by measuring the electrical resistance of nonstoichiometric cobaltous oxide[4-6] ($Po_2 = 10^{5}$-10^{-6} *Pa* at 1273 K) and barium titanate[4-6] ($Po_2 = 10^{-10}$-10^{-17}

Pa at 1273 K) in high and low oxygen partial pressure ranges as shown in Figs. 3 and 4, respectively.

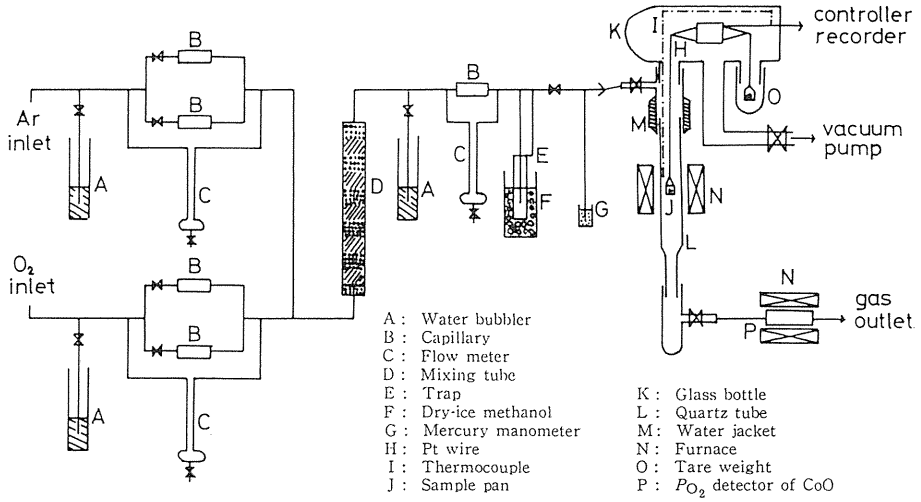

Fig. 1 Apparatus used for the studies on the phase equilibria of some oxides.

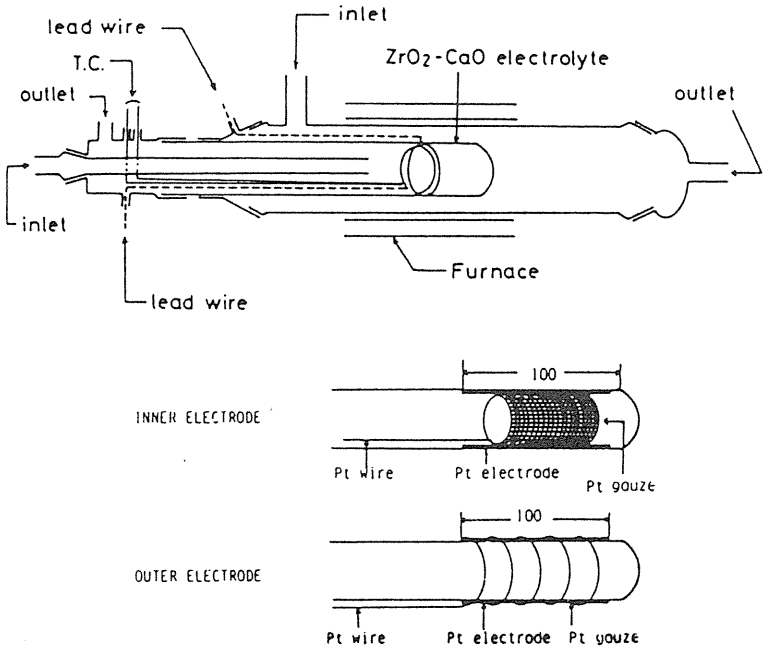

Fig. 2 The solid electrolyte oxygen pump and the electrode assembly[2].

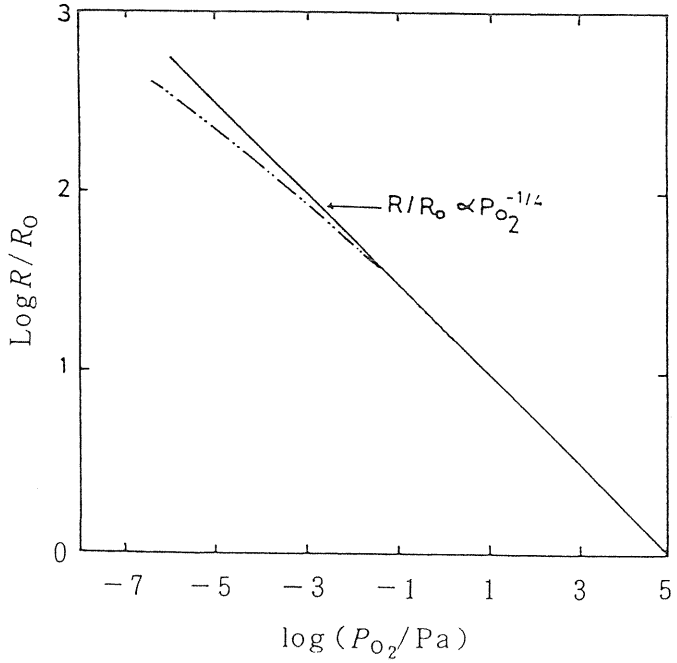

Fig. 3 Relation between log R/Ro and log Po_2 at 1273 K for $Co_{1-x}O$ (—— wire; —··— pellet)[5].

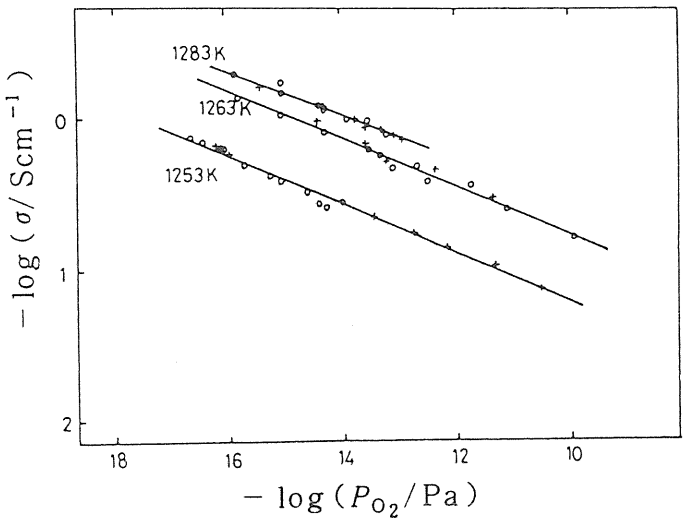

Fig. 4 Electrical conductivity of non-stoichiometric barium titanate versus oxygen partial pressure at 1253, 1263 and 1283 K[6].

The gravimetric measurement was made with a Cahn RG automatic electromicrobalance to determine the weight change of the sample. The electrical conductivity was carried out by the conventional inserted wires method[7]. High and room temperature X-ray diffractometries were used for the determination of lattice parameter and for the identification of the phase.

The vapor pressures were measured using a time-of-flight mass spectrometer (CVC model MA-2) equipped with Knudsen cell in a tungsten holder heated by electron bombardment and the details of equipment have been described elsewhere[1].

Heat capacity measurement was carried out by using an adiabatic scanning calorimeter which was developed in our laboratory and described in detail elsewhere[1,8].

Electromotive force measurements for determining thermodynamic properties of Nb_2O_{5-x} were carried out by the following galvanic cell[9]

Nb_2O_{5-x} | solid electrolyte | air

The cell system is schematically shown in Fig. 5. A calcia (or yttria) stabilized zirconia tube (ZrO_2+15 mol% CaO (or Y_2O_3)) with a flat closed end was used, as the solid electrolyte.

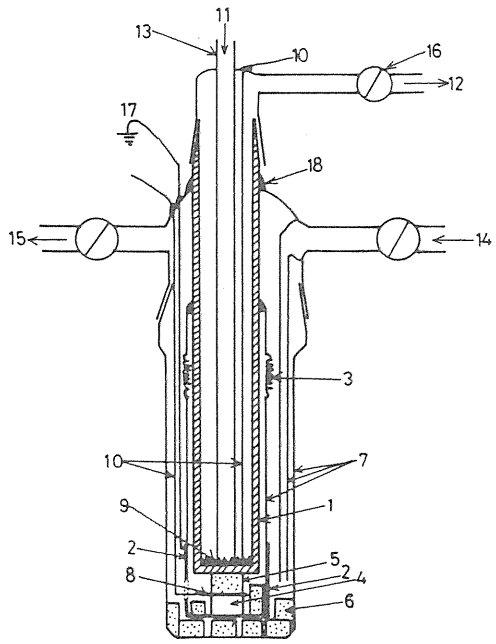

Fig. 5 Schematic diagram of the galvanic cell assembly (1) solid electrolyte tube, (2) *Pt* cover, (3) spring (4) quartz pellet, (5) sample pellet, (6) pellets for oxygen getter, (7) quartz tube, (8) *Pt* foil, (9) *Pt* paste and gauze, (10) *Pt* lead wire, (11) air inlet, (12) air outlet, (13) alumina tube, (14) *Ar* inlet, (15) *Ar* outlet, (16) glass stopcock, (17) ground, (18) araldite seal[91].

2. 2. *Phase equilibria and defect structures*

2. 2. 1. *U-Osystem*

Uranium dioxide is now widely used as nuclear fuel, and many studies have been carried out on the *U-O* system[10]. Fig. 6[11] shows the phase diagram of the *U-O* system. As seen in the figure, many phases exist in this system and each phase has a propensity to become non-stoichiometric in composition.

(a) $UO_{2\pm x}$ and doped $UO_{2\pm x}$[12,13]

(1) Oxygen potential vs. O/M

The oxygen potential, $\Delta\overline{Go}_2 = RT\ ln\ Po_2$, where Po_2 is the oxygen partial pressure, is one of the most important basic properties of oxide fuel, since the magnitude of the oxygen potential of the fuel determines the behavior of fission products and the occurrence of the reactions in the fuel pin.

The oxygen potentials at about 1280 K of $UO_{2\pm x}$ doped with various cations are shown against the O/M (M: U+other metal) ratio in Fig. 7[13], where the dopant concentrations are limited to be as low as possible, say about 1 % to make the effect by doping clear. It is seen from the figure that the oxygen potentials of $UO_{2\pm x}$ doped with cations of lower valency than

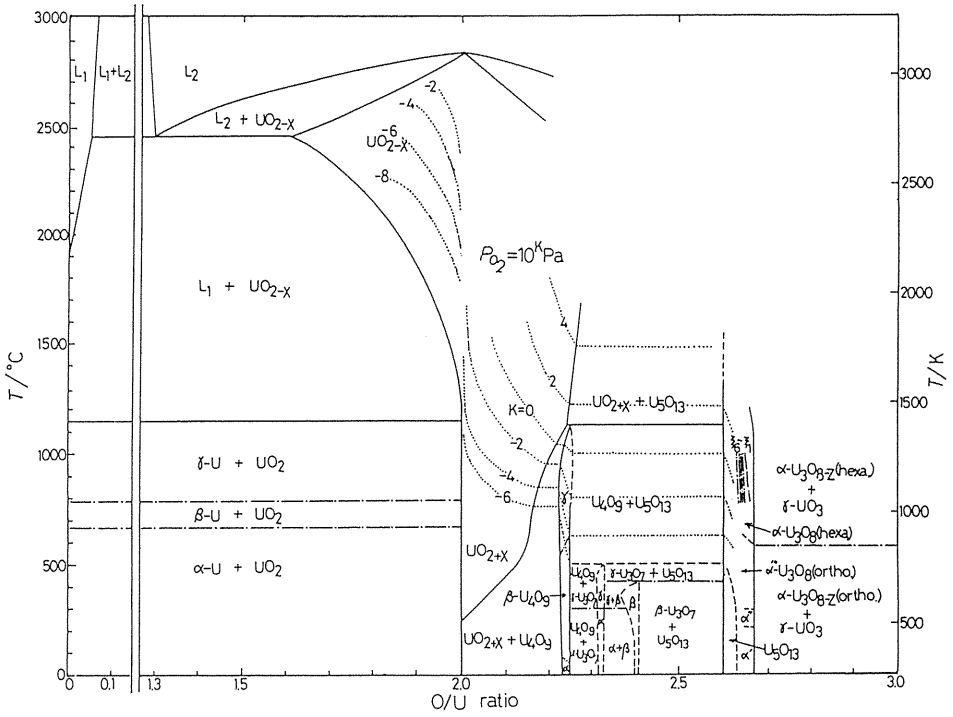

Fig. 6 Phase diagram of the *U-O* system[11].

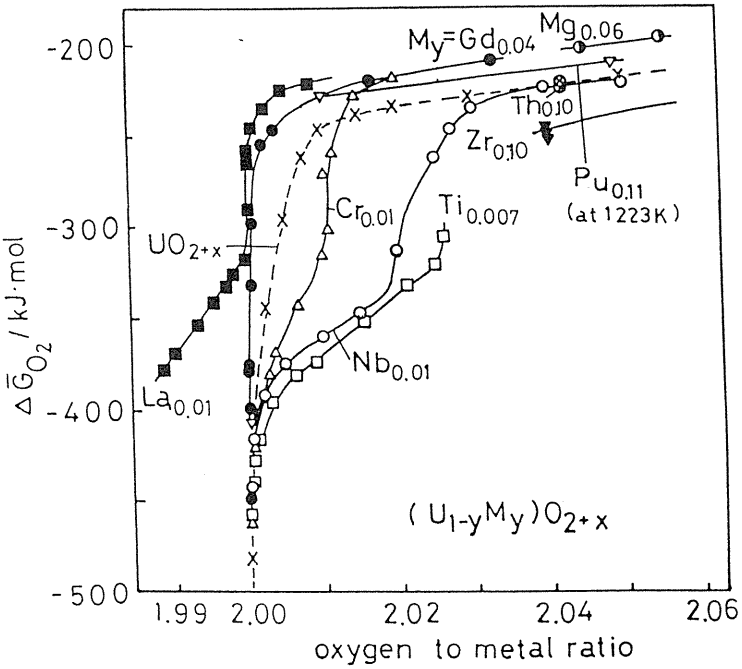

Fig. 7 Oxygen potential ($\triangle \bar{G}o_2$) vs. oxygen-to-metal ratio for $(U_{1-y}M_y)O_{2+x}$ at about 1282 K[12].

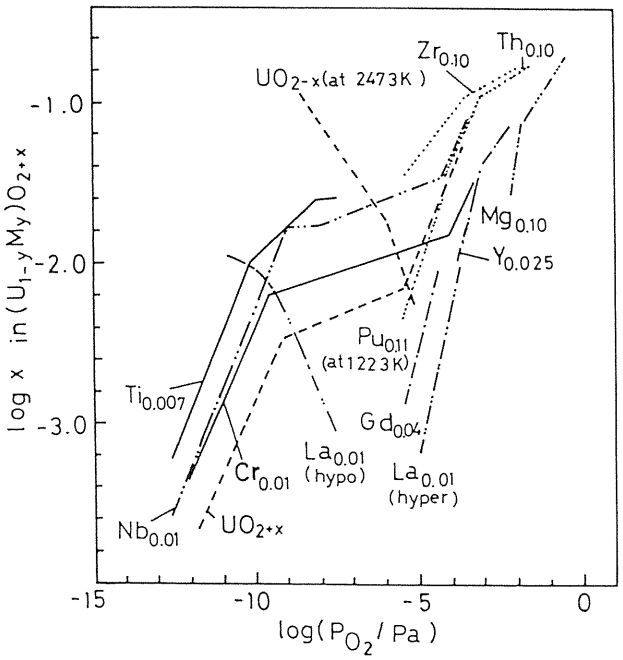

Fig. 8 Dependence of x on Po_2 for $U_{1-y}M_y\ O_{2+x}$ at about 1282 K.

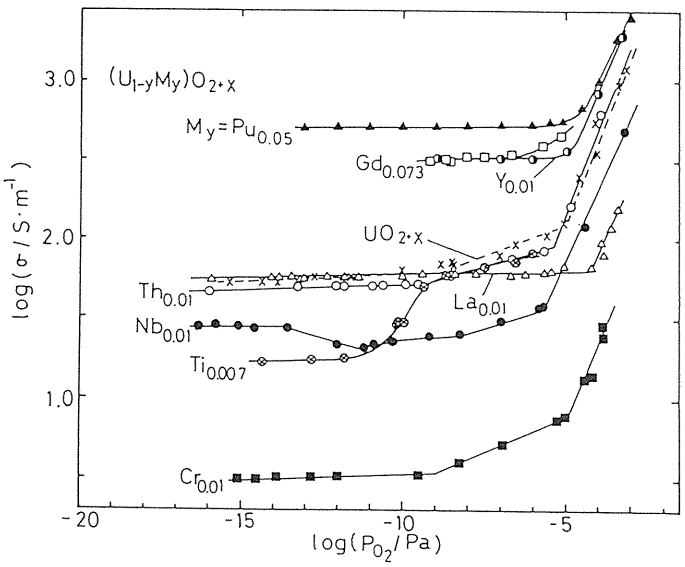

Fig. 9 Dependence of the electrical conductivity (σ) on oxygen partial pressure (Po_2) for $(U_{1-y}M_y)O_{2\pm x}$ at about 1282 K.

the uranium ion (such as La[14], Gd[15], Mg[16]) are higher than that of undoped $UO_{2\pm x}$, and those with cations of higher valency (such as Nb[17], Cr[18]) are lower than that of undoped $UO_{2\pm x}$.

These features are explained, to a first approximation, from the valence control rule, assuming that these metal ions are present as the substitutionals for uranium ions; the doping with the metal ions of lower (higher) valency induces the increase (decrease) in the oxidation state of the remaining uranium ions after substitution of the dopant ions for uranium ions by the electric charge compensation, which leads to the increase (or decrease) of the oxygen potential.

In the case of doping with homovalent (tetravalent) cations (such as Th[19], Zr[20], Pu[21]), the oxygen potentials at high O/U ratio (with large x) are nearly equal to that of undoped UO_{2+x}, as expected by the valence control rule. However, the lower oxygen potential of UO_{2+x} doped with Ti ions[22] than that of UO_{2+x} can not be interpreted by the substitutional model, but may be explained by assuming the Ti^{4+} interstitials as the predominant defects. Similarly the lower oxygen potential observed in the case of UO_{2+x} doped with Cr ion may have the possibility to be interpreted by assuming the Cr^{3+} interstitials instead of the Cr^{6+} substitutionals for uranium ions.

(2) Defect structure[12,13]

The oxygen partial pressure (Po_2) dependence of the departure from stoichiometric composition (x) and the electrical conductivity (σ) for $MO_{2\pm x}$ are usually expressed as $x \propto Po_2^{1/n}$ and $\sigma \propto Po_2^{1/n'}$, respectively.

Log x vs. log Po_2[12,13,23] and log σ vs log Po_2[12,13,23] for pure UO_2 and doped $UO_{2\pm x}$ at about 1280 K are shown in Figs. 8 and 9, respectively. The values of n for UO_{2+x} are observed from Fig. 8 as 2, 12 and 2 in turn from the low oxygen partial pressure for three oxygen partial pressure regions. The oxygen partial pressure dependences of x for UO_{2+x} doped with various cations are similar to those of undoped $UO_{2\pm x}$, indicating the presence of the similar defect structures in the doped $UO_{2\pm x}$ to those of undoped $UO_{2\pm x}$.

The values of n' for UO_{2+x} are seen from Fig. 9 as ∞, 12 and ∞ in turn from the low oxygen partial pressure, which corresponds to the relation between x and Po_2. Similar relationships between σ and Po_2 hold for doped $UO_{2\pm x}$ as seen from Fig. 9.

For pure UO_{2+x}, the oxygen partial pressure dependences $n=n'=2$ observed from x-Po_2 and σ-Po_2 relations in the relatively high oxygen partial pressure region are interpreted by the following defect formation reaction, using the Kröger-Vink notation[24]:

$$2V_i^a + 2V_i^b + 2O_o + O_2(g) = \{2(O_i^a O_i^b V_o)\}^{m'} + mh^{\cdot} \quad , \tag{1}$$

where $h^{\cdot}$ is a hole and m' is the charge of the complex defect. Taking the value $m=1$ in eq. (1), one obtains $n=n'=2$.

The values $n=n'=12$ observed in the intermediate oxygen partial pressure region can be explained by the reaction:

$$2V_i^a + 2V_i^b + 2O_o + 1/2O_2(g) = (2O_i^a O_i^b 2V_o)^{m'} + mh^{\cdot} \quad . \tag{2}$$

Taking $m=5$ in eq. (2), one obtains $n=n'=12$.

The values $n=2$ and $n'=\infty$ in the low oxygen partial pressure region can be explained by taking $m=0$ in eq. (2).

For the defect structure of hypostoichiometric $(U,La)O_{2-x}$[14], the following reactions are assumed:

$$2O_i^a + O_i^b + 2V_o = (2V_o^a V_o^b 2O_i)^{\cdot} + e' + 1/2O_2(g) \tag{3}$$

and

$$2O_i^a + 2O_i^b + 2O_o = \{2(V_o^a V_o^b O_i)\}^{\cdot} + e' + O_2(g) \ , \qquad (4)$$

where e' is the electron. The dependences $n=-2$ and $n'=\infty$ in the low oxygen partial pressure region can be derived from eq. (3) and the relation $[e'] \simeq$ constant. The values $n=-1$ and $n'=\infty$ can be explained from eq. (4) and the relation $[e'] \simeq$ constant.

In the case of $(U,Ti)O_{2+x}$[22], assuming the interstitial model rather than the substitutional one, the following reaction can be considered:

$$Ti^x + 1/2O_2(g) + 2V_i^a + V_i^b + 2O_o = \{(2O_i^a O_i^b 2V_o)^{m'} Ti^{4\cdot}\}^{q'} + qh^{\cdot} \ , \qquad (5)$$

where Ti^x is the neutral titanium in interstitial position and q' is the charge of the complex defect. The dependences $n=2$ and $n'=\infty$ in the low oxygen partial pressure region can be interpreted from eq. (5) by assigning the value $m=4$ and $q=0$ and by using the electrical neutrality condition $[e'] \simeq [h^{\cdot}] \simeq$ constant. The values $n=n'=4$ in the intermediate oxygen partial pressure region can be interpreted from eq. (5) by assuming $m=5$ and $q=1$. The oxygen partial pressure dependence $n=n'=\infty$ in the high oxygen partial pressure region is explained by using eq. (5) and the electroneutrality condition $[Ti_i^x]=[(2O_i^a O_i^b 2V_o)^{5'} Ti_i^{4\cdot}]'=[h^{\cdot}]$=constant.

Table 1 Defect structures for UO_{2+x} and $(U, M)O_{2+x}$ (M = metal) in the temperature range between 1173 and 1373 K[12].

phase	Po_2 region	$x \propto Po_2^{1/n}$ n value	$\sigma \propto Po_2^{1/n'}$ n' value	defect model	main neutrality conditions
UO_{2+x}	high	2	2	$(2(O_i^a O_i^b Vo))'$	$[h^{\cdot}]=[(2(O_i^a O_i^b Vo))']$
	intermediate	12	12	$(2O_i^a O_i^b 2Vo)^{5'}$	$[h^{\cdot}]=5[(2O_i^a O_i^b 2Vo)^{5'}]$
	low	2	very large	$(2O_i^a O_i^b 2Vo)^{x}$	$[h^{\cdot}]=[e']$
$(U,La)O_{2+x}$	high	2	2	$(2(O_i^a O_i^b Vo))'$	$[h^{\cdot}]=[(2(O_i^a O_i^b Vo))']$
	intermediate	1	very large	$(2(O_i^a O_i^b Vo))'$	$[h^{\cdot}]=[La_U^{\cdot}]$
$(U,La)O_{2-x}$	low	-1 ~ -2	very large	$(2(V_o^a V_o^b O_i))'$ or $(2V_o^a V_o^b 2O_i)^{\cdot}$	$[h^{\cdot}]=[La_U^{\cdot}]$
$(U,Nb)O_{2+x}$	high	2	2	$(2(O_i^a O_i^b Vo))'$	$[h^{\cdot}]=[(2(O_i^a O_i^b Vo))']$
	intermediate	12	12	$(2O_i^a O_i^b 2Vo)^{5'}$	$[h^{\cdot}]=5[(2O_i^a O_i^b 2Vo)^{5'}]$
	low	very large	±10	$(2O_i^a O_i^b 2Vo)^{5'}$	$[Nb_U^{\cdot}]=5[(2O_i^a O_i^b 2Vo)^{5'}]$
	very low	2	very large	neutral defect or $(2O_i^a O_i^b 2Vo)^{5'}$	$[Nb_U^{\cdot}]=[e']$
$(U,Ti)O_{2+x}$	high	very large	very large	$[(2O_i^a O_i^b 2Vo)^{5'} Ti_i^{4\cdot}]']$	$[h^{\cdot}]=[((2O_i^a O_i^b 2Vo)^{5'} Ti_i^{4\cdot})']$ $=Ti_i^x$
	intermediate	4	4	$[(2O_i^a O_i^b 2Vo)^{5'} Ti_i^{4\cdot})']$	$[h^{\cdot}]=[((2O_i^a O_i^b 2Vo)^{5'} Ti_i^{4\cdot})']$
	low	2	very large	$[(2O_i^a O_i^b 2Vo)^{4'} Ti_i^{4\cdot})^{x}]$	$[h^{\cdot}]=[e']$

The results are summarized as shown in Table 1[12]. Schematic diagram of the relationship between the relative concentration of defects and Po_2 for $UO_{2\pm x}$ and $(U,M)O_{2\pm x}$ is shown by the authors.[12]

(3) Heat Capacity of UO_2[25]

The origin of anomalous rise of heat capacity of UO_2 above about 1500 K has been the subject of the discussion by many investigators.[25] One is due to the formation of Frenkel defects of oxygens and the other the formation of electron-hole pairs.

The heat capacities of UO_2 doped with Gd[26,27] and La[28] of the concentration from 4.4 to 14.2 mol% are shown in Fig. 10[27,28]. It was observed that anomalous increase in the heat capacity begins at lower temperature than undoped UO_2: the onset temperature decreases with increasing Gd and La contents. Since no anomaly in the electrical conductivity curve was found[25,26] around the onset temperature found in the heat capacity curve, it is not likely that the excess heat capacity of doped UO_2 is due to the formation of electron-hole pairs. The fact that the onset temperature of doped UO_2 decreases as the Gd and La contents increase may indicate that the excess heat capacity of doped UO_2 is due to the formation of atomic defect because the defects concentration increases as the Gd and La contents increase. By doping trivalent cations such as La^{3+} and Gd^{3+} in UO_2, U^{5+} ions with smaller ionic radius than that of U^{4+} ions are formed from the electroneutrality condition, and then the Frenkel pairs of oxygen could be easily formed at lower temperature.

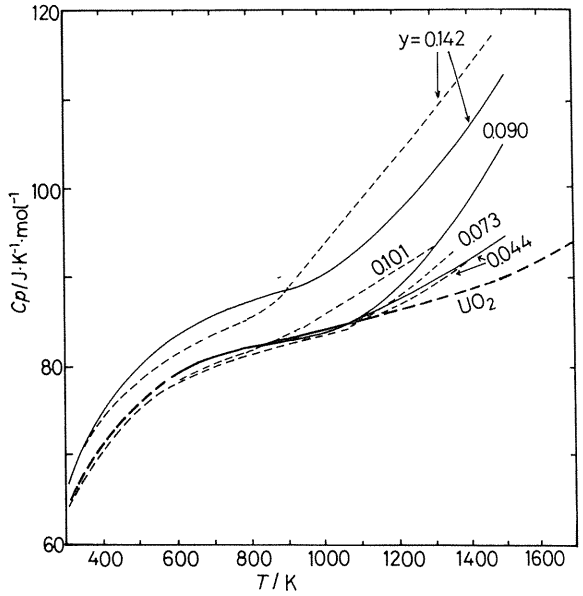

Fig. 10 Heat capacities of UO_2 doped with Gd (-----) and La (——) of the concentration from 4.4 to 14.2 mol %[27,28].

(b) $U_4O_{9\pm x}$

(1) Phase transition[13]

The crystal structure of U_4O_{9-x} is very similar to that of UO_{2+x}. The difference is that the arrangement of the interstitial oxygen atoms are ordered (or partially ordered) in U_4O_{9-x} phase with clearly discernible superlattice lines in the X-ray or neutron diffraction patterns, while those of UO_{2+x} phase are disordered[13].

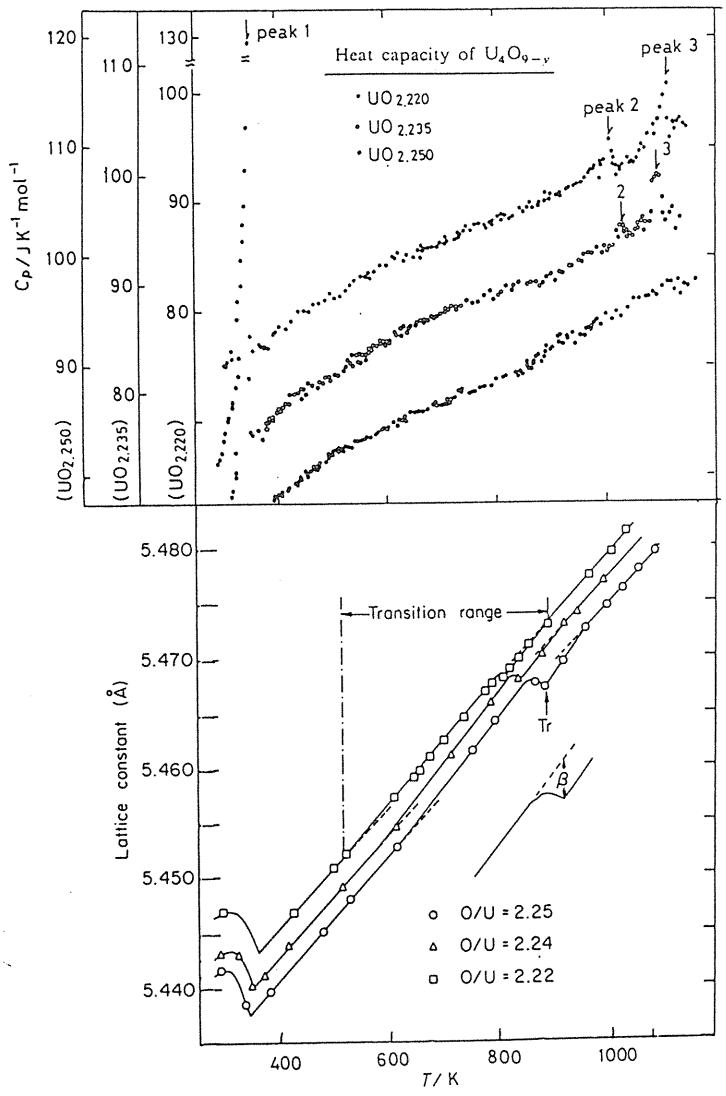

Fig. 11 (a) Variation of the lattice constant and heat capacity of U_4O_{9-y} with temperature at different O/U ratios[13].

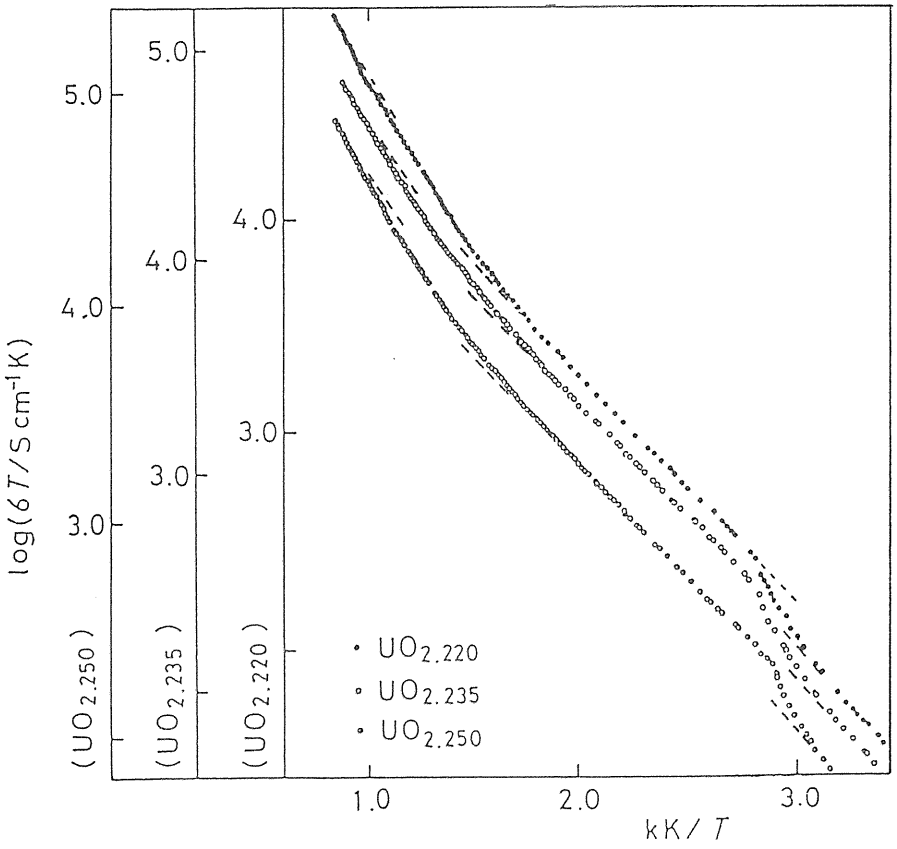

Fig. 11 (b) Variation of the electrical conductivity of U_4O_{9-y}[13].

The feature of the phase transition (α to β phase) around 300 K was studied in detail by the authors[13]. The changes in heat capacity[31,32], lattice constant[33,34] and electrical conductivity[32,34] at the transition were found to depend on the composition (O/U ratio) as seen in Fig. 11[13].

Apart from the transition around 300 K, the occurrence of another transition at high temperatures has been suggested[35,36]. The feature of this high-temperature transition has also been investigated by the authors[13] as seen from Fig. 11. From these facts observed, it was concluded that the phase transition of U_4O_9 is the order-disorder type involving change in the configuration of U^{4+} and U^{5+} ions in the U_4O_9 lattice, like Verwey transition in Fe_3O_4[37]: that the α-U_4O_9 phase consists of ordered cationic charges (U^{4+} and U^{5+}) with a less ordered anion superlattice structure based on interstitial oxygen, that the β-U_4O_9 phase consists of partly disordered cationic charges with a more ordered anion superlattice structure, and that the γ-U_4O_9 phase consists of disordered cationic charges with a more ordered anion superlattice structure.

Phase diagram of U_4O_{9-x} determined from heat capacity, lattice constant and electrical conductivity measurements is shown in Fig. 12[30].

(2) Defect structure

The predominant defect for U_4O_{9-x} has been considered to be oxygen vacancies on the basis of the data of the variation in density with the O/U ratio[38], but these oxygen vacancies

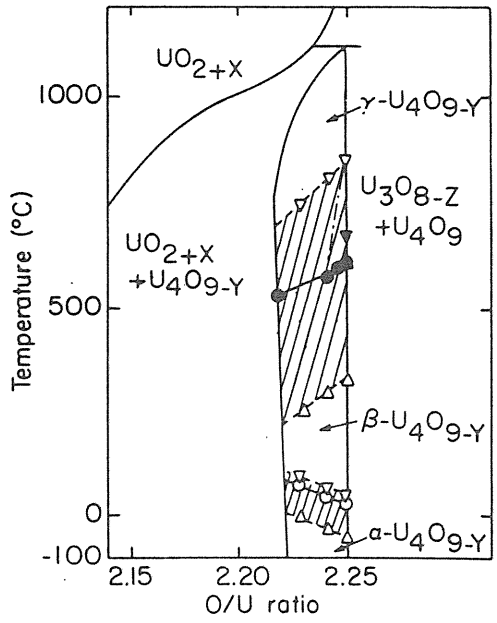

Fig. 12 Phase diagram of U_4O_{9-y}. ●: results of lattice constant by the present authors[30),34)], ○, △, ▽: results of electrical conductivity measurements by the present authors[30)], —·—·—: result by Blank and Ronchi[213)], ▼: result by Grønvold et al.[214)].

are paired with oxygen interstitials to form similar complex defects with UO_{2+x} consisting of two kinds of oxygen vacancies (V_o^a and V_o^b) and one oxygen interstitials (O_i)[39)], although these defects cause the long-range ordering forming the superlattice structure[33,40)].

The defect structure of U_4O_{9-x} was suggested by the authors from the electrical conductivity measurement based on Willis model as shown in Table 2[41)]. The existence of a hyper-U_4O_{9+x} phase at high temperatures has been claimed from the electrical conductivity measurement[41)], but the range of this hyperstoichiometric composition has not yet been determined.

Table 2 Defect models for $U_4O_{9\pm y}$[41)].

Phase	Temperature region	Defect models	Equations for defect formation	$1/n'$ for $P_{O_2}^{1/n'}$ Calc.	Exp.
U_4O_{9-y}	Low (783-883K)	$V_0^a:V_0^b:O_i = 2:1:2$	$\begin{cases} 2V_i + 2O_0^a + O_0^b = \{2V_0^a 2O_i V_0^b\}^{4\cdot} + 4e' + 1/2O_2(g) \\ \quad = \{2V_0^a 2O_i V_0^b\}^{6\cdot} + 6e' + 1/2O_2(g) \end{cases}$	$\begin{cases} -1/10 \\ -1/14 \end{cases}$	$-1/10 \sim -1/20$
	Intermediate (973-1063K)	$V_0^a:V_0^b:O_i = 2:2:2$	$\begin{cases} 2V_i + 2O_0^a + 2O_0^b = \{2(V_0^a O_i V_0^b)\}^{4\cdot} + 4e' + O_2(g) \\ \quad = \{2(V_0^a O_i V_0^b)\}^{8\cdot} + 8e' + O_2(g) \end{cases}$	$\begin{cases} -1/5 \\ -1/9 \end{cases}$	$-1/5 \sim -1/10$
	High (1298-1388K)	Decomposed model $Z \equiv [O_i'']/[V_0^a] = 1/2$	$\begin{cases} \{2(V_0^a O_i V_0^b)\}'''' = 4V_0'' + 2O_i'' \\ 1/n = \{(Z/3) - (1/3)\}/\{2(Z+1)\} \end{cases}$	$-1/18$	$-1/20 \sim -1/15$
U_4O_{9+y}	High (1298-1399K)	Decomposed model $Z = 2$	$\begin{cases} \{2(O_i' V_0 O_i')\}'''' = 4O_i'' + 2V_0'' \\ 1/n = \{(Z/3) - (1/3)\}/\{2(Z+1)\} \end{cases}$	$1/18$	$1/15 \sim 1/20$

(c) U_3O_{8-x}

(1) Phase transition[13)]

In the U_3O_8 region, the existence of many phases has been reported, and the relation prevailing among these phases has hitherto presented a rather confused picture. Recent careful measurements, however, reveal some of the complicated phase relations.

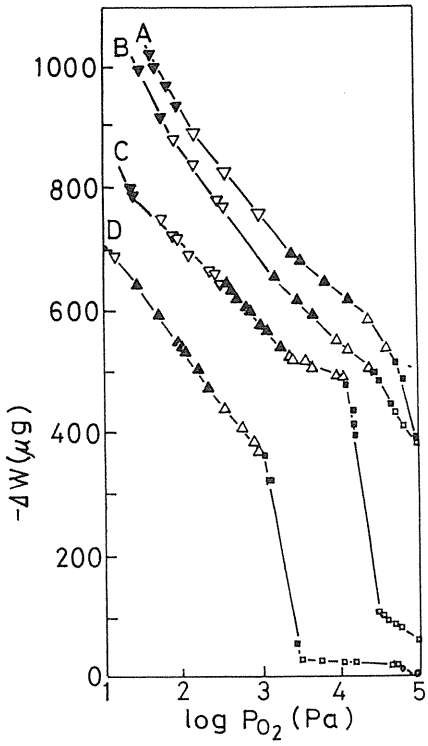

Fig. 13 (a) Relative weight change vs. oxygen partial pressure[13].
Temperature; A: 1268 K,
B: 1248 K, C: 1158 K, D: 1038 K,
□: ξ_1, ■: ξ_2, △: ξ_3, ▲: ξ_4, ▽: ξ_5,
▼: ξ_6

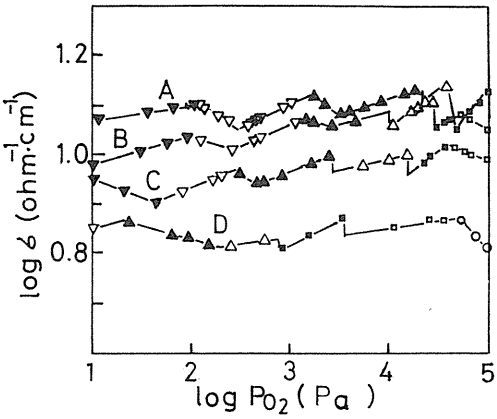

Fig. 13 (b) Isothermal conductivity vs. oxygen partial pressure[13].
Temperature; A: 1268 K,
B: 1248 K, C: 1158 K, D: 1038 K,
□: ξ_1, ■: ξ_2, △: ξ_3, ▲: ξ_4, ▽: ξ_5,
▼: ξ_6

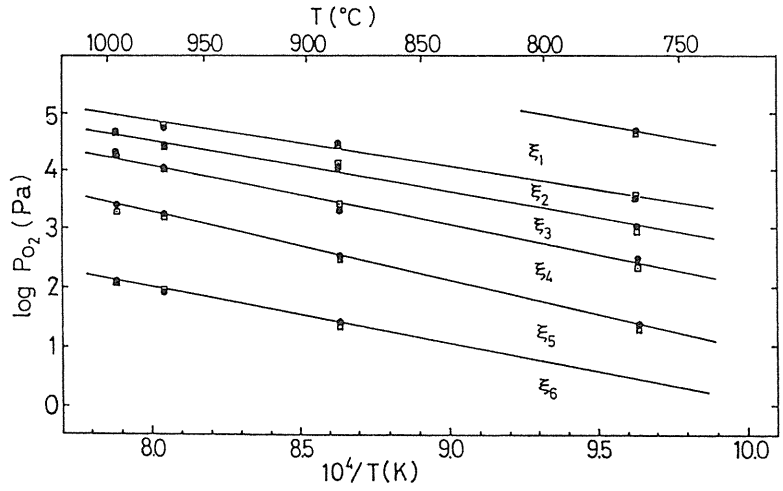

Fig. 13 (c) Oxygen potential diagram of U_3O_{8-x} phase[13].
○; phase boundaries determined by thermogravimetric method
□; phase boundaries determined by electrical conductivity measurement

In the α-U_3O_{8-x} region (hexagonal) above about 1000 K, the existence of at least six phases, ξ_1 to ξ_6, was reported by the authors from the small changes in both weight[42] and electrical conductivity[43] against oxygen partial pressure. Though the changes were small, the coincidence of both changes was good satisfactorily (Fig. 13)[13].

α'-U_3O_8 phase (orthorhombic) is stable at lower temperatures, and the occurrence of phase transition in α'-U_3O_8 phase has been reported at different temperatures. The heat capacity measurement of α'-U_3O_8 phase[44,45] revealed the existence of three λ-type phase transitions (as shown in Fig. 28 in our previous review[1]). The phase transitions in α'-U_3O_8 phase is shown to be similar to that in U_4O_9 phase, from the O/U dependences of the transition temperature and the entropy change, from the unit cell volume change, from the X-ray analysis and from the electrical conductivity measurement. Hence, we concluded that the phase transitions in α'-U_3O_8 phase are thought to be mainly due to the order-disorder rearrangement of U^{5+} and U^{6+} ions.

A phase diagram in α-U_3O_{8-x} based on the electrical conductivity, X-ray diffraction and heat capacity measurements is given in Fig. 14[44].

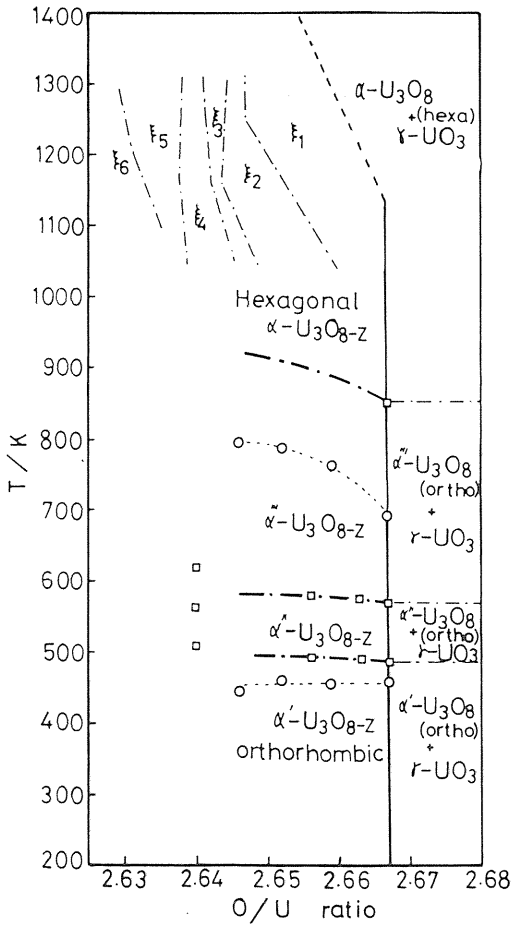

Fig. 14 Phase diagram in α-U_3O_{8-x} based on the electrical conductivity (○), X-ray diffraction and heat capacity (□) measurements[44].

(2) Defect structure

In α-U_3O_{8-x} phase, from the oxygen partial pressure dependences of electrical conductivity and compositional departure from stoichiometry, together with X-ray diffractometry patterns[42] for these ξ_1 to ξ_6 phases, we concluded[42] that the fundamental structure of the various phases ξ_1 to ξ_6 is a high-temperature α-U_3O_8 (hexagonal) structure, characterized by a sort of two-dimensional out-of-step structure[45] related to oxygen vacancies and interstitials, and that the individual phases are produced in the course of the ordering or disordering process between α-UO_3 like structure and β-UO_3 like structure. The change of oxygen partial entropy[42] calculated from the oxygen partial pressure change, against reciprocal temperature indicates the ordering or disordering process among these phases.

2. 2. 2. *U-Pu-O and U-Th-O systems*

Uranium-plutonium mixed oxide, $(U,Pu)O_{2+x}$, is of interest to the reactor engineers for use as fuel for fast breeder reactors and plutonium enriched thermal reactors. Thorium-uranium mixed oxide, $(Th,U)O_2$, has been recognized as a fuel of thermal breeder reactors.

(a) $(U,Pu)O_{2\pm x}$ and PuO_{2-x}

Defect structures in hypostoichiometric $(U_{1-y}Pu_y)O_{2-x}$ are proposed by several investigators, but the experimental results cannot be explained sufficiently by proposed model. The existence of hyperstoichiometric $(U_{1-y}Pu_y)O_{2+x}$ is not reported yet.

The oxygen partial pressure dependences (Po_2) of the electrical conductivity (σ) of $(U_{1-y}Pu_y)O_{2+x}$ (y=0, 0.05, 0.10, 0.20 and 0.50)[46] and PuO_{2-x}[47] observed by the authors at 1273 K are shown in Fig. 15.

In low oxygen partial pressure region below about 10^{-5} *Pa* at 1273 K, the slopes of $(U_{1-y}Pu_y)O_{2+x}$ except y=0 in Fig. 15 are zero, irrespective of y. It is considered that a neutral defect is predominant in this region. The oxygen partial pressure dependence of the compositional deviation(x) is needed to discuss in more detail the defect structure in this region. It is also seen from Fig. 15 that the value of electrical conductivity in this region increases with increasing y. This increase may be explained by the increase in the hopping probability between plutonium and uranium ions in addition to that between uranium ions.

From the slope in the intermediate oxygen partial pressure region at 1273 K shown in Fig. 15, the values of n' for y=0, 0.05, 0.10 and 0.20 are calculated as 2.1, 2.2, 3.0 and 4.1, respectively. In the case of y=0.50, the value of n' in the intermediate oxygen partial pressure region is difficult to be determined due to the influence of the formation of M_4O_{9-x} (M=U+Pu) phase. The defect models and electroneutrality conditions for $(U_{1-y}Pu_y)O_{2+x}$ proposed are summarized in Table 3. These values of n'=2.1, 2.2, 3.0 and 4.1 from log σ-log Po_2 relation can be interpreted from eq. (1) by taking the values for m=1,1,2 and 3, respectively.

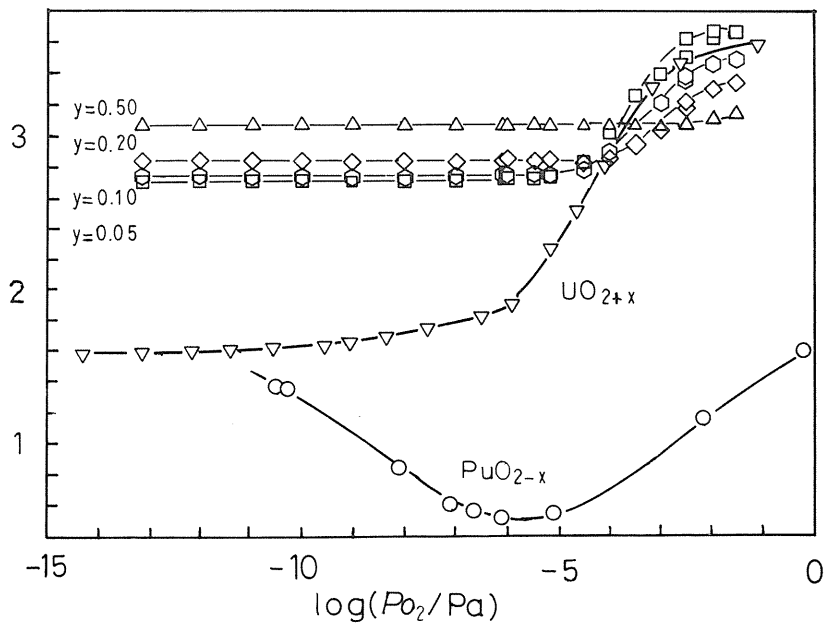

Fig. 15 The oxygen partial pressure dependences (Po_2) of the electrical conductivity (σ) of $(U_{1-y}Pu_y)O_{2+x}$ (y = 0, 0.05, 0.10, 0.20 and 0.50) and PuO_{2-x} at 1273 K[46,47].

Table 3 Defect models and electroneutrality conditions for $(U_{1-y}Pu_y)O_{2+x}$[47,51].

y	n' for $\sigma \propto (Po_2)^{1/n'}$	Defect model	Electroneutality condition
0	2.1	$\{2(O_i^{a\,b}O_i^{a\,b}V_O)\}'$	$[h^{\cdot}]=[\{2(O_i^{a\,b}O_i^{a\,b}V_O)\}']$
0.05	2.2	$\{2(O_i^{a\,b}O_i^{a\,b}V_O)\}'$	$[h^{\cdot}]=[\{2(O_i^{a\,b}O_i^{a\,b}V_O)\}']$
0.10	3.0	$\{2(O_i^{a\,b}O_i^{a\,b}V_O)\}''$	$[h^{\cdot}]=2[\{2(O_i^{a\,b}O_i^{a\,b}V_O)\}'']$
0.20	4.1	$\{2(O_i^{a\,b}O_i^{a\,b}V_O)\}'''$	$[h^{\cdot}]=3[\{2(O_i^{a\,b}O_i^{a\,b}V_O)\}''']$

On the other hand, the slopes of the plot of log σ against log Po_2 for the n-type region of PuO_{2-x} is obtained to be $-1/4.72$ at 1273 K. The pressure dependence of $-1/5$ has been interpreted in two ways, by assuming (1) a defect structure involving quadruply charged interstitial plutonium ions proposed by Atlas and Schlehman[48] and (2) a defect structure with completely ionized oxygen vacancy pairs proposed by Chereau and Wadier[49]. It is difficult to decide which model is suitable for this case from the pressure dependence of electrical conductivity alone. However, judging from the density measurement by Atlas et al[50] whose experimental density decreased with increasing deviation from stoichiometry, the ionized oxygen vacancy model seems to be more reasonable in this system.

It is noted in Fig. 15 that there is a minimum in the curve of electrical conductivity of PuO_{2-x}. The minimum could occur by the presence of some impurities in PuO_{2-x}, but the possibility of the existence of hyper-stoichiometric PuO_2 also could not be excluded by considering the concentration of the impurities in this sample used. An intrinsic band-gap energy of 2.5 eV was calculated from the temperature dependence of the minimum electrical conductivity.

(b) $(U,Th)O_{2+x}$

Some studies on the oxygen potentials of $(Th_{1-y}U_y)O_{2+x}$ (y=0.05–0.3) have been carried out by electrochemical method and thermogravimetry (y=0.05–0.2), but the agreement among them is insufficient.

The relations between log Po_2 and log x for $(Th_{1-y}U_y)O_{2+x}$ (y=0.2, 0.4 and 1.0) at 1282 K by the present authors[51] together with that by Aronson and Clayton[52] are shown in Fig. 16. In these figures, the dependences of x upon Po_2 for $(Th_{1-y}U_y)O_{2+x}$ (y=0.2 and 0.4) can be obtained for four divided regions, whereas that for $UO_{2\pm x}$ for three divided regions.

Table 4 Defect models of $(Th,\ U)O_{2+x}$[51].

phase	composition x	n for $x \propto P_{O_2}^{1/n}$	Defect model	Electroneutrality consition
$(Th,U)O_{2+x}$	x<0.001	2	Neutral defect $(\{2O_i^{a\,b}O_i^{a\,b}2V_O\})$	[e]=[h]
	0.001<x<0.003	4	$\{2O_i^{a\,b}O_i^{a\,b}2V_O\}'$	$[h]=[\{2O_i^{a\,b}O_i^{a\,b}2V_O\}']$
	0.003<x<0.008	12	$\{2O_i^{a\,b}O_i^{a\,b}2V_O\}^{5'}$	$[h]=5[\{2O_i^{a\,b}O_i^{a\,b}2V_O\}^{5'}]$
	x>0.008	4	$\{2(O_i^{a\,b}O_i^{a\,b}2V_O)\}'''$	$[h]=3[\{2(O_i^{a\,b}O_i^{a\,b}V_O)\}''']$

Defect models and electroneutrality conditions for $(Th_{1-y}U_y)O_{2+x}$ proposed are summarized in Table 4. It may be concluded that the defect structure of $(Th_{1-y}U_y)O_{2+x}$ can be interpreted with the complex defect model consisting of two different types of interstitial oxygens and oxygen vacancies, similarly to that of UO_{2+x}[12].

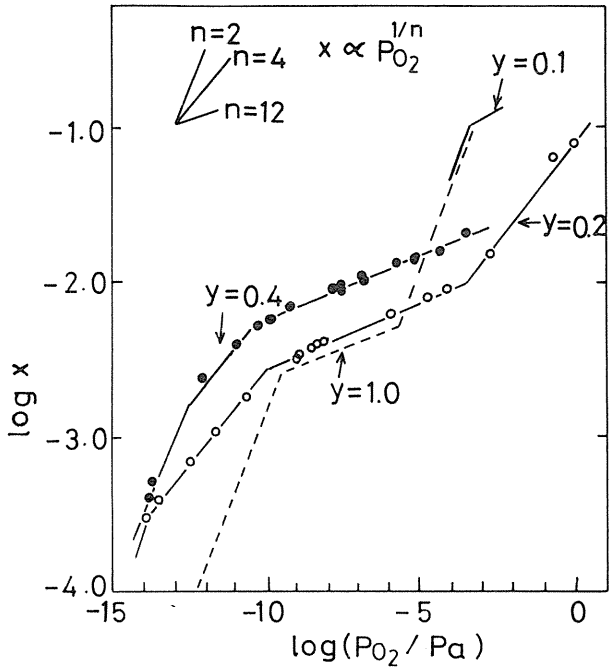

Fig. 16 The relations between log Po_2 and log x for $(Th_{1-y}U_y)O_{2+x}$ ($y = 0.2$, 0.4 and 1.0) at 1282 K by the present authors[51] together with that ($y = 0.1$) by Aronson and Clayton[52].

2. 2. 3. *Rare Earth Oxides*

The rare earth elements are produced by nuclear fission in the fuels, and the study on rare earth oxides is of importance to interprete the behavior of these elements in the oxide fuels and also interesting from the point of view of solid chemistry because of the similarity to actinide oxides.

(a) Nd_2O_{3+x}

The electrical conductivity of Nd_2O_3 has been measured by many investigators[53-58], but most of them have been limited to the temperature dependence of the electrical conductivity in air.

The electrical conductivity of Nd_2O_{3+x} was measured by the authors as a function of oxygen partial pressure in the temperature range from 1173 to 1373 K[55], and the results are shown in Fig. 17. As seen in Fig. 17, p-type conduction exists in the high pressure region near the stoichiometry of Nd_2O_3 and the predominant ionic conduction, which is nearly independent of oxygen partial pressure, was seen in low pressure region. Total conductivity, σ_t, can be expressed as the sum of electrical conductivity, σ_p, and ionic one, σ_i. σ_p is obtained

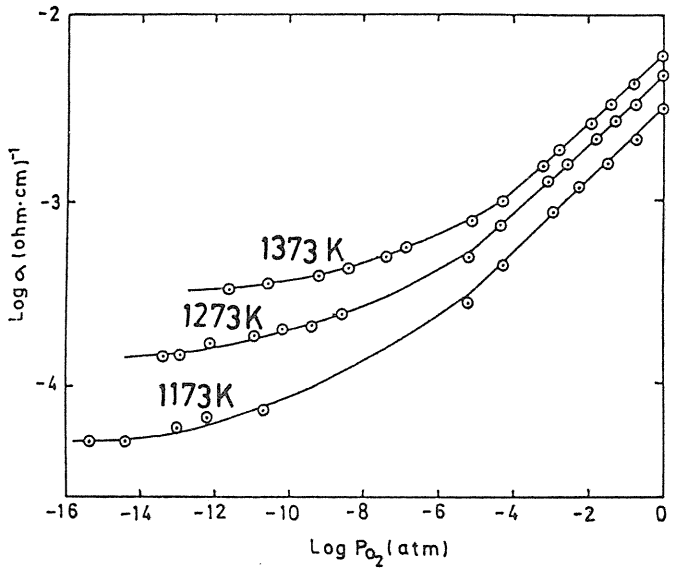

Fig. 17 Electrical conductivity of Nd_2O_3 as a function of oxygen partial pressure from 1173 to 1373 K[55].

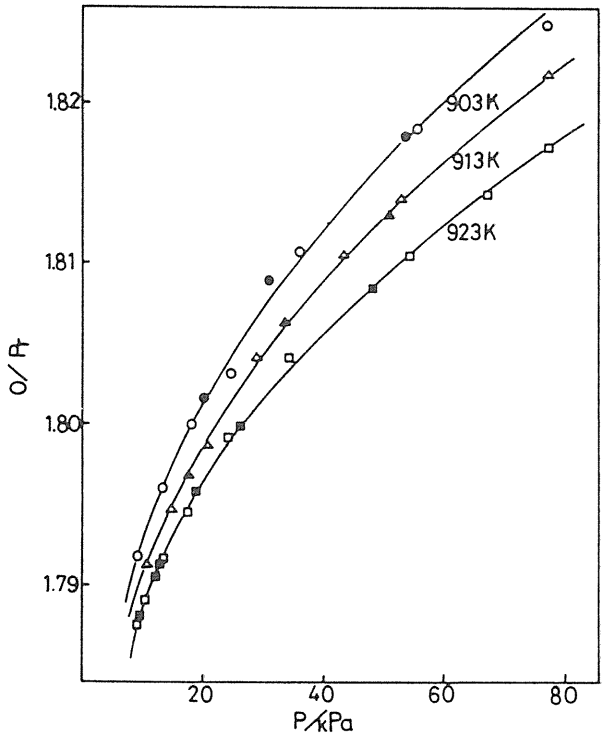

Fig. 18 Composition-pressure plot in the α-phase at 903, 913, 923 K; ○, △, □ oxidation; ●, ▲, ■ reduction[57]. Solid line represents eq. (8).

by subtracting σ_i from σ_t.

The slopes (n') of the plot of log σ_p vs. log Po_2 vary from 1/5.1 at 1373 K to 1/4.6 at 1173 K. As these values of the slope at high temperature are near to 1/5.3, it can be considered that the predominant defects at high temperature are triply ionized metal vacancy assuming the following reaction:

$$4/3O_2 = 3/2O_0 + V_M''' + 3h \tag{6}$$

$$[h] \propto Po_2^{3/16} , \tag{7}$$

where the electroneutrality condition is $[h]=3[V_M''']$.

The rare earth sesquioxides such as Eu_2O_3[53], Ho_2O_3[54] and Y_2O_3[55] with the metal vacancy as the predominant defect structure have been reported previously.

(b) *Pr-O* system

Simultaneous measurements of oxygen pressure, composition and electrical conductivity were made by the authors for the alpha (PrO_{2-x})[57], epsilon ($Pr_{10}O_{18\pm x}$)[57], zeta (Pr_9O_{16-x})[58] and iota (Pr_7O_{12-x})[58] praseodymium oxides. The composition-pressure diagram for the α-phase (PrO_{2-x}) is shown in Fig. 18[57] and the plots of PrO_{2-x} are seen to fit very well to the following parabolic equation:

$$2-x = 1.780 + k(P-Po)^{1/2} , \tag{8}$$

where k is a constant independent of pressure and Po a hypothetical equilibrium pressure at a hypothetical stoichiometric composition $O/Pr=1.780$. The good fitting to eq. (8) indicates that the predominant defects of the alpha phase are neutral oxygen interstitials, since the concentration of neutral oxygen vacancy is shown to be proportional to $Po_2^{1/2}$. The small slopes in log σ-log P plots in the alpha phase also supported this conclusion.

For the nonstoichiometric epsilon phase[57], the nonstoichiometric parameter δ of $PrO_{1.800\pm\delta}$ can be expressed by the defect model of neutral interstitials and neutral vacancies as eq. (9) and by that of neutral interstitials and doubly charged vacancies as eq. (10), since $[O_i]$ is proportional to $Po_2^{1/2}$, $[V_o] \propto Po_2^{-1/2}$ and $[Vo''] \propto Po_2^{-1/6}$,

$$\delta = [O_i]-[V_o] = k_1Po_2^{1/2} - k_2Po_2^{-1/2} \tag{9}$$

$$\delta = [O_i]-[V_o''] = k_1Po_2^{1/2} - k_2Po_2^{-1/6} , \tag{10}$$

where $[O_i]$, $[V_o]$ and $[V_o'']$ are the concentrations of neutral oxygen interstitials, neutral oxygen vacancies and doubly charged oxygen vacancies, respectively, and K_1 and K_2 are constants independent of oxygen pressure. The fittings of eqs. (9) and (10) to the experimental composition-pressure curve were fairly good.

In the zeta ($Pr_9O_{16\pm x}$)[57] and iota ($Pr_7O_{12\pm x}$)[57] phases, we introduced the nonstoichiometric parameters for $PrO_{1.778+\delta}$ and $PrO_{1.714+\delta}$, similarly to the case of epsilon phase, and the curve fitting of eqs.(9) and (10) to the experimental data was good in the high pressure region, but a slight deviation of the fitting was observed in low pressure region. The electrical conductivities of both phases are found to increase very slightly with oxygen pressure. Composition-pressure and electrical conductivity-pressure diagrams suggested that the predominant point defects in these nonstoichiometric zeta and iota phases are neutral oxygen interstitials and doubly charged oxygen vacancies[58].

2. 2. 4. Refractory metal oxides

As the first wall and structural materials of nuclear fusion reactor, refractory metals (group 4A, 5A and 6A in the periodic table) seem to be promissing. But these metals are known to react easily with oxygen, so that it is of importance to have the precise knowledge about the phase equilibria and defect structure of these oxides.

(a) *Nb-O* system

Although the phase equilibria in the niobium-oxygen system have been studied by many investigators, the existence of many oxide phases has not been well established between NbO_2 and Nb_2O_5[59,60]. The phase relations of several oxides between NbO_2 and Nb_2O_5 below 1700 K proposed by the authors[59,61,62] based on the data of the electrical conductivity measurements and electromotive force measurements are shown in Fig. 19. The phase relations at high temperature above 1700 K in the range from *Nb* metal to Nb_2O_5 have also been determined based on the vapor pressure measurements by the authors[63-67], since the mass-spectrometric method may be the only method applicable for the phase study at high temperature.

The oxygen partial pressure dependences of the composition and the electrical conductivity observed by the authors[60-62] are shown in Fig. 20 together with those reported previously for homologous phases between NbO_2 and Nb_2O_5[68-71]. The discontinuities in the curves of electrical conductivity and composition indicate the presence of the narrow homologous phases. The various slope values for the plots of log x against log Po_2 (n value) and log σ against log Po_2 (n' value) for the homologous phases were interpreted in terms of various defect structures by the authors[61,62]: In the nonstoichiometric region of Nb_2O_{5-x} phase, the values of $n=-5.2$[62] and $n'=-4.2 \sim -4.8$[61] were obtained by the authors at 1173-1283 K and 1283-1573 K, respectively. These n' values can be interpreted by a defect model involving

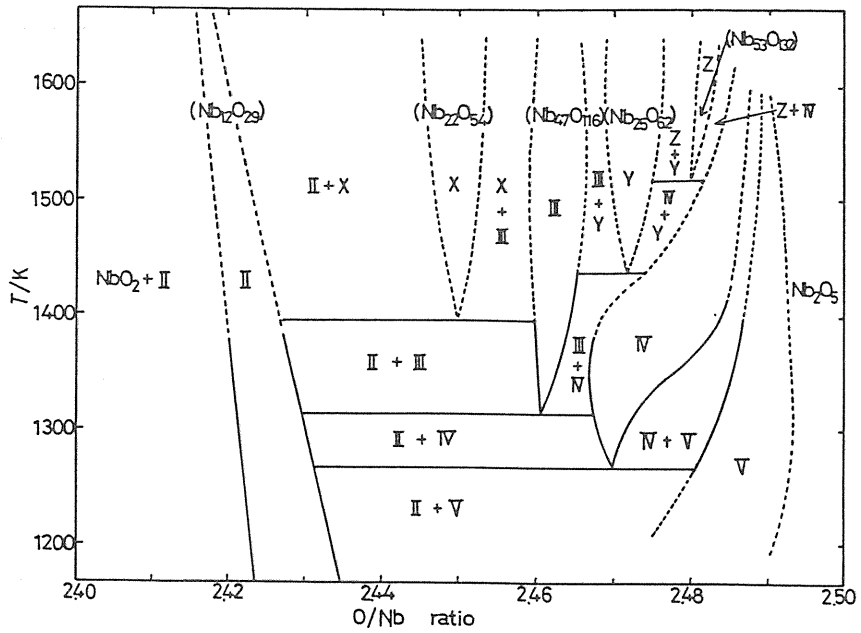

Fig. 19 Phase diagram of the region between NbO_2 and Nb_2O_5[59,61,62].

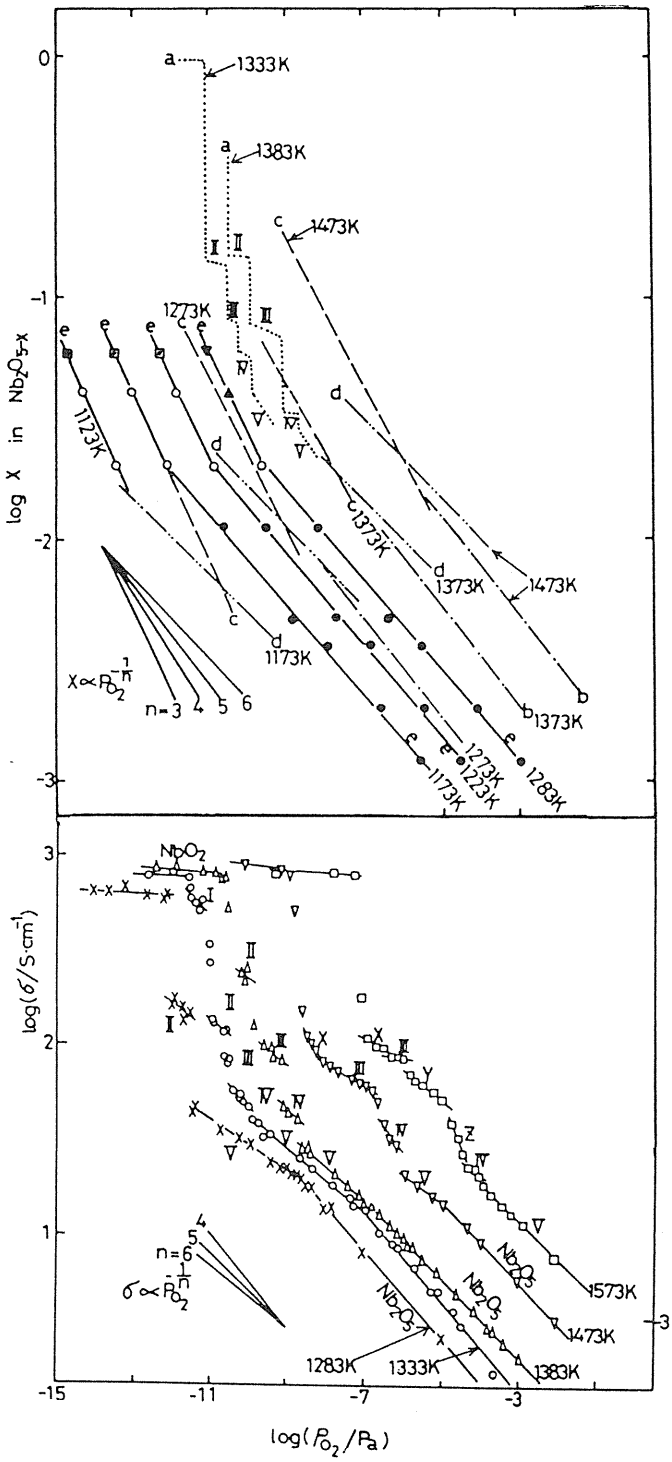

Fig. 20 The relation between log x in Nb_2O_{5-x} and oxygen partial pressure for the phases between NbO_2 and Nb_2O_5[60,62] and log σ vs. log Po_2[61].

(a ·····) Naito et al[61],
(b —·—) Wimmer and Tripp[68],
(c ---) Blumenthal et al[69],
(d —··—) Kofstad and Anderson[70,71],
(e —●—) Nb_2O_{5-x}[62],
(e —○—) phase V[62],
(e —▼—) phase IV[62],
(e —▲—) $V+IV$[62],
(e —■—) $V+II$[62]

both singly ionized oxygen vacancies ($V\dot{o}$) and doubly ionized oxygen vacancies ($V\ddot{o}$) with the different concentration ratio of $V\dot{o}/V\ddot{o}$ with different temperatures[61,62]. In the region of V phase next to Nb_2O_{5-x} phase, the value of n=3 was obtained in the temperature range from 1123 to 1223 K[62]. On the other hand, n' values for V phase were observed to vary with temperature: −7.8 at 1283 K, −5.8 at 1333 K, −5.7 at 1383 K, −5.1 at 1473 K and −4.7 at 1573 K[61]. These n and n' values can be interpreted by the defect model involving neutral oxygen vacancies (Vo), neutral and singly ionized $Nb_{25}O_{62}$-type Wadsley defect (V_{wad} and $V_{wad}^{\cdot}$), quasi-free electrons and tetravalent niobium ions[62]. With this model, n values may change from −2 to −8 depending on the concentration ratios of $[Vo]$, $[V_{wad}]$ and $[V_{wad}^{\cdot}]$. The value n=−3 is given by assuming $[Vo] \simeq [V_{wad}] \geqq [V_{wad}^{\cdot}]$. The value of n'=−8 obtained with this model is consistent with the experimental value n'=−7.8 at 1283 K[62]. Other values (n'=−5.8 ~ −4.7) at high temperatures above 1283 K can be interpreted by the similar complex defect consisting of $Nb_{25}O_{62}$-type Wadsley defect and singly ionized oxygen vacancies[61]. Phase IV shows the different values of n' at various temperatures: n'=−5.4 at 1333 K, −5.2 at 1383 K, −2.0 at 1473 K, and −3.8 at 1573 K[61]. The values of n at lower temperatures (1333 and 1383 K) may be interpreted by a similar complex defect model consisting of point defects and $Nb_{22}O_{54}$-type Wadsley defects[61]. However, for the values of n at high temperatures (1473 and 1573 K), an explanation based on other defect structure seems to be necessary[61]. Phase III shows n'=−5.4 at 1383 K, −8.0 at 1473 K, and −16 at 1573 K[61]. These values may be explainable by a complex defect model consisting of singly charged oxygen vacancy and $Nb_{22}O_{54}$-type Wadsley defect[61]. Phase X is considered to correspond to $Nb_{22}O_{54}$, and the values of n' obtained as −2.9 at 1473 K and −8.3 at 1573 K are not simple to interpret[61]. In phase II, n' values obtained as −4.9 at 1333 K and −5.5 at 1383 K may also be interpreted by a mixing model of singly charged oxygen vacancy $[V\dot{o}]$ and doubly charged oxygen vacancy $[V\ddot{o}]$: 38 % of $[V\ddot{o}]$ at 1333 K and 69 % of $[V\ddot{o}]$ at 1383 K[61].

The vapor pressures over the system between niobium-oxygen solid solution and $NbO_{2\pm x}$ were measured by means of mass spectrometry at high temperature and the presence of $NbO(g)$ and $NbO_2(g)$ was observed by the present authors[63-67]. The oxygen partial pressures for this system above 1900 K could be calculated from the ratio between the partial pressures of $NbO_2(g)$ and $NbO(g)$[63-67]. From the temperature dependence of the oxygen partial pressure, thus calculated, the partial molar enthalpy and entropy of oxygen were determined for Nb-O solid solution[65,67] and $NbO_{2\pm x}$[60,64]. The compositional dependence of the partial molar entropy of oxygen can be explained by assuming the occupancy of octahedral sites by the interstitial oxygen in the Nb-O solid solutions. The partial molar enthalpy and entropy of oxygen in nonstoichiometric $NbO_{2\pm x}$ showed a complicated (irregular) dependence, indicating the presence of a series of different kinds of short-range ordering[60,64].

The heat capacities and the electrical conductivities of NbO_2[72] and NbO_2 doped with Zr and Mo[73] were measured by means of direct-heating pulse calorimetry from 400 to 1170 K. As shown in Fig. 21[74], a λ-type peak in the heat capacity and a rapid increase of the electrical conductivity due to semiconductor-metal phase transition were obtained for NbO_2. Similar anomalies in the heat capacity and the electrical conductivity curve were seen in doped NbO_2. The entropy change due to the phase transition was calculated in terms of the 4 //-band electronic and the harmonic vibrational contributions, and a large contribution by the former to the total entropy was suggested. The phase transition was explained by the change of cation-cation bonding in the direction of the c-axis, producing the metallic 4d//-band structure in the high temperature phase.

(b) V-O system

The phase diagram of the V-O system was shown in Fig. 22[74], which was obtained on the basis of the partial phase diagram between V and VO by Alexander and Carlson[81], that

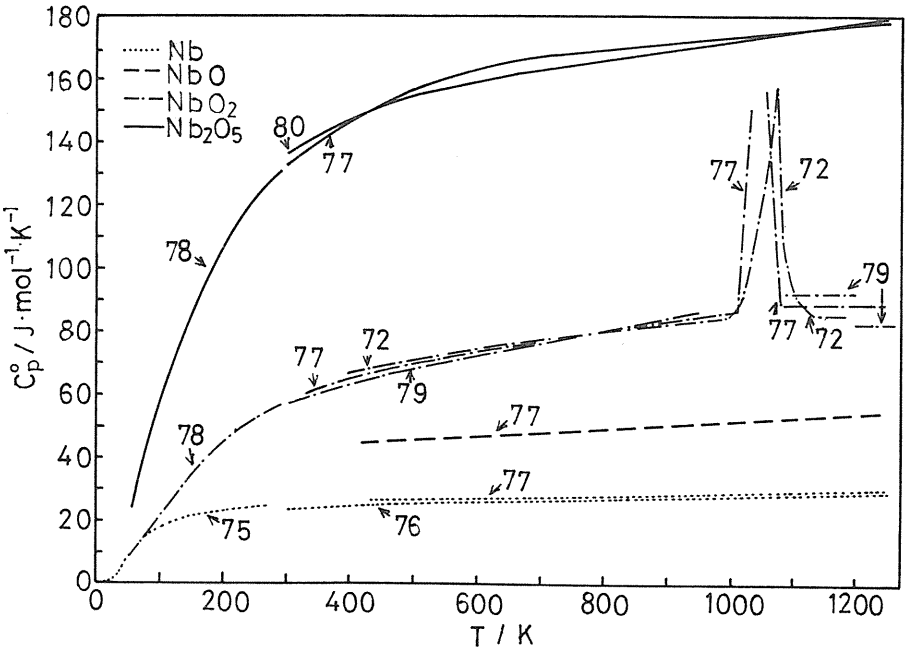

Fig. 21 Heat capacities of *Nb, NbO, NbO_2* and *Nb_2O_5*. Number in the figure corresponds to the reference number[74].

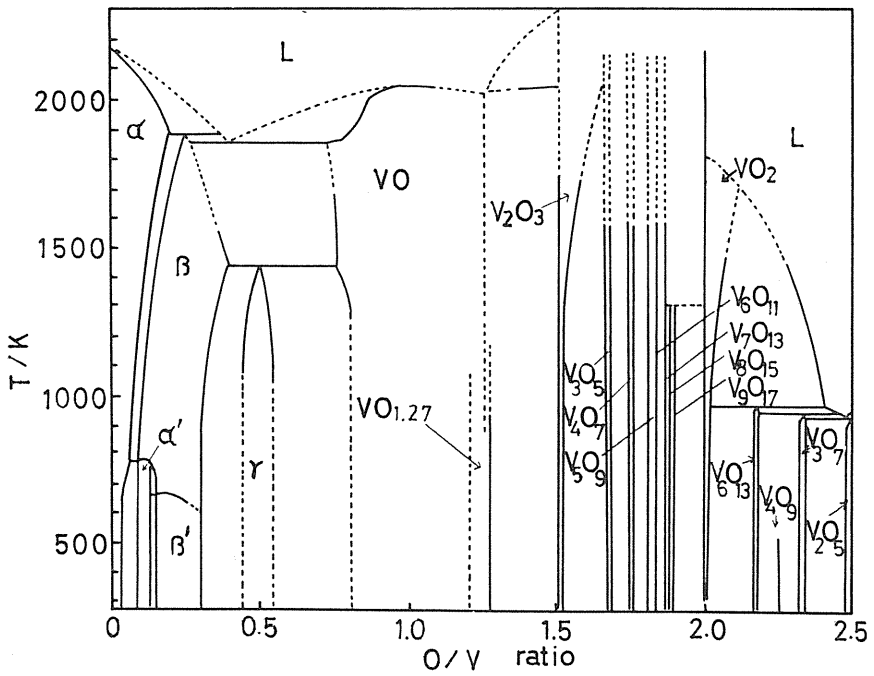

Fig. 22 Phase diagram of the vanadium-oxygen system[74].

between V_2O_3 and V_2O_5 by Kosuge[76,82], and the phase boundaries of VO_x (α, α', β, β') solid solutions by Hiraga and Hirabayashi[83] and the authors[84]. It is characteristic that both the *V-O* and the *Nb-O* system have complex Magneli-phases in the high *O/M* (*M*=*V* and *Nb*) ratios below about 1500 K.

The oxygen partial pressures of the phases between *V-O* solid solution and VO_2 were determined by the authors by means of mass-spectrometry[86-88]. The total vapor pressure and partial vapor pressures of $V(g)$, $VO(g)$, $VO_2(g)$, $O(g)$ and $O_2(g)$ obtained by mass-spectrometry as a function of composition at averaged temperature 1900 K are shown in Fig. 23[86-88] including the data by Frantseva and Semenov[89], where the partial pressures of $O(g)$ and $O_2(g)$ were calculated based on the gas equilibrium between $VO(g)$ and $VO_2(g)$. From the temperature dependence of the oxygen partial pressure thus obtained, the partial molar enthalpy and entropy of oxygen were obtained[86-88].

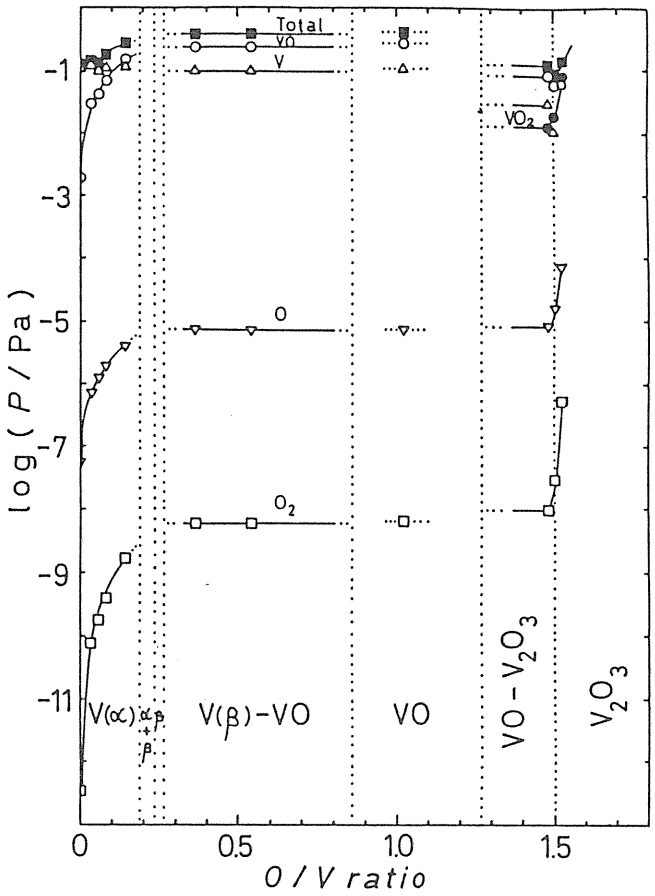

Fig. 23 Total and partial vapor pressures of $V(g)$, $VO(g)$, $VO_2(g)$, $O(g)$ and $O_2(g)$ as a function of O/V ratios at 1900 K based on our previous data[86-88].
■: total pressure, △: $V(g)$, ○: $VO(g)$, ●: $VO_2(g)$, ▽: $O(g)$ and □: $O_2(g)$.
The data at $O/V = 1.52$ and 1.4975 are reported by Frantseva and Semenov[89].

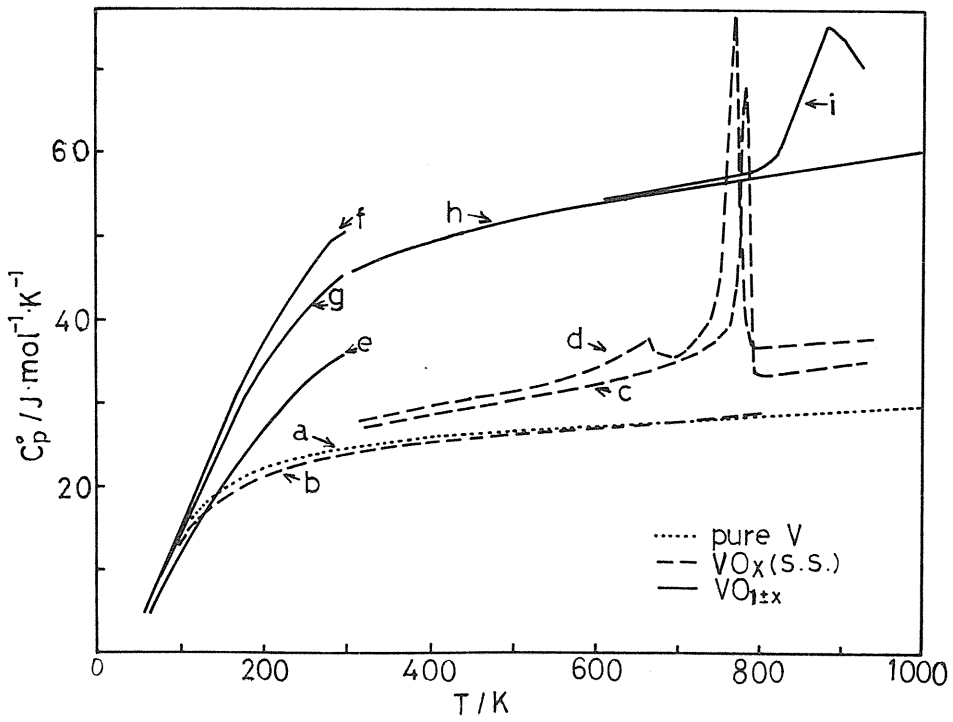

Fig. 24 Heat capacities of V, VO_x (solid solution) and $VO_{1\pm x}$[74].
a: V[90], b: $VO_{0.0346}$[90], c: $VO_{0.0834}$[84], d: $VO_{0.1296}$[84],
e: $VO_{0.86}$[85], f: $VO_{1.30}$[85], g: VO[92], h: VO[93], i: $VO_{1.063}$[85].

The heat capacities of VO_x alloys (x=0.0834, 0.1127, 0.1245 and 0.1296) in the region of α', β' and β phases[84], $VO_{1\pm x}$ (x=−0.117, 0.063 and 0.267) and $VO_{1.0}$ doped with Nb[85] were measured from 320 to 920 K by the authors by means of adiabatic scanning calorimetry. Some of our these results[84,85] are shown in Fig. 24 together with the previous results by other researchers[90-93]. In VO_x alloys, a heat capacity anomaly of $\alpha'-\alpha$ phase transition due to order-disorder rearrangement of oxygen atoms in the octahedral sites was observed around 770-790 K for each composition[84]. For $VO_{1\pm x}$ phase, the high temperature heat capacity peak was seen around 900 K in $VO_{1.063}$[85], which was thought to be due to the order-disorder rearrangement of clusters of oxygen and vanadium vacancies and/or clusters of interstitial vanadium and vanadium vacancy[85].

(c) TiO_x solid solution

Heat capacities of titanium-oxygen alloys, TiO_x (x=0.215, 0.306, 0.409 and 0.466), and doped alloys, $(Ti_{1-y}V_y)O_{0.2}$ (y=0.016 and 0.048) and $(Ti_{1-y}Al_y)O_{0.2}$ (y=0.03 and 0.05), were measured from 320 to 910 K by adiabatic scanning calorimeter[94]. As seen in Fig. 25, two kinds of heat capacity anomalies were observed for all samples except $VO_{0.466}$. The anomaly at higher temperatures was assigned to be due to an order disorder rearrangement of oxygen atoms, although the transition enthalpy and entropy obtained by the authors[94] are smaller than the theoretical values in the range of $O/Ti \geqq 0.4$. Another anomaly observed at lower temperatures depends on cooling condition, indicating that this anomaly is due to a non-equilibrium phenomenon, relating to the frozen long range order of oxygen atoms at some

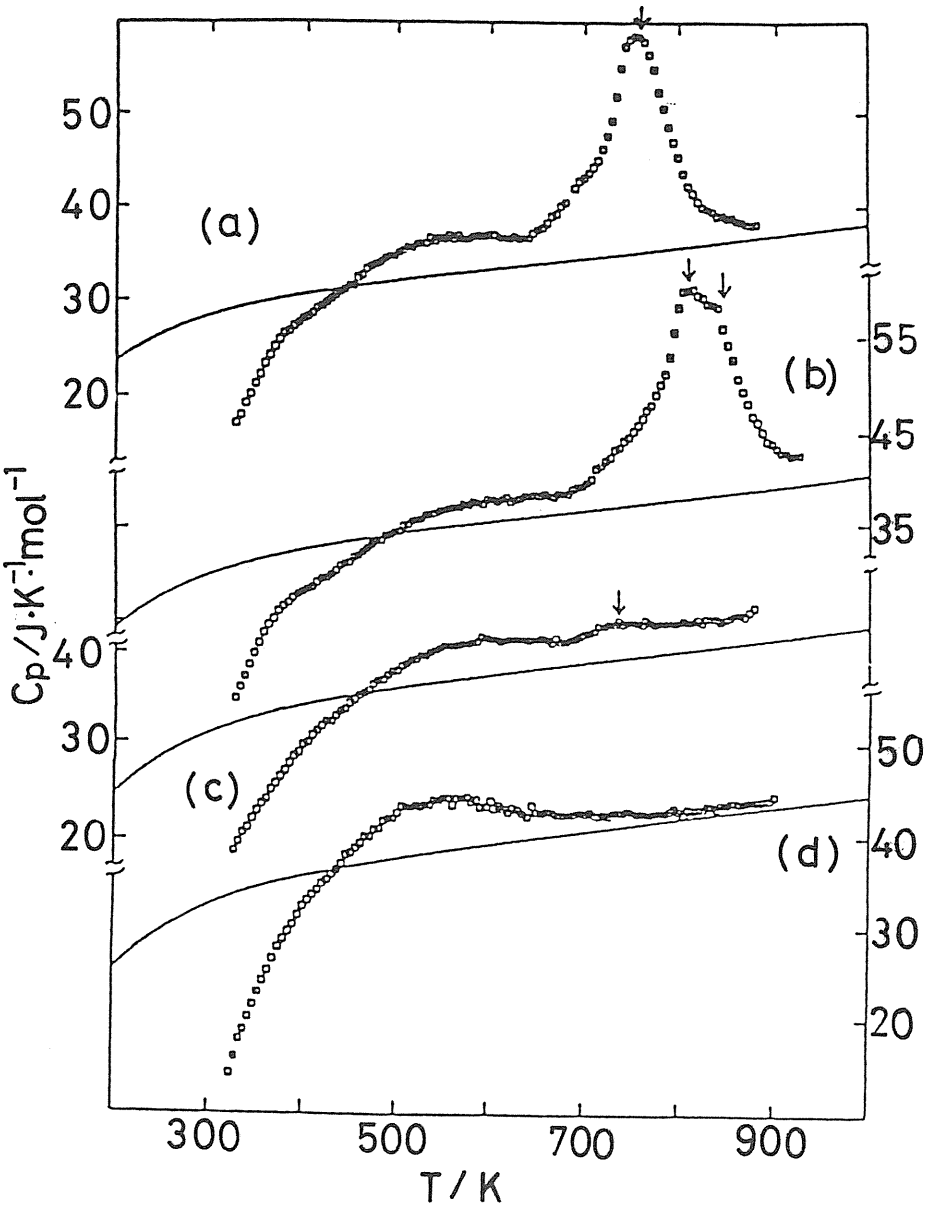

Fig. 25 Heat capacities of TiO_x solid solutions[94)]

a: $TiO_{0.215}$, b: $TiO_{0.306}$, c: $TiO_{0.409}$, d: $TiO_{0.466}$
The baseline (solid line) of heat capacity for each sample is calculated from Kopp-Neuman's rule.

temperature between room temperature and the order-disorder transition temperature and to the oxygen migration process to induce the increase in the degree of order of the "frozen in" state during heating the sample[94)]. The heat capacity anomalies were also observed in the case of doped TiO_x[94)]. The transition temperature and the enthalpy and entropy changes at the

transition decrease with increasing dopant contents of *V* and *Al*, suggesting that the arrangement of oxygen atoms at lower temperatures may be partially ordered by the interaction between doped metal and oxygen atoms.

(d) $Cr_2O_{3\pm x}$

The nonstoichiometric composition of $Cr_2O_{3\pm x}$ was measured by the authors[96] by thermogravimetry in the range of $1173 \leqq T/K \leqq 1373$ and $10^{-17} \leqq Po_2/Pa \leqq 10^5$ and the results are shown together with the result of electrical conductivity measurements[95] in Fig. 26. The compositional deviation from stoichiometry, *x*, in the hyperstoichiometric Cr_2O_{3+x} phase was observed to be smaller than 2×10^{-4}, irrespective of temperatures, provided that the hyperstoichiometric Cr_2O_{3+x} exists. The existence of the hypostoichiometric Cr_2O_{3-x} phase was first established by the present authors[95,96] in the region of low oxygen partial pressure below 10^{-5} Pa. From the oxygen partial pressure dependence of *x* in Cr_2O_{3-x}, the defect structure was discussed: In the composition near the stoichiometry of Cr_2O_{3-x}, the neutral chromium interstitials (Cr_i) formed by the reaction:

$$3O_o + 2Cr_{Cr} = 2Cr_i + 3/2O_2(g) \ , \tag{11}$$

where O_o is an oxygen ion on a normal lattice site and Cr_{Cr} a chromium ion on its normal lattice site. From eq. (11) the following relation can be obtained

$$x \propto [Cr_i] \propto P_{O_2}{}^{-3/4} \ , \tag{12}$$

where $[Cr_i]$ indicates the concentration of Cr_i. The value of $n=-4/3$ is close to the experimental values of $n=-1.3 \sim -1.8$ in the compositional region near the stoichiometry. The very small dependence of the electrical conductivity upon oxygen partial pressure can

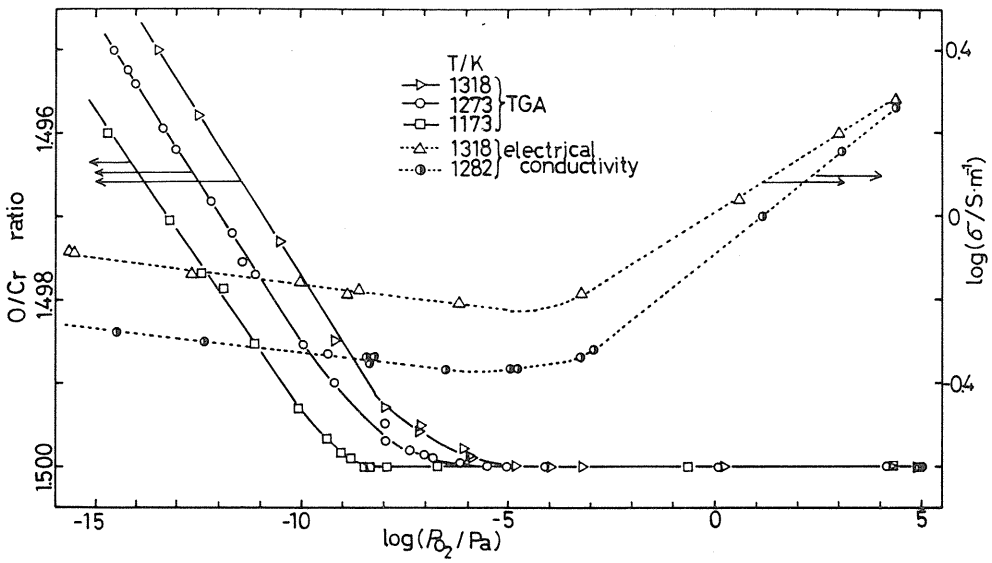

Fig. 26 Variation of *O/Cr* ratio and electrical conductivity of $Cr_2O_{3\pm x}$ with oxygen partial pressure[95,96].

also be explained from the existence of the neutral defect. In the compositional region with relatively large x ($x>0.0015$ in $CrO_{1.5-x}$), the triply charged chromium interstitials $Cr_i^{\cdots}$ can be proposed. The formation of $Cr_i^{\cdots}$ is given as

$$3O_O + 2Cr_i = 2Cr_i^{\cdots} + 3/2O_2(g) + 6e' \quad . \tag{13}$$

From eq. (13), the following relation can be derived

$$x \propto [Cr_i^{\cdots}] \propto P_{O_2}{}^{-3/16} \quad . \tag{14}$$

The n value ($n=-16/3=-5.3$) derived from eq. (14) is not so different from the experimental value $n\simeq -7$[31], but the value $n'=-5.3$ also given from this model is different from the very small dependence of the electrical conductivity upon oxygen partial pressure observed experimentally by the present authors[94]. The difference between the theoretical and the experimental n and n' values may be caused from the variation of the electron mobility with oxygen partial pressure and/or interaction between defects[96]. The existence of iron interstitials as the predominant defects in Fe_2O_{3-x} with small x values, which has the same corundum structure as Cr_2O_3 has been reported by Chang and Wagner[97].

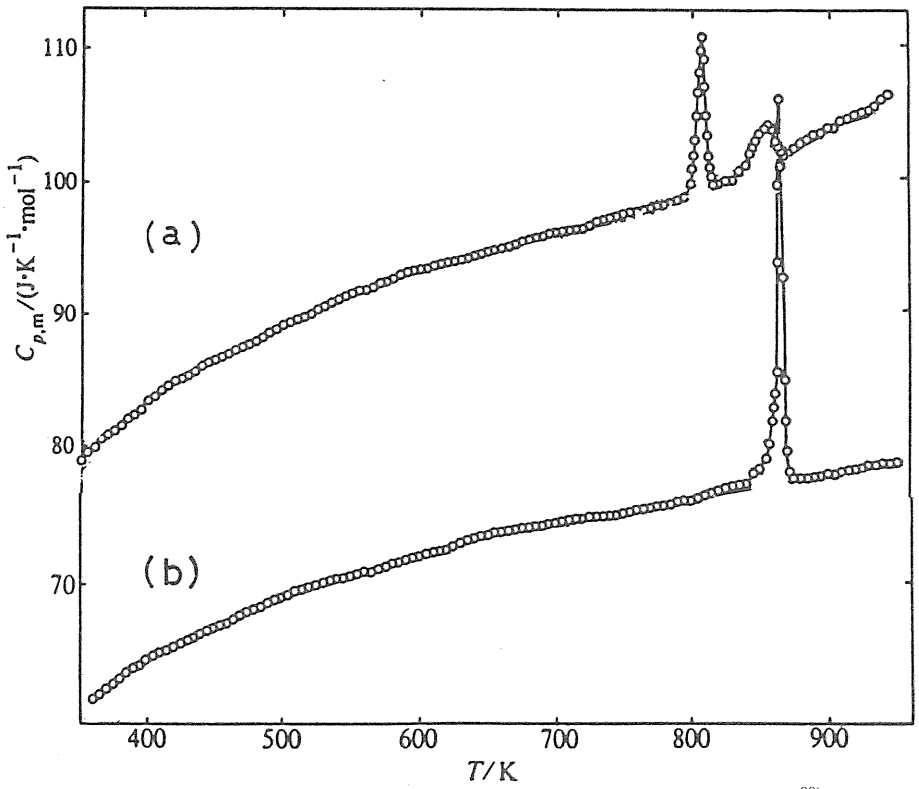

Fig. 27 Heat capacities of MoO_3 (a) and MoO_2 (b) by the present authors[98].

(e) MoO_2 and MoO_3

Heat capacities of MoO_2 and MoO_3 were measured by the authors in the range between 350 and 950 K by adiabatic scanning calorimeter[98]. In Fig. 27 (a), two heat capacity anomalies were found for MoO_3 at 808 and 857 K, while neither anomaly had been reported in the result by the drop method[98]. In Fig. 27 (b), a sharp heat capacity anomaly was observed for MoO_2 at 865 K, which also had not been reported by drop calorimetry[98]. The origin of the heat capacity anomaly found in MoO_3 and MoO_2 is inferred as arising from the slight movement of distorted MoO_6 octahedra in the MoO_2 and MoO_3 structure. Two heat capacity anomalies are found in MoO_3 since MoO_3 has a layered structure producing two kinds of relaxations of MoO_6 octahedra in two directions.

2. 2. 5. *Spinels*

As corrosion products in the coolant system of a nuclear water reactor, various kinds of spinels such as $Cr_xFe_{3-x}O_4$, $Co_xFe_{3-x}O_4$, etc. are formed. The spinels are also interesting materials from the viewpoint of high temperature chemistry.

The magnetic and electrical properties of spinel-type oxides are strongly influenced by the oxygen potential in the sample preparation and fabrication at high temperatures. Many spinel-type oxides are known to show the phase transitions due to the magnetic ordering as well as the cubic-tetragonal transition resulting from the cooperative Jahn-Teller effect. The chemical potential diagram and heat capacity data at high temperatures are thought to be important basic data for the spinel-type oxides. The λ-type heat capacity anomaly due to the ferri-paramagnetic transition was observed for $Mn_xFe_{3-x}O_4$ (x=1.0, 1.5 and 2.0)[99] and $Cr_xFe_{3-x}O_4$ (x=0.6, 0.8 and 1.0)[100]. The transition mechanism was mentioned in detail in our previous review[1].

(a) $MnFe_2O_{4\pm x}$

$MnFe_2O_4$ is a spinel of $Mn_xFe_{3-x}O_4$ with x=1. The phase equilibrium of *Mn-Fe-O* system with *Fe/Mn*=2 was studied by the authors under various oxygen partial pressures by means of thermogravimetry. Fig. 28 shows the oxygen partial pressures against reciprocal temperature for *Mn-Fe-O* system with *Fe/Mn*=2[101]. In the figure, the phase boundary of two phases (spinel and spinel+hematite) and that of three phases (spinel+hematite and hematite+bixbyite) are given by solid and dotted lines, respectively, while the values at a constant composition within a single phase of manganese ferrite are shown by broken lines. The standard enthalpy and entropy changes per one mole oxygen for the phase boundary reaction between spinel and spinel+hematite were calculated from thermogravimetric data[101].

(b) $Cu_{1-x}Ni_xCr_2O_4$

Many magnetic spinel-type oxides are known to show the phase transitions due to the cooperative Jahn-Teller effect as well as those due to the magnetic ordering. The heat capacities of $Cu_{1-x}Ni_xCr_2O_4$[102] with x values of 0.0, 0.2, 0.5, 0.7, 0.85 and 1.0 were measured by the authors in the range 220 to 960 K.

The typical results of the heat capacity measurement for $Cu_{0.3}Ni_{0.7}Cr_2O_7$ and $Cu_{0.5}Ni_{0.5}Cr_2O_4$ are shown in Fig. 29. A λ-type heat capacity anomalies due to the cooperative Jahn-Teller effect are seen in the figure. The excess heat capacities due to λ-type anomaly observed were compared with those calculated by assuming cubic-tetragonal transition resulting from the cooperative Jahn-Teller effect with the theoretical model by Kataoka and Kanamori[103].

The transition temperatures, enthalpy and entropy changes due to the transition obtained are listed in Table 5, comparing with the calculated values from the model by Kataoka and Kanamori[103]. In this model, the bulk distortions of mixed crystals are assumed to be

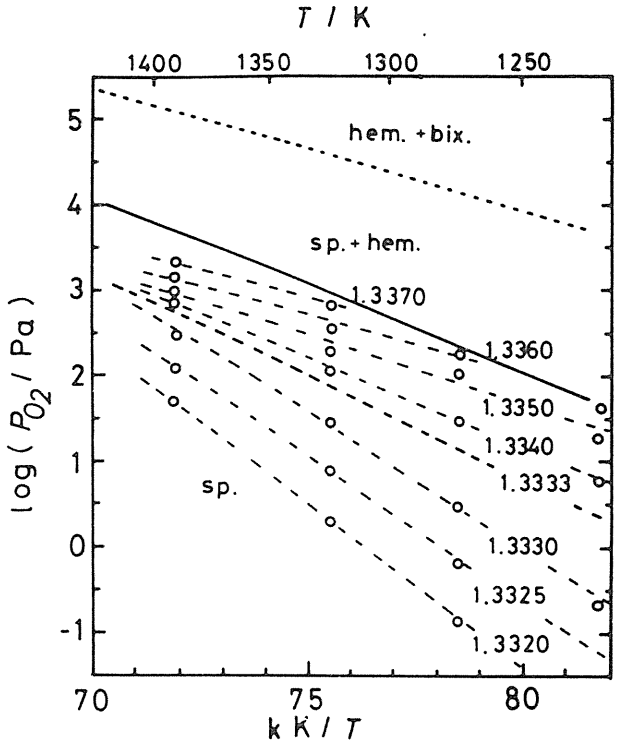

Fig. 28 The oxygen partial pressures against reciprocal temperature for *Mn-Fe-O* system with *Fe/Mn* = 2[101].

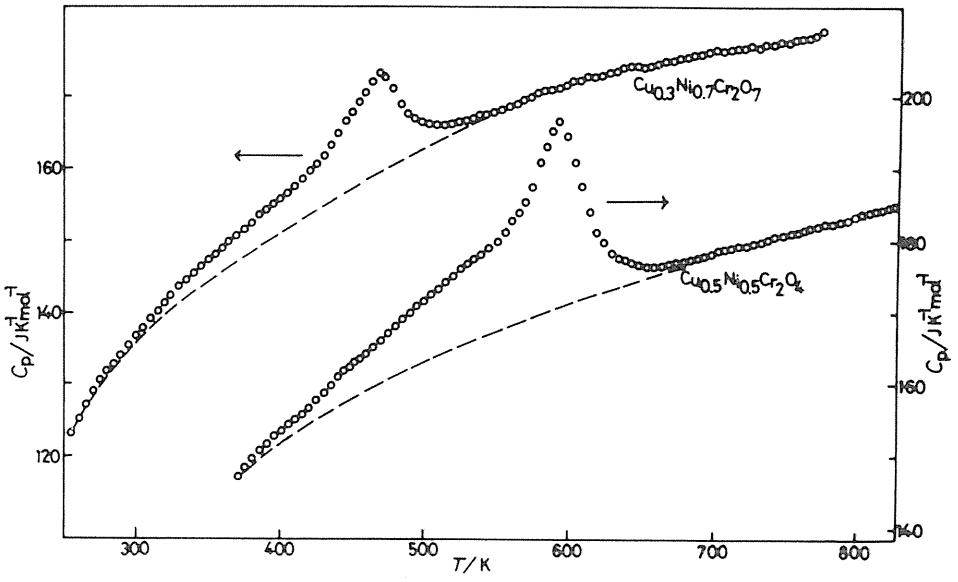

Fig. 29 The typical results of the heat capacity measurement for $Cu_{0.3}Ni_{0.7}Cr_2O_7$ and $Cu_{0.5}Ni_{0.5}Cr_2O_4$[102].

Table 5 The calculated and observed results of transition temperatures (t_{c2}), enthalpy change (ΔH), and entropy change (ΔS) due to the cubic-tetragonal transition for $Cu_{1-x}Ni_xCr_2O_4$[102].

Sample : x in $Cu_{1-x}Ni_xCr_2O_4$	t_{c2} (K)		ΔH (kJ mol^{-1})		ΔS (JK^{-1} mol^{-1})	
	calculated	observed	calculated	observed	calculated	observed
0.0	865	862	6.74	6.38	9.13	8.69
0.2	741	768	4.96	5.47	7.98	7.99
0.5	556	590	2.77	2.34	6.07	4.29
0.7	437	469	1.39	1.21	3.52	2.86
0.85	354	355	0.26	0.89	0.63	2.59
1.00	302	309	2.35	—	9.13	—

calculated on the basis of a Hamiltonian, which consists of the elastic energy, the energy of the lattice vibrations, the interaction between the electronic states of each ion and the uniform strains originating in the crystalline field, and the interaction between the electronic states and relative displacements. As seen in the table, the agreement between the observed and the theoretical results is fairly good, considering the errors in the experiment and theoretical calculation[103].

2. 2. 6. *Superconducting oxide $Ba_2YCu_3O_{7-x}$*

The superconducting material itself is not the nuclear reactor material, but an important material from the point view of plasma confinement and also a very interesting material from the point of view of solid state chemistry.

The study on the oxygen nonstoichiometry x in $Ba_2YCu_3O_{7-x}$ has been carried out by Kishio et al.[104] and Gallaghar[105]. Their data agree fairly well each other, but no clear change was found in the slope of the oxygen nonstoichiometry x vs. the oxygen partial

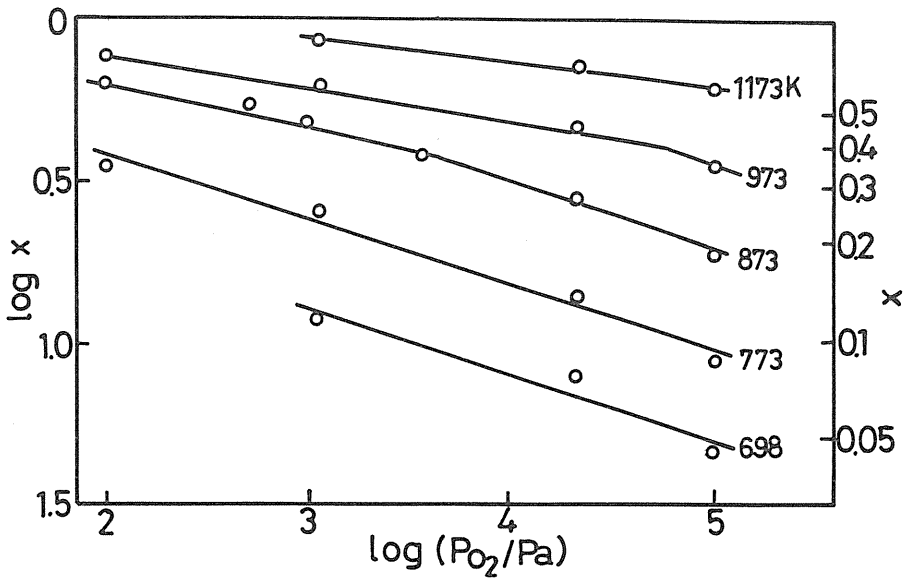

Fig. 30 Variation of log x in $Ba_2YCu_3O_{7-x}$ with log Po_2[109].

pressure relating to the occurrence of the phase transition from the tetragonal to the orthorhombic structure reported by means of high temperature X-ray diffractometry[100,101] and the electrical conductivity measurement[108].

The oxygen nonstoichiometry x in $Ba_2YCu_3O_{7-x}$ was measured by thermogravimetry as a function of oxygen partial pressure and temperature over the ranges $10^2 \leqq Po_2/Pa \leqq 10^5$ and $698 \leqq T/K \leqq 1173$ by the authors[109]. The oxygen partial pressure dependence of x is shown in Fig. 30. In this figure, two regions with different dependences of x upon Po_2 are seen. In the compositional region with small x values ($x \leqq 0.3$), the slope values of $\partial \log Po_2/\partial \log x$ ($=n$) are about 5, irrespective of temperature from 698 to 873 K. In the compositional region with large x values ($x \geqq 0.4$), the slope values, n, are about 10, irrespective of temperatures from 873 to 1173 K. At 873 K the n value changed from 5 to 10 around $x=0.4$. The difference in the n values from 5 to 10 is thought to be indicative of the occurrence of the phase transition from the orthorhombic (I) to the tetragonal structure. Although $n \simeq 5$ in the orthorhombic (I) phase seems to be simply interpreted by assuming the co-presence of the singly and doubly charged oxygen vacancies as the predominant defects, a simple defect may not be applied for $Ba_2YCu_3O_{7-x}$, since the distribution of the oxygen vacancies is not random. According to the structural studies, it was concluded that (1) the one-dimensional-*O-Cu-O-Cu-O-* chains along the a-axis on the plane sandwithched between the two adjacent *Ba* planes lose their oxygen atom and produce the ordering of oxygen vacancies in the low temperature (low x-value) orthorhombic phase, and (2) the disordering of the oxygen vacancies relates to the orthorhombic-to-tetragonal phase transition. The defect structure including the distribution (ordering) of the oxygen vacancies and/or interaction between oxygen vacancy and copper ion may be more appropriate than the simple oxygen vacancy model.

2. 2. 7. Th_3N_4 and Th_2N_2O

The Th_3N_4 and Th_2N_2O are the potential nuclear fertile materials for fast breeder reactors. These compounds, however, are poorly investigated compared with uranium nitrides.

The electrical conductivities of Th_3N_4 and Th_2N_2O[110] were measured by the authors as a function of nitrogen partial pressure in the temperature range from 1273 to 1473 K and its results are shown in Fig. 31. The electrical conductivity increases with decreasing nitrogen partial pressure, suggesting n-type semiconduction of Th_3N_4 and Th_2N_2O over the temperature range measured. As seen in the figure, the slope of the plots of log σ vs log P_{N_2} becomes smaller in the higher nitrogen partial pressure region and the deviation from the straight line occurs therefore at higher nitrogen partial pressure with increasing temperature. This behavior may be explained either by the contribution of ionic conduction or by the presence of some impurities.

As the crystal structure of Th_3N_4 is closely related to that of Th_2N_2O and the nitrogen partial pressure dependence of the electrical conductivity of both Th_3N_4 and Th_2N_2O samples is nearly the same value of $-1/8$, the defect structures of Th_3N_4 and Th_2N_2O may be explained by triply ionized nitrogen vacancies[110].

2. 2. 8. *Metallic fuels*

Metallic alloys such as *U-Pu-Zr* alloy have been recently recognized as the promising fuels in the fast breeder reactor. Heat capacity and thermal conductivity are the important thermophysical properties of the fuels to evaluate their thermal stability. Hence, *U-Zr* alloy was studied as a basic research of the *U-Pu-Zr* alloy.

(a) $U_{0.80}Zr_{0.20}$ alloy

The heat capacity and the electrical conductivity of $U_{0.80}Zr_{0.20}$ were measured by the authors by means of direct heating pulse calorimetry in the range from 300 to 1300 K[111].

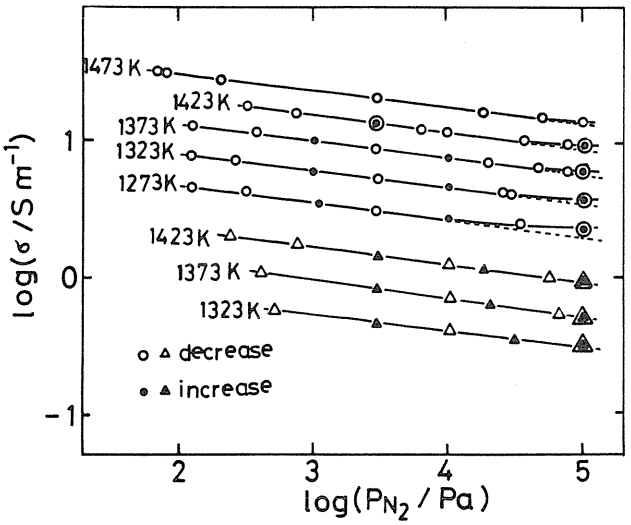

Fig. 31 The electrical conductivities of Th_3N_4 (○, ●) and Th_2N_2O (△, ▲) as a function of nitrogen partial pressure in the temperature range from 1273 to 1473 K[110].

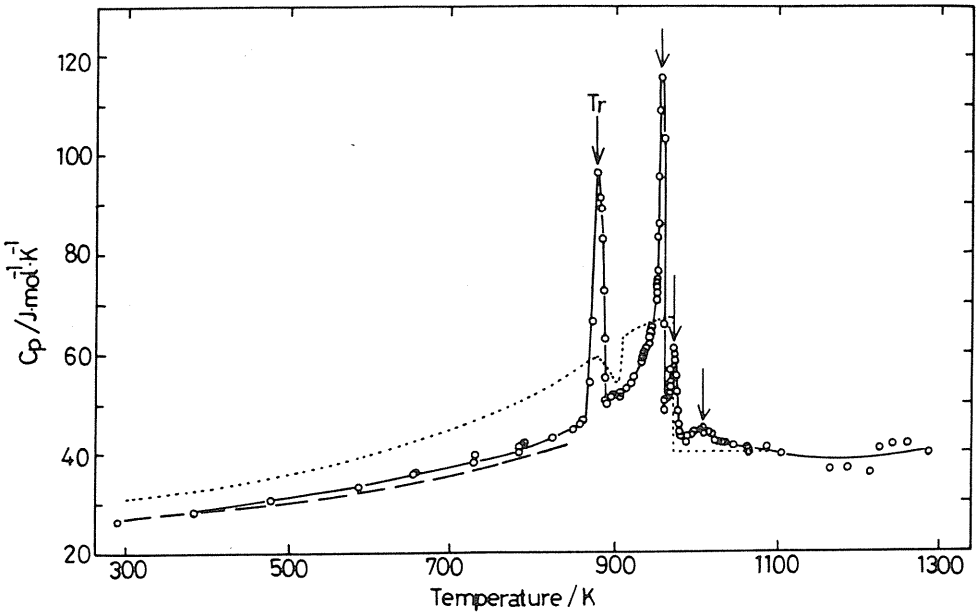

Fig. 32 Heat capacity of *U*-20 at % *Zr* alloy[111]
—○— Matsui et al.[111], ····· Fedorov and Smirnov[112], ----- calculated values from Kopp-Neuman's rule[111].

The heat capacity measured on $U_{0.80}Zr_{0.20}$ is shown in Fig. 32 together with that of $U_{0.87}Zr_{0.13}$ by Fedorov and Smirnov[112]. Four peaks were seen at 879, 957, 971 and 1011 K in the heat capacity of $U_{0.80}Zr_{0.20}$ corresponding to four phase transitions ($\alpha+\delta \rightarrow \alpha+\gamma$ phases, $\alpha+\gamma \rightarrow$

$\beta+\gamma$, $\beta+\gamma \rightarrow \gamma_1+\gamma_2$, $\gamma_1+\gamma_2 \rightarrow \gamma$). The transition temperatures were fairly in good agreement with those estimated from the phase diagram reported previously[113]. The thermal conductivity of $U_{0.80}Zr_{0.20}$ calculated from both the heat capacity[111] and the thermal diffusivity[114] is shown in Fig. 33 together with those previously reported[115,116] and is seen to be very close to that of $U_{0.75}Zr_{0.25}$ experimentally determined by Leibowitz et al.[115] The thermal conductivity of $U_{0.80}Zr_{0.20}$ calculated on the basis of the Wiedemann-Franz's law from the electrical conductivity simultaneously measured with heat capacity[111] is a little lower than that calculated from the heat capacity and the experimental one by Leibowitz et al[115].

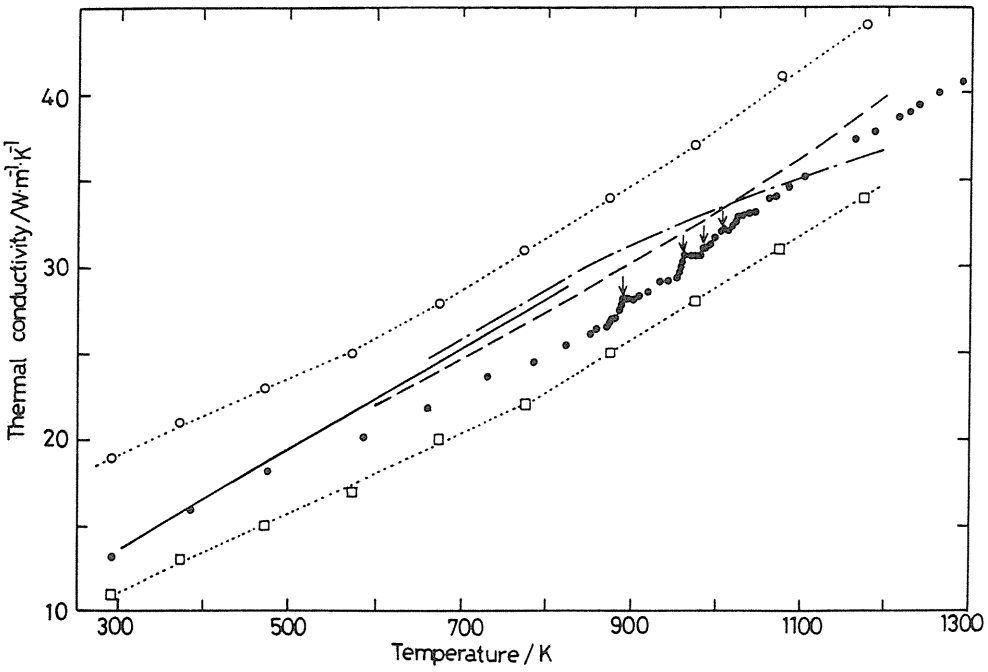

Fig. 33 Thermal conductivity of *U*-20 at % *Zr* alloy[111]

—— calculated values of $U_{0.80}Zr_{0.20}$ from the heat capacity and the thermal diffusivity[111],
● calculated values of $U_{0.80}Zr_{0.20}$ from the electrical conductivity based on the Wiedemann-Franz's law[111]
—·— experimental values of $U_{0.75}Zr_{0.25}$ by Leibowitz et al[115],
– – experimental values of $U_{0.75}Zr_{0.25}$ during the years of 1954,
—— 1958 reported by Leibowitz et al[115],
○···○ experimental values of $U_{0.88}Zr_{0.12}$[116],
□···□ experimental values of $U_{0.52}Zr_{0.48}$[116].

(b) $U_{0.80}Mo_{0.20}$ alloy

The heat capacity and the electrical conductivity of $U_{0.80}Mo_{0.20}$ were also measured by direct heating pulse calorimetry in the range from 300 to 1150 K. The result on the heat capacity is shown in Fig. 34. The heat capacity of *U-Mo* alloy has not been measured above 5 K. Two peaks were observed at 833 and 847 K in the heat capacity curve corresponding to phase transitions ($\alpha+\gamma' \rightarrow \alpha+\gamma$, $\alpha+\gamma \rightarrow \gamma$). The transition temperatures thus obtained are in

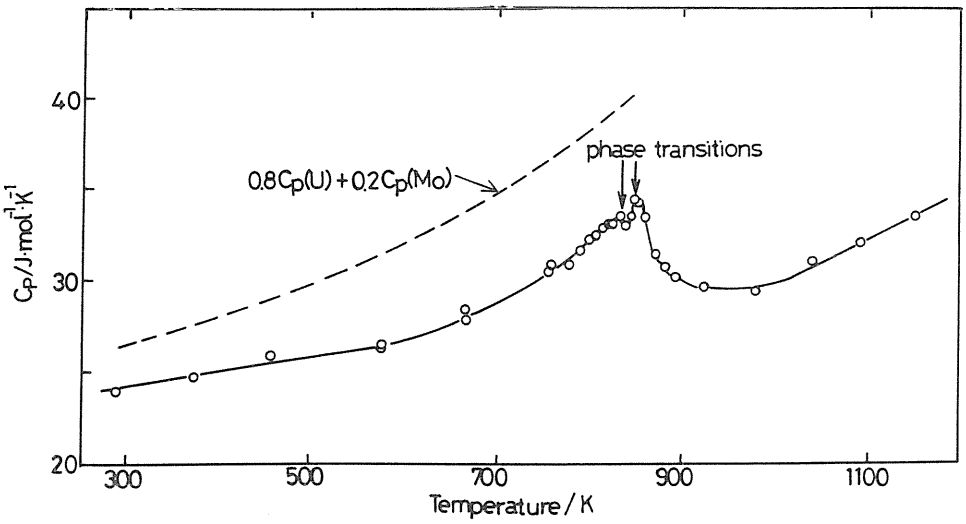

Fig. 34 Heat capacity of *U*-20 at %*Mo* alloy[111].
Matsui et al[111], — — calculated values from Kopp-Neuman's rule[111]

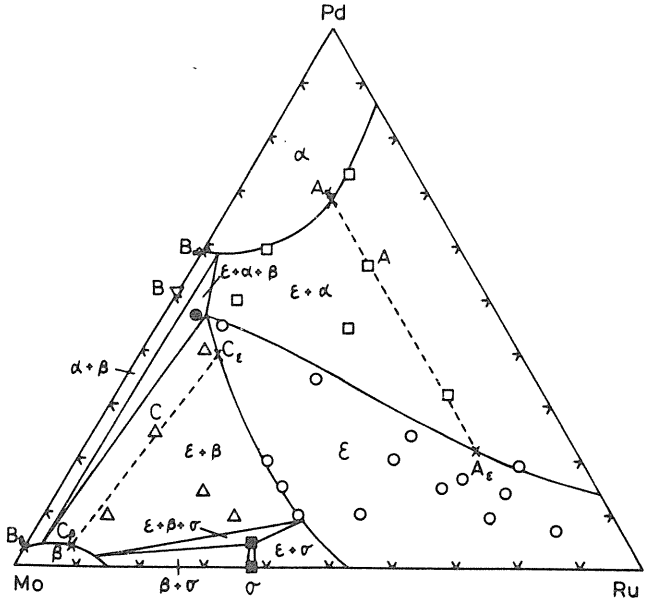

Fig. 35 Phase diagram of the ternary *Mo-Ru-Pd* system at 1723 K[119].
α: solid solution (fcc), ε: solid solution (hcp), σ: intermetallic compound of Mo_5Ru_3 (tetragonal), β: solid solution (bcc), ○: ε, □: $\varepsilon+\alpha$, △: $\varepsilon+\beta$, ▽: $\alpha+\beta$, ●: $\varepsilon+\alpha+\beta$, ■: σ

good agreement with those estimated from the phase diagram[113]. The thermal conductivity of $U_{0.80}Mo_{0.20}$ was calculated from the electrical conductivity on the basis of the Wiedemann-Franz's law[111], which fell between the experimental values of $U_{0.77}Mo_{0.23}$[117] and $U_{0.88}Mo_{0.12}$[126].

2. 2. 9. Fission-produced noble metal alloys

(a) *Mo-Ru(Tc)-Pd(Rh)* alloys

It is known from many post-irradiation test that fission-produced noble metals (*Ru, Rh, Pd*) form fine metallic inclusions together with *Mo* and *Tc*. The chemical states of these noble metals in the fuel depend on the temperature, oxygen potential, burnup, etc. The phase diagram of this system and the vapor pressures of each constituent at various temperatures and oxygen partial pressures are of importance to know the behavior of these metals in the fuel or in the case of severe accident of nuclear reactor. In the metallic inclusions, it is also known that *Tc* and *Rh* form complete solid solution with *Ru* and *Pd*, respectively. Hence, the ternary system consisting of *Mo-Ru-Pd* is often used for the experiments[119-121].

Four reports[119,122-124] are now available for the phase diagrams of the ternary system between *Mo, Ru* and *Pd*. The phase diagram of the ternary *Mo-Ru-Pd* system at 1723 K in vacuum determined by means of optical microscopy, X-ray diffractometry and electron probe microanalysis by the authors is shown in Fig. 35[119]. It was found that the ε-phase region decreases with decreasing ruthenium content and finally coexists with α and β phases and that the σ-phase region is very small at 1723 K. The phase diagram was calculated by the authors from the regular solution model proposed by Kaufman and Bernstein[125], and the comparison with the phase diagram obtained experimentally showed a fairly good accordance in some extent.

The vapor pressures over the ε-phase of *Mo-Ru-Pd* alloys were measured by mass spectrometry in the temperature range 1536−1791 K[119,120]. From the thermodynamic activity of *Mo, Tc, Ru, Rh* and *Pd* in *Mo-Ru(Tc)-Pd(Rh)* alloys calculated based on the regular solution model, the vapor pressures of $Mo(g)$, $Tc(g)$, $Ru(g)$, $Rh(g)$ and $Pd(g)$ were obtained as a function of composition of alloys and temperature and shown in Fig. 36 compared with those of $Mo(g)$ and $Pd(g)$ obtained experimentally[121]. It is seen from Fig. 36 that the vapor pressures of $Pd(g)$ and $Mo(g)$ experimentally obtained are in good agreement with calculated ones, indicating that the regular solution model is fairly appropriate for the thermodynamic calculations of these alloys. Using the thermodynamic activities thus calculated, the equilibrium partial pressures of metal gas and gaseous oxide species can be calculated as a functions of temperature and oxygen partial pressure. Vapor pressures of various gaseous species over the systems of *Mo-O, Tc-O, Ru-O, Rh-O* and *Pd-O* were calculated[121] and the result on the *Ru-O* system as an example is shown in Fig. 37[121].

(b) *Pd-Zr* alloys

Thermodynamic data on *Pd-Zr* alloys are of importance in relation to the development of metal-fuelled fast breeder reactors, since zirconium is one of the constituents of the promising *U-Pu-Zr* metallic fuel. In order to predict the behavior of fission produced palladium in such a fuel, the relative stability of the possible reaction products must be known.

The partial vapor pressures of *Pd* over the *Zr-Pd* solid solution ($Pd(ss)$) and over the two-phase mixtures $Pd(ss)+Pd_3Zr$ and Pd_3Zr+Pd_2Zr were determined by means of mass-spectrometry[127]. From the Gibbs energies of formation for $Pd(ss)$, Pd_3Zr and Pd_2Zr obtained from the vapor pressure data together with those of PdO[128], ZrO_2[129], $Pd_3Zr_6O_x$[130] and $PdZr_2$[131], the phase diagram of the ternary *Pd-Zr-O* system was calculated by the authors[127]. Considering the phase diagram at 700 K which corresponds approximately to the temperature of the zircaloy cladding at normal operational condition, the equilibrium oxygen

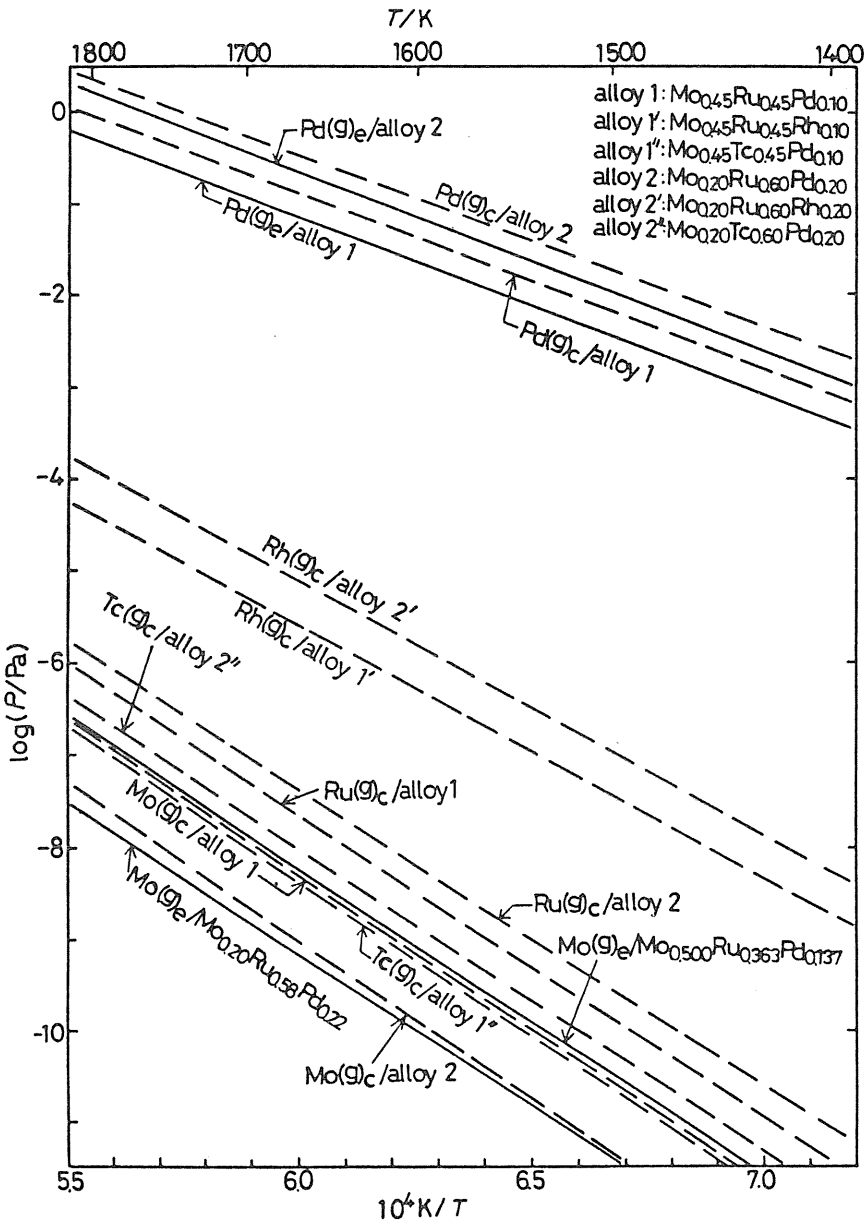

Fig. 36 Temperature dependences of vapor pressures of *Mo(g)*, *Ru(g)* an *Pd(g)* over *Mo-Ru-Pd* alloys, *Rh(g)* over *Mo-Ru-Rh* alloys and *Tc(g)* over *Mo-Tc-Pd* alloys[121].

– – $Mo(g)_c$, $Ru(g)_c$, $Pd(g)_c$, $Tc(g)_c$: calculated values on the basis of the regular solution model over alloys[121]

—— $Pd(g)_e$: experimental values for *Mo-Ru-Pd* alloys[121]

—— $Mo(g)_e$: extrapolated values for $Mo_{0.500}Ru_{0.363}Pd_{0.137}$ and $Mo_{0.20}Ru_{0.58}Pd_{0.22}$ from the EMF data experimentally obtained in the range 1200–1300 K by Yamawaki et al[126].

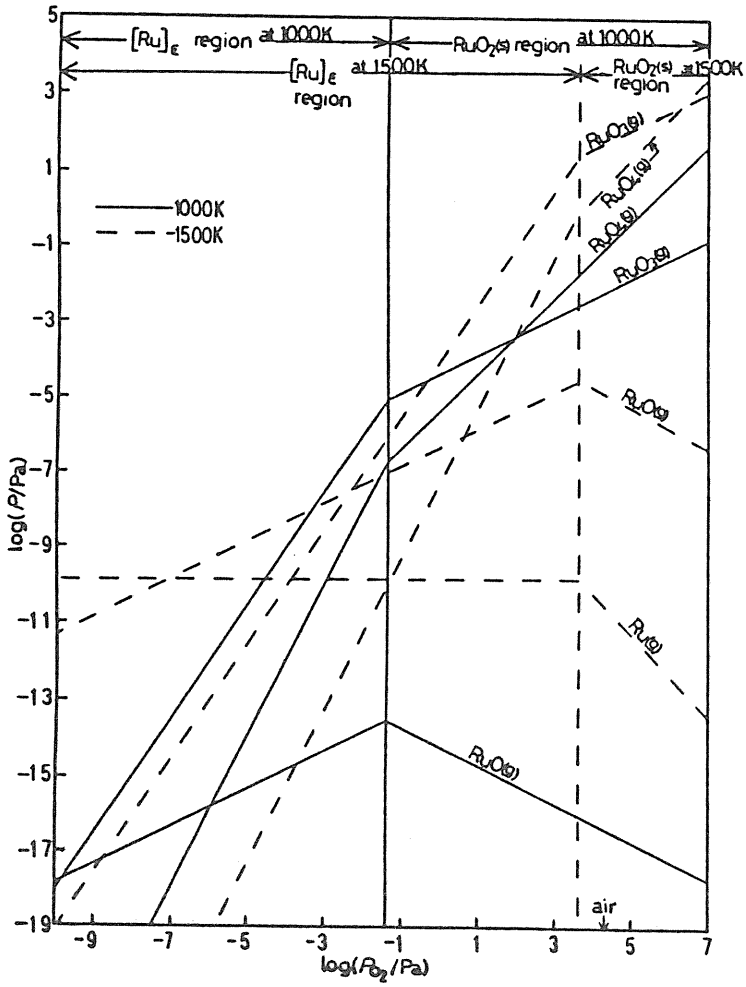

Fig. 37 Vapor pressures of various gaseous species containing *Ru* over $Mo_{0.450}Ru_{0.450}Pd_{0.100}$ (alloy 1) and $RuO_2(s)$ as a function of oxygen partial pressure at 1000 and 1500 K[126].

potential of high burnup fast breeder fuel at the inner surface of the cladding and that of stoichiometric UO_2, and the palladium activity determined by $(U,Pu)Pd_3$ or $ZrPd_3$ which is thought to be present in that gap, the most stable reaction product under normal operational conditions was concluded to be ZrO_2.

III. Diffusion Studies

3. 1. Definition of diffusion coefficients

In this section the results on the self-, tracer- and chemical diffusion coefficients in oxides, sulfides and tellurides measured in our laboratory are summarized. Prior to the review, it may be better to mention about the definition of these coefficients briefly.

The tracer-diffusion coefficient is the most basic coefficient and can be defined as the diffusion coefficient of a tracer isotope (in a very dilute concentration) under the concentration gradient of the tracer itself in an otherwise homogeneous crystal. The self-diffusion coefficient is the diffusion coefficient of an atom under random walk condition in a homogeneous crystal where the successive atom jumps were independent of one another and of the direction of previous jumps. The chemical-diffusion coefficient is sometimes called as interdiffusion coefficient and can be defined as the diffusion coefficient under the concentration gradient of atom(s) in an inhomogeneous crystal.

The relationship between the chemical($\tilde{D}$) and the self(D)-diffusion coefficient derived by Wagner[134] is given by

$$\tilde{D} = t_e (Z_1 D_1 + |Z_2| D_2)/|Z_2| (C_1/C_d) \left(\frac{1}{RT} \frac{\partial \mu_2}{\partial ln C_d} \right), \tag{15}$$

where subscripts 1 and 2 denote cation and anion, respectively, C_1 and C_d are the concentrations of cation and defects, and μ the chemical potential. Z_1 and Z_2 denote numbers of charge of cations and anions, and t_e is the electronic transport number. For example in the case of NbO_2[135], the following values are assigned to the parameters in Eq. (15): $t_e=1$ (metallic or non ionic conductor), $D_1 \gg D_2$ (predominant cation diffusion), $Cd=C_v=x$ (the concentration of niobium vacancies in the nonstoichiometric $Nb_{1-x}O_2$), $(\partial ln\, Po_2/\partial ln\, Cd)=1$ (niobium vacancy model), $Z_1=4$ and $|Z_2|=2$. Therefore the Eq. (15) can simply be given by

$$\tilde{D} = (D_1 C_1/C_v)(\partial ln\, Po_2/\partial ln\, C_v) = D_1/x. \tag{16}$$

The self-diffusion coefficient of niobium ion (D_1) is related to the diffusion coefficient of niobium vacancy (D_v) by the expression

$$D_1 C_1 = D_v C_v, \tag{17}$$

since vacancies jump into neighboring lattice sites and ions on the sites jump in the reverse directions in the case of the vacancy diffusion mechanism. From Eqs. (16) and (17), the diffusion coefficient of niobium vacancies (D_v) is equal to the chemical diffusion coefficients ($\tilde{D}$) as the equation:

$$D_v = C_1 D_1/C_v = \tilde{D}. \tag{18}$$

The tracer diffusion coefficient (D_1^*) is also related to the self-diffusion coefficient of niobium ions (D_1) by the equation:

$$D_1^* = D_1 f, \tag{19}$$

where f is the correlation factor. The correlation factor can be calculated from the diffusion mechanism (such as vacancy or interstitial etc.) and the crystal structure of the sample.

3. 2. Apparatus and method

3. 2. 1. Sectioning method for tracer diffusion

Sectioning method using radioactive tracer has been widely used for measuring tracer diffusion coefficients (D^*). When an infinitely thin film of the tracer is assumed to be deposited on a semi-infinite solid, the solution of the diffusion equation for the tracer under

these conditions is given by

$$C(y,t) = \frac{C_o}{\sqrt{\pi D^* t}} \exp\left(-\frac{y^2}{4D^* t}\right), \tag{20}$$

where C is the tracer concentration, C_o the total integral concentration of tracer, y the distance from the surface, t the diffusion time and D^* the tracer diffusion coefficient. The value of D^* is determined from the slope of the plot of log C vs. y^2 at a time t.

3. 2. 2. Mössbauer line-broadening method for self-diffusion

Singwi and Sjölander[135] predicted that the zero-phonon Mössbauer resonance should broaden in proportion to the diffusivity. For polycrystalline samples, the Mössbauer diffusional line broadening, $\Delta\Gamma$, is determined by the average jump frequency, $\bar{\nu}$, of the elementary displacement process,[136,137]

$$\Delta\Gamma = 2\,\hbar\nu \tag{21}$$

The diffusion coefficient, D, is represented according to the random walk theory by the following equation,

$$D = g\,r_o^2 f / \bar{\nu}\,, \tag{22}$$

where g is a geometric factor, r_o the nearest-neighbour distance and f the correlation factor[138].

The line broadenning, $\Delta\Gamma$, is determined by subtracting the minimum reference linewidth, Γ_o, from the observed linewidth, Γ, where Γ_o is the linewidth when the diffusion does not occur. If the diffusion mechanism is assumed to be identical in the temperature range studied, the minimum linewidth is calculated by a computer fitting for observed values of Γ and T to the following equation containing three parameters: Γ_o, $(\Delta\Gamma)_o$ and E,

$$\Delta\Gamma = \Gamma - \Gamma_o = (\Delta\Gamma)_o \exp\left(-\frac{E}{RT}\right), \tag{23}$$

where Γ is the observed linewidth at a temperature T, $(\Delta\Gamma)_o$ the preexponential term and E the activation energy of atomic diffusion.

Mössbauer spectra were obtained using a transducer driven by a trianguler waveform generator with a 25 mCi ^{57}Co/Rh source, a PR gas flow proportional counter and a multichannel analyzer. The isomer shifts are quoted with respect to iron foil at 295 K.

The furnace for Mössbauer spectroscopy at high temperature is shown in Fig. 38[137] and consists of quartz heating-element, Kantal heating wire and stainless steel vessel. The sample was placed in the furnace and heated up to about 1073 K in vacuum for the observation of the Mössbauer diffusional line broadening.

3. 2. 3. Thermogravimetric and electrochemical relaxation method for $\tilde{D}$

The chemical diffusion coefficient ($\tilde{D}$) in oxide is usually determined by observing the relaxation phenomena of compositional deviations responding to a stepwise change in oxygen partial pressure through monitoring electrical conductivity change or weight change. The weight change can be precisely measured as a function of time with an automatic recording electro-microbalance. The weight of a cylindrical sample with a size of $2a$ in diameter and $2b$

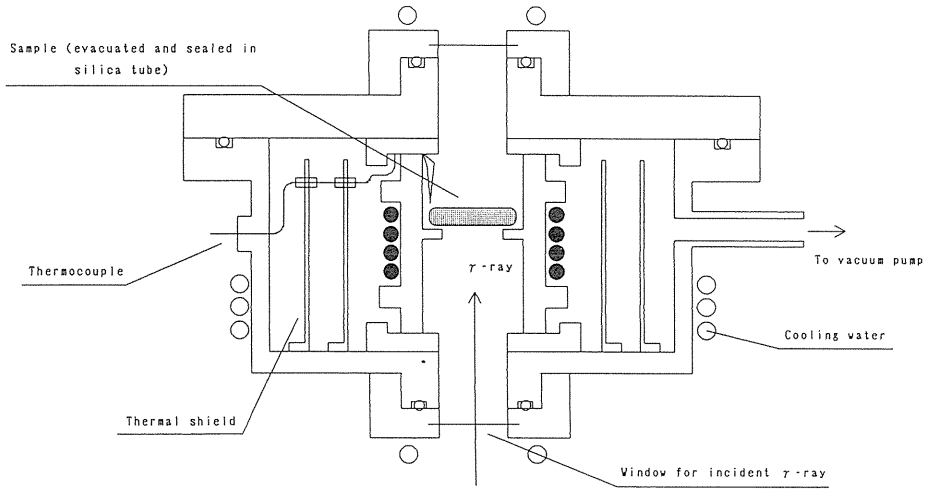

Fig. 38 The furnace for Mössbauer spectroscopy at high temperature[137].

in thickness is shown to change with time t in accordance with the following equation[139] after sufficiently long time ($[W(t)-W(o)]/W(\infty)-W(o)] \geqq 0.5$):

$$\log\left(\frac{W(\infty)-W(t)}{W(\infty)-W(o)}\right) = -0.252 - \frac{1}{2.303}\left(\frac{(2.405)^2}{a^2} + \frac{2}{4b^2}\right)\tilde{D}t, \tag{24}$$

Where $W(o)$, $W(\infty)$ and $W(t)$ are the initial weight, the final equilibrium weight and the weight at t, respectively. From the values of the slope of the logarithmic plot of weight change against time, the chemical diffusion coefficient can be calculated.

Since it is very difficult to measure the chemical diffusion coefficient in metallic conductors whose electrical conductivity is independent of oxygen partial pressure and that in the materials whose homogeneity range is very narrow, the electrochemical relaxation method was recently developed for the determination of $\tilde{D}$[135,140-143]. In the electrochemical methods a solid electrolyte is used and it can be divided into two classes: potentiostatic and galvanostatic techniques. In the potentiostatic technique, the constant voltage is applied to the sample and the resultant current flow through the sample is monitored as a function of time. On the other hand, in the galvanostatic technique the constant current is applied and the resultant voltage drop is monitored as a function of time. The advantage and disadvantage of these two techniques were discussed previously in our papers[135,141]. Here the theory of the electrochemical potentiostatic technique is described briefly and this technique was used for the determination of $\tilde{D}$ in NbO_2 with very narrow homogeneity range[135,141]. The galvanic cell used for the determination of $\tilde{D}$ is

$$\underset{\text{I}}{Pt(1) \mid ZrO_2\ (15\,\text{mol\%}\ CaO \text{ or } Y_2O_3)} \mid \underset{\text{II}}{NbO_2} \mid \underset{\text{III}}{Pt(2)}. \tag{25}$$

The calcia-(or yttria) stabilized zirconia in this cell acts so as to change the oxygen potential

at interface II. $Pt(1)$ is a porous platinum electrode and $Pt(2)$ is a platinum disk. The $Pt(2)$ disk is used for blocking oxygen flow into the atmosphere, out of the sample, through interface III. At first this cell was set in equilibrium, i.e. an equilibrium chemical potential of oxygen throughout the sample was attained and then the constant voltage (E) was suddenly applied. If the $Pt(1)$ and $Pt(2)$ electrodes are anode and cathode, respectively, the chemical potential of oxygen at the boundary II is suddenly decreased by E. The chemical diffusion coefficient ($\tilde{D}$) can be determined by monitoring the change in current through the sample as a function of time and applying Fick's first and second law[144] with the following initial and boundary conditions:

$$C = C_0, \ (O \leqq x \leqq L, \ t = 0), \tag{26}$$

$$C = C_1, \ (x = 0, \ t > 0), \tag{27}$$

$$\partial C/\partial x = 0, \ (x = L, \ t > 0), \tag{28}$$

where C is the oxygen concentration in the sample, x, the distance from interface II, and L the sample thickness. The electric current I through the sample is

$$\mathrm{I} = \frac{4eA(C_1 - C_0)\tilde{D}}{L} \sum_{m=0}^{\infty} \exp\left[-\frac{(2m+1)^2 \Pi^2 \tilde{D}}{4L^2} t\right] + \mathrm{I}_{st}, \tag{29}$$

where A is the cross-sectional area of the sample in contact with the solid electrolyte, e is the elementary electric charge, and I_{st} is the contribution of electronic current flow through the zirconia solid electrolyte. The current, I, is monitored during the relaxation process and fitted to Eq. (29) with the aid of a computer, then $\tilde{D}$[141] is determined from Eq. (29).

3. 3. *Self-diffusion (Tracer-diffusion)*

The radioactivity buildup around the primary coolant system of nuclear water reactor is caused mainly by ^{60}Co and ^{58}Co deposited on the structural material. The corrosion products formed on the structural material are corundom- and/or spinel-type oxides which contain the cations of iron, chromium, nickel, etc. The diffusion data of cations in these oxides are needed to understand corrosion mechanism.

The tellurium is a corrosive fission product having the fission yield of about 1% in fast breeder reactor and may attack the inner surface of fuel pins made of stainless steel to form iron tellurides. Iron sulfides as well as tellurides have a hexagonal NiAs-type structure with iron vacancies. The diffusion mechanism of iron in these iron chalcogenides are interested in the viewpoint of high temperature chemistry.

3. 3. 1. *Iron and cobalt in α-$(Fe_{0.80}Cr_{0.20})_2O_3$ and $(Fe_{0.80}Cr_{0.20})_3O_4$*

The diffusion data of the cations in corundom- and spinel-type oxides are available for simple oxides such as α-Fe_2O_3, α-Cr_2O_3 and Fe_3O_4, but those in α-$(Fe, Cr)_2O_3$ and $(Fe, Cr)_3O_4$ solid solutions have not been known.

The tracer diffusion coefficients of iron and cobalt in the sintered samples of α-$(Fe_{0.80}Cr_{0.20})_2O_3$ and $(Fe_{0.80}Cr_{0.20})_3O_4$ were measured by the authors[145] in air in the temperature range from 1498 to 1673 K and under controlled oxygen partial pressures at 1573 K, respectively. The densities of α-$(Fe_{0.80}Cr_{0.20})_2O_3$ and $(Fe_{0.80}Cr_{0.20})_3O_4$ sample pellets used in this measurement were 95 and 80% of the theoretical densities, respectively.

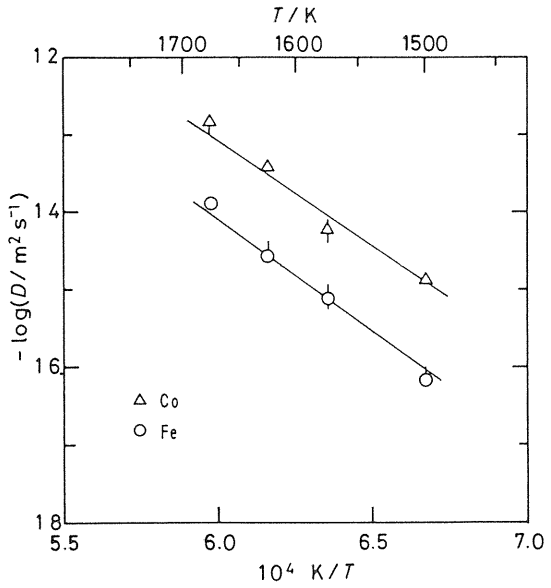

Fig. 39 The temperature dependence of diffusion coefficients of iron (o) and cobalt (△) in α-$(Fe_{0.80}Cr_{0.20})_2O_3$ sample in air[145].

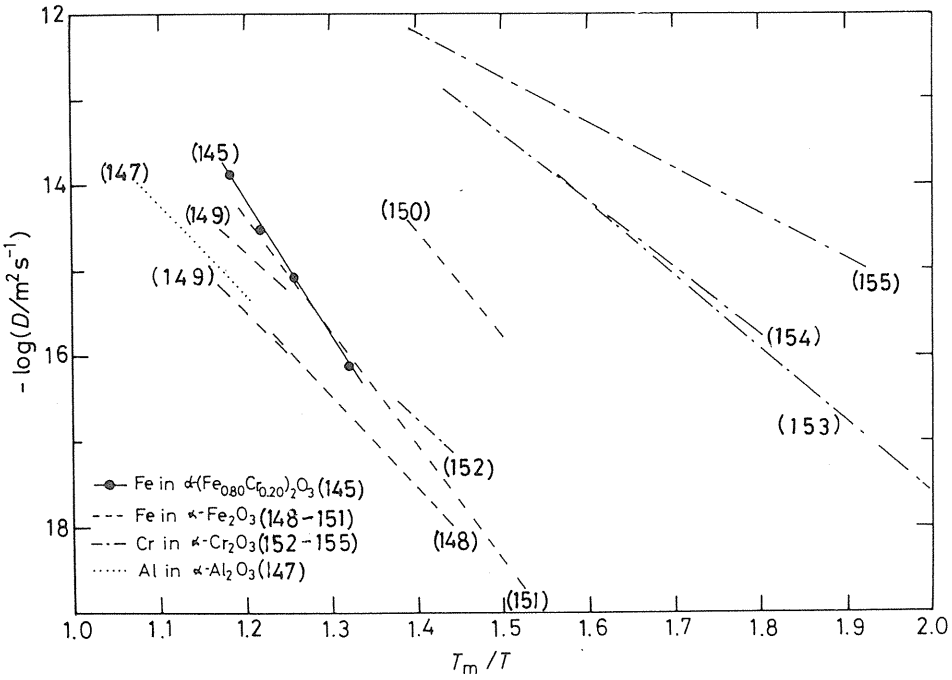

Fig. 40 Comparison of the cation diffusion coefficients in corundom-type oxides:
α-$(Fe_{0.80}Cr_{0.20})_2O_3$ by the present authors[145]
α-Al_2O_3[147], α-Fe_2O_3[148-151] and α-Cr_2O_3[152-155]
For the comparison, a normalized temperature scale is used (T_m = melting point in K).

Fig. 39 shows the temperature dependence of the diffusion coefficients of iron and cobalt in α-$(Fe_{0.80}Cr_{0.20})_2O_3$[145], and it is seen that the diffusion coefficients of cobalt in α-$(Fe_{0.80}Cr_{0.20})_2O_3$ are about one order of magnitude larger than those of iron, while the diffusion coefficients of iron and cobalt in $(Fe_{0.80}Cr_{0.20})_3O_4$[145] and those in Fe_3O_4[146] are nearly the same within the experimental error. The iron diffusion in $(Fe_{0.80}Cr_{0.20})_3O_4$ obtained by the authors[145] is not so different from that in Fe_3O_4 by Dieckmann et al.[146]

Since α-$(Fe_{1-x}Cr_x)_2O_3$ has corundom structure, the diffusion coefficient of iron in α-$(Fe_{0.80}Cr_{0.20})_2O_3$ was compared with those of cations in other oxides with corundom structure such as α-Al_2O_3[147], α-Fe_2O_3[148-151] and α-Cr_2O_3[152-155] in Fig. 40[145], where the normalized temperature by melting point, T/T_m, is used as abscissa. The iron diffusion behavior in α-$(Fe_{0.80}Cr_{0.20})_2O_3$ by the authors[145] is similar to the cation diffusion behavior in α-Al_2O_3[147], α-Fe_2O_3[148-150] and α-Cr_2O_3[152] except for a few references[150,153-155]. The difference might be caused by the grain boundary diffusion.

3. 3. 2. Iron in $Fe_{1-x}S$

The tracer diffusion coefficients of cation and anion in iron chalcogenides have been measured only for $Fe_{1-x}S$[156] but the self-diffusion coefficients of iron in $Fe_{1-x}S$ by Mössbauer diffusional line broadening have not been reported yet.

Diffusion broadening of the Mössbauer line of non-stoichiometric $Fe_{1-x}S$ (x=0.003, 0.03, 0.08 and 0.125) was measured by the authors[157,158] in the temperature range from 600 to 1073 K to compare with the tracer data[156]. Fig. 41[158] shows typical Mössbauer spectra of a $Fe_{0.997}S$ sample close to the stoichiometric composition in the temperature range from 295 to 1073 K. Fig. 42[158] shows the plots of the Mössbauer diffusional line broadening, $\Delta\Gamma$, for the samples with various nonstoichiometries against reciprocal temperature. The activation energies for $Fe_{0.997}S$, $Fe_{0.970}S$, $Fe_{0.920}S$ and $Fe_{0.875}S$ samples are 65, 75, 70 and 55 kJ · mol^{-1}, respectively, which are in fairly good agreement with 81, 83, 87 and 91 kJ · mole^{-1}, respectively, by the tracer technique reported by Condit et al.[156] except $Fe_{0.875}S$ sample. Fig. 43[158] shows the diffusion coefficients in the a- and c-directions calculated from Mössbauer diffusional line broadening data by using the lattice parameters (a=352 and c=571 pm), together with those measured by the tracer method[156]. The Mössbauer and the tracer data seem to be in good agreement at 953 K except for a composition of x=0.003, but the former at 773 K are larger than the latter for the samples with the composition of 0.08 and 0.125 of larger deviation from stoichiometry due to the correlation of successive jumps, based on the ordering of vacancies.

The difference of diffusion coefficients between the Mössbauer and the tracer data for a composition of x=0.003 (with very small concentration of defects) may be explained by considering the change of the predominant diffusion mechanism and a small correlation factor.

3. 3. 3. Iron in iron tellurides[160,161]

The tracer diffusion coefficients of iron and tellurium in iron tellurides have not been studied yet. The self-diffusion coefficients of iron in iron tellurides by the Mössbauer diffusional line broadening have been carried out only for δ'-phase ($Fe_{1.33}Te_2$) at 903 and 945 K[159], but those of iron in β- and ε-iron tellurides have not been reported.

The diffusion coefficients of iron in β-, δ'- and ε- iron tellurides were measured in the temperature range from 570 to 1023 K by the Mössbauer line broadening method[160,161]. Tracer technique was also used to measure the diffusion coefficients of iron in β-iron telluride[161]. The activation energies of the diffusion coefficient in β-iron telluride obtained by two kinds of techniques were 91.5 ± 5.4 and 105.6 ± 23 kJ · mol^{-1}, respectively, and were in good agreement within experimental error. The diffusion coefficients calculated by

Mössbauer experiment assuming random walk process were about four times larger than those obtained by the tracer method. If the jump probabilities of iron atoms depend on the direction of previous jump, the diffusion coefficients calculated from Mössbauer spectra become greater than those obtained by the tracer method, since the correlation factor in Eq. (22) is less than unity.

Figure 44[160] shows the full width at half maximum resonance of the spectra of iron tellurides against the reciprocal temperature. As seen in the figure, the diffusional line broadening was observed in the β and δ'-phases above 773 and 923 K, respectively, but not observed in the ε-phase even at 873 K near peritectic point.

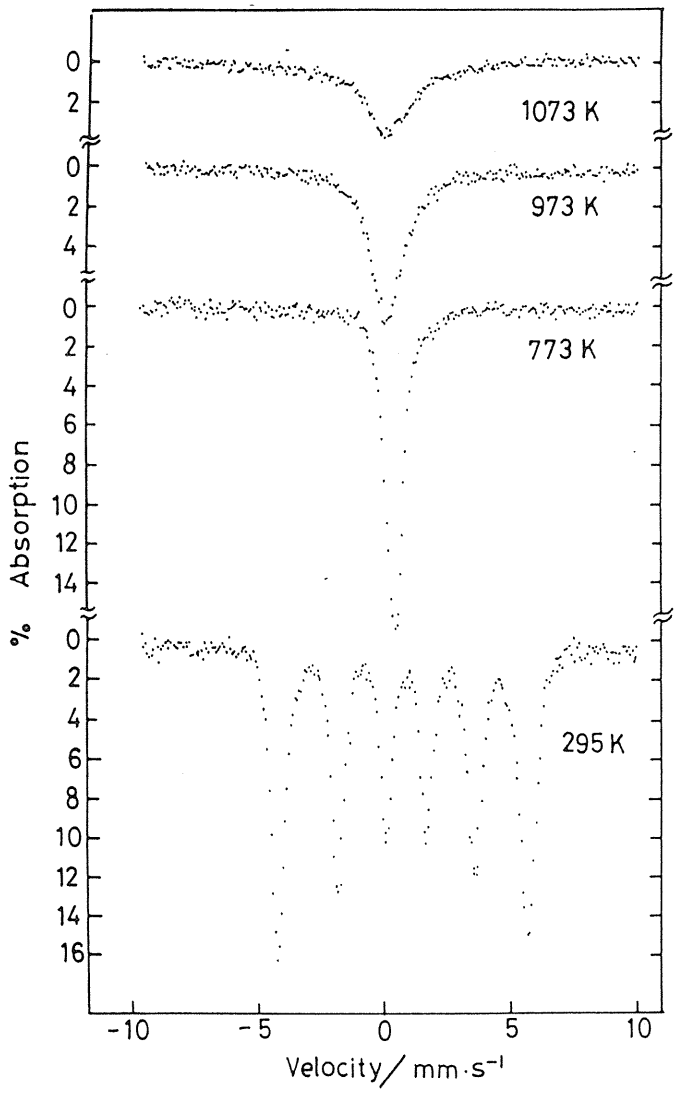

Fig. 41 Typical Mössbauer spectra of $Fe_{0.997}S$ sample in the temperature range from 295 to 1073 K[158].

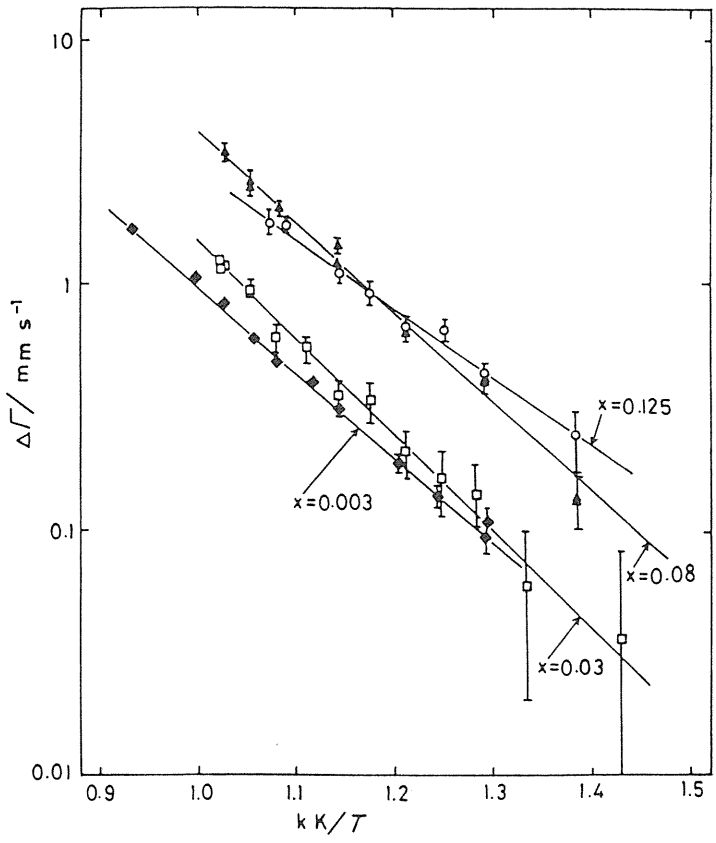

Fig. 42 Mössbauer diffusional line broadening, $\Delta\Gamma$, against $1/T$[158].

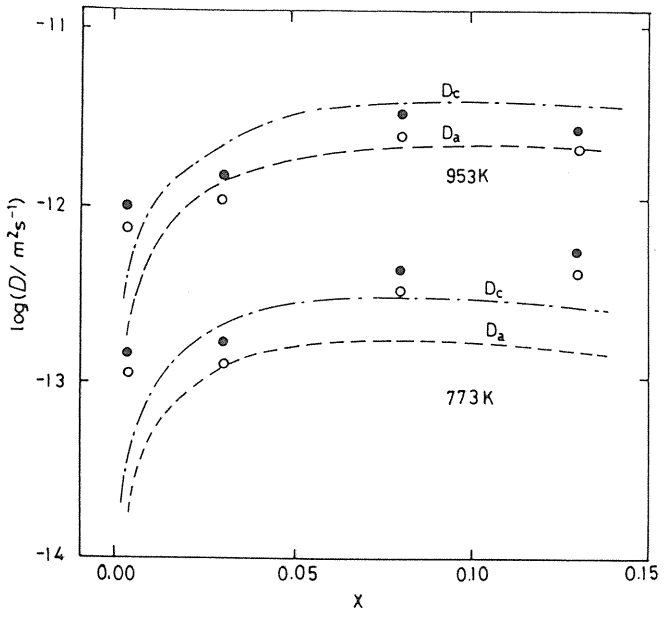

Fig. 43 Diffusion coefficients calculated from the diffusional line broadening and those measured by tracer technique against the composition (x) of $Fe_{1-x}S$ sample at 773 and 953 K:
(—·—·—) D_c by Condit et al.[156],
(-----) D_a by Condit et al.[156]
(●) D_c by the present authors[158],
(○) D_a by the present authors[158].

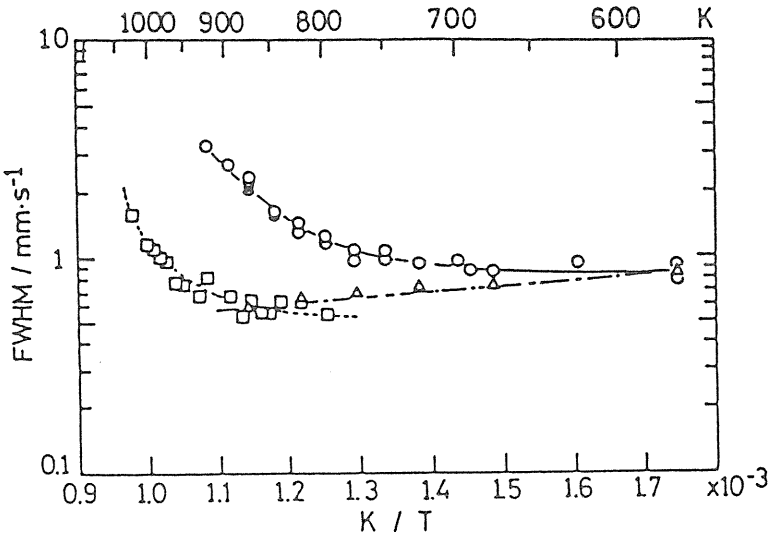

Fig. 44 The full width at half maximum resonance of the spectra of iron tellurides against the reciprocal temperature[160]. ○—○: β-phase ($Fe_{1.12}Te$), □—□: δ'-phase ($Fe_{1.33}Te_2$), △—·—△: ε-phase ($FeTe_{2.11}$).

3. 4. *Chemical diffusion*

3. 4. 1. *Oxygen in* $(Th, U)O_{2+x}$

Thorium-uranium mixed oxide, $(Th, U)O_2$ possesses promising qualities as a fuel for the thermal breeder reactors in the future. To understand the processes of oxidation and reduction of fuels through the chemical interaction with cladding materials and atmosphere and also to evaluate the redistribution of oxygen in the fuel pellets in reactor, the investigation of the diffusion of oxygen in the fuel pellet is important. However the diffusion coefficients of oxygen in $(Th_{1-y}U_y)O_{2+x}$ have not been determined so far until our measurements[162]. Most recently after our study, the chemical diffusion coefficients of $(Th_{1-y}U_y)O_{2+x}$ were measured in the low temperature range below 773 K by Furuya[163].

The present authors measured the chemical diffusion coefficients ($\tilde{D}$) in $(Th_{1-y}U_y)O_{2+x}$ (y=0.2 and 0.4) by means of thermogravimetry in the temperature

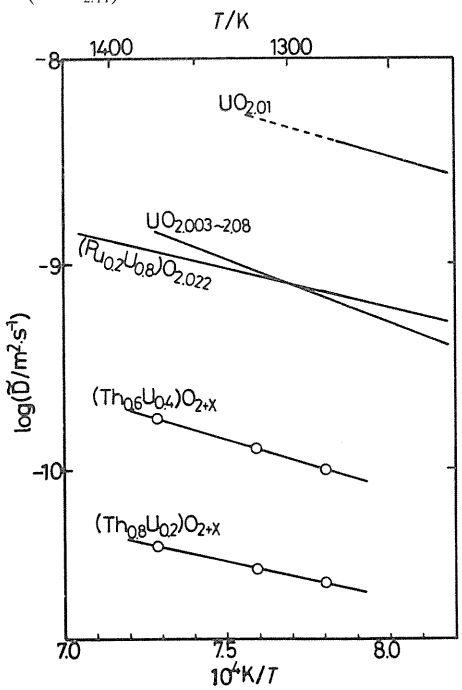

Fig. 45 Variation of the chemical diffusion coefficients of oxygen with the reciprocal temperatures[162]
o: $(Th_{1-y}U_y)O_{2+x}$ (y = 0.2 and 0.4) by Matsui and Naito[162], $UO_{2.003-2.08}$[165], $UO_{2.01}$[164], $(Pu_{0.2}U_{0.8})O_{2.022}$[166].

range $1282 \leqq T/K \leqq 1373$[162]. Since in binary or ternary actinide oxides MO_{2+x} (where $M=U$, Pu or $U+Pu$) with fluorite structure, the diffusion coefficient of oxygen is generally much higher than that of the cation, the chemical diffusion in $(Th_{1-y}U_y)O_{2+x}$ for oxidation and reduction is considered to be mainly controlled by the oxygen ion rather than the cation. The chemical diffusion coefficients of oxygen obtained by thermogravimetry are shown in Fig. 45 in comparison with those of UO_{2+x}[164,165] and $(Pu_{0.2}U_{0.8})O_{2+x}$[166]. From the chemical diffusion coefficient and the thermodynamic factor $(\partial \log Po_2/\partial \log x) = 12$ in the case of $(Th_{1-y}U_y)O_{2+x}$ ($x=0-0.016$)), the defect diffusion coefficients (D_d) were calculated and shown in Fig. 46[162], where the defect diffusion coefficients of UO_{2+x} estimated from the chemical diffusion coefficient[162,164] on the assumption of the value $(\partial \ln Po_2/\partial \ln x) = 12$ are included. It can be seen in these figures that the activation energies of $\tilde{D}$ or D_d are nearly the same, irrespective of the y value, and also nearly coincide with those of UO_{2+x} and $(Pu_{0.2}U_{0.8})O_{2+x}$ reported by other investigators, suggesting the presence of a similar diffusion mechanism to that found in UO_{2+x}. The magnitude of both diffusion coefficients $\tilde{D}$ and D_d of $(Th_{1-y}U_y)O_{2+x}$ increased with increasing uranium content and approached that of UO_{2+x}. The increase of D_d of $(Th_{1-y}U_y)O_{2+x}$ with y value was considered to be due to the increase of both the vibrational frequency of lattice and the entropy change of migration produced by the substitution of a U ion for a Th ion, since the activation energies are nearly equal, irrespective of the y value.

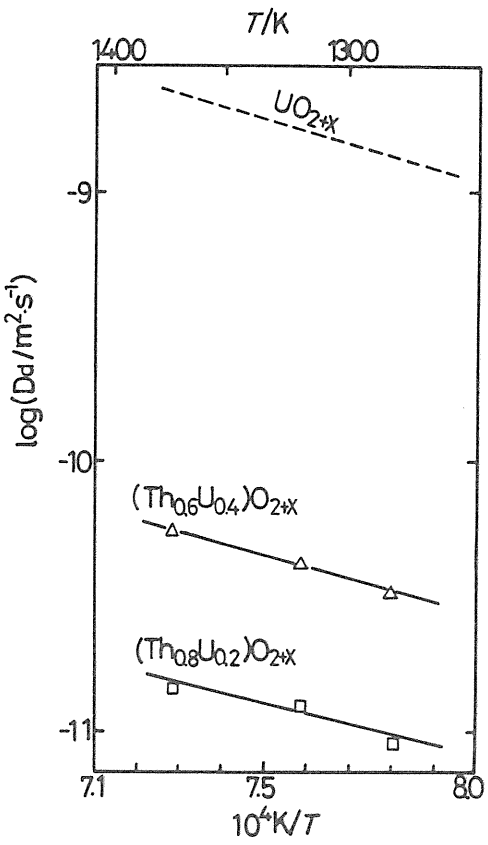

Fig. 46 Variation of the defect diffusion coefficients with the reciprocal temperatures[162].
—□— $(Th_{0.8}U_{0.2})O_{2+x}$[162],
—△— $(Th_{0.6}U_{0.4})O_{2+x}$[162]
– – UO_{2+x}[164]

3. 4. 2. *Niobium vacancy in* $Nb_{1-x}O_2$

The chemical diffusion coefficients in $Nb_{1-x}O_2$ were determined by the electrochemical potentiostatic technique with the use of a stabilized zirconia electrolyte[141,215]. Since the diffusion in NbO_2 was reported to occur by the niobium vacancy mechanism[141], the tracer- and self-diffusion coefficients of niobium were calculated for the chemical diffusion coefficients in terms of the thermodynamic factor $(\partial \ln Po_2/\partial \ln x) = 1$ and the correlation factor $f=0.721$. The chemical diffusion coefficients and the tracer diffusion coefficients in $Nb_{1-x}O_2$ are shown as a function of temperature in Figs. 47 and 48, respectively[162,164].

The chemical diffusion coefficients in NbO_2 obtained by thermogravimetry[168] and those

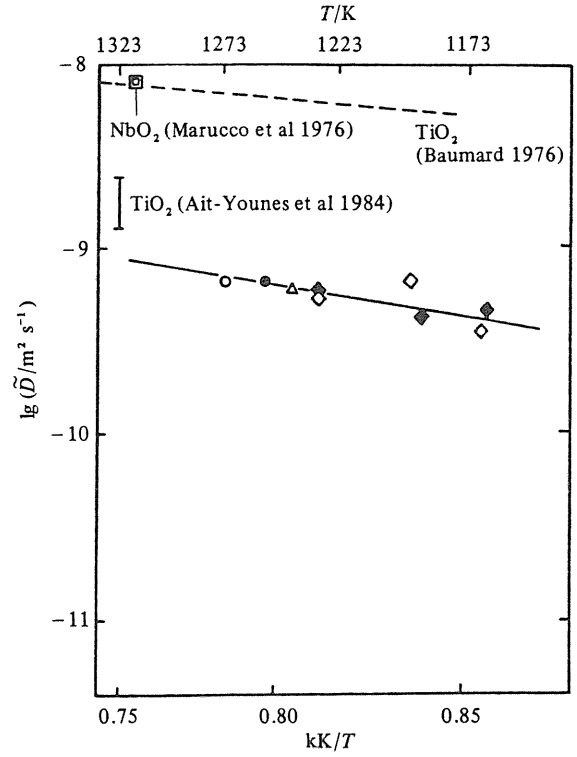

Fig. 47 Temperature dependence of the chemical diffusion coefficient for NbO_2[141] Open and closed symbols relate to data obtained from oxidation and reduction processes, respectively.[141,202] △ ($O/Nb = 2.0065$), ◆◇ (2.0004, 2.0009, 2.0011, 2.0012), ○● (2.0052, 2.0042)

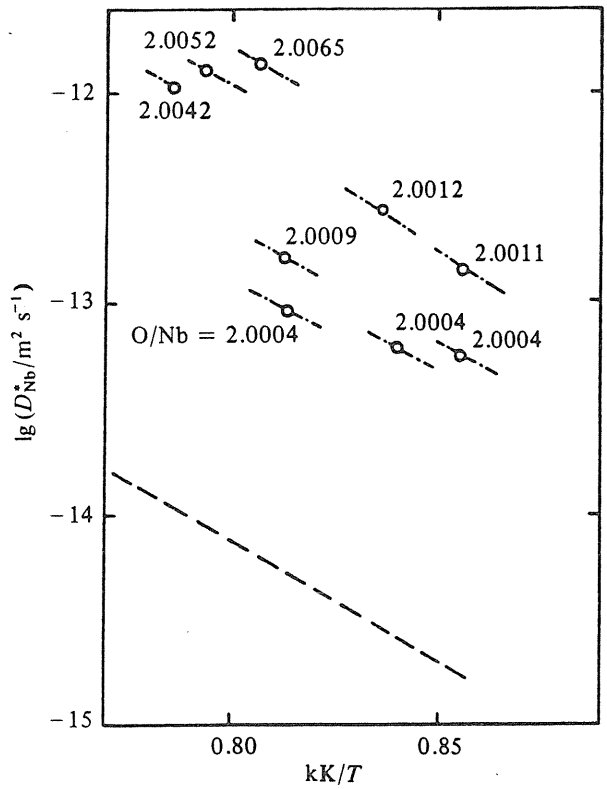

Fig. 48 Tracer diffusion coefficients calculated from chemical diffusion coefficients in NbO_2[141]. — — — Geld and Lyubimov with ^{95}Nb tracer[171] —○— Matsui et al.[141,202] from chemical diffusion coefficient

of TiO_2[169,170] with the same rutile structure as NbO_2 were also shown in Fig. 47. The temperature dependence of $\tilde{D}$ in NbO_2 determined by the authors[162,164] was seen to be similar to that in TiO_2 by Baumard[169] but the magnitude of the coefficient in NbO_2 at 1323 K was close to that in TiO_2 by Ait-Younes et al.[170]. The temperature dependence of the tracer diffusion coefficient determined with ^{95}Nb tracer by Geld and Lyubimov[171] is also shown in Fig. 48. The tracer diffusion coefficients calculated from $\tilde{D}$ are seen to increase with increasing compositional deviation from stoichiometric composition and are higher than those by Geld and Lyubimov probably due to the difference in nonstoichiometric composition.

3. 4. 3. Oxygen in $Ba_2YCu_3O_{7-x}$

The chemical diffusion coefficient of oxygen in $Ba_2YCu_3O_{7-x}$ was measured by thermogravimetry mainly in the region of the small oxygen deviation from stoichiometry ($x \leqq 0.4$) at low temperature ($T \leqq 873$ K)[109]. The dependences of the chemical diffusion coefficients of oxygen upon the oxygen nonstoichiometry x at constant temperature and upon the reciprocal temperature at constant oxygen nonstoichiometry x were first determined in the low temperature superconducting $Ba_2YCu_3O_{7-x}$ phase with the orthorhombic structure by the authors[109] and shown in Fig. 49. The compositional dependences of the chemical diffusion coefficients in $Ba_2YCu_3O_{7-x}$ at constant temperature changed at about x=0.35, indicating the occurrence of the phase transition, as was suggested from the slope change in the plot of log x vs. log Po_2 described in section 2.2.6.

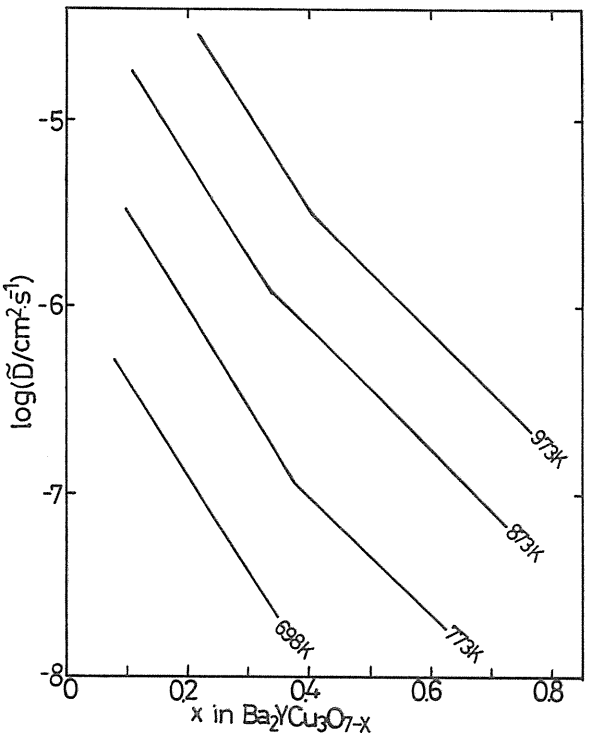

Fig. 49 Variation of the chemical diffusion coefficients of oxygen with the oxygen nonstoichiometry x in $Ba_2YCu_3O_{7-x}$[109].

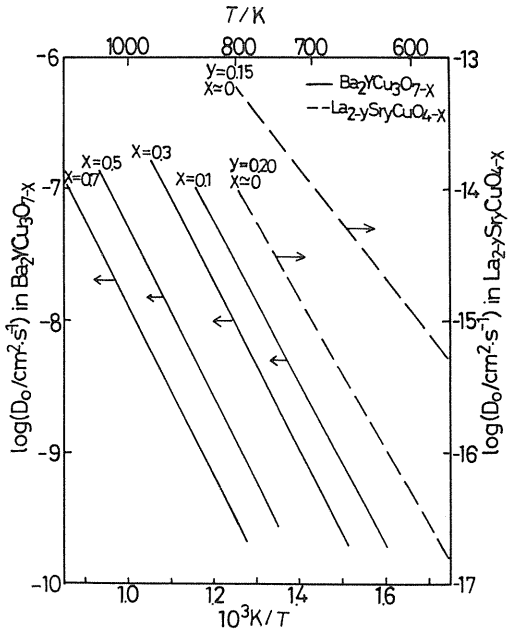

Fig. 50 Variation of the self-diffusion coefficient of oxygen in $Ba_2YCu_3O_{7-x}$ and $La_{2-y}Sr_yCuO_{4-x}$[172].

The diffusion coefficient of oxygen vacancy and the self-diffusion coefficient of oxygen in $Ba_2YCu_3O_{7-x}$ were first calculated from the chemical diffusion coefficients in terms of the thermodynamic factors 5 and 10 in the compositional region $x \leqq 0.3$ and $x \geqq 0.4$, respectively[109], whose values were also determined by the authors[109]. The self-diffusion coefficients are shown in Fig. 50[109] in comparison with those of another superconductor $La_{2-y}Sr_yCuO_{4-x}$[172]. The higher self-diffusion coefficient of oxygen in $Ba_2YCu_3O_{7-x}$ is thought to be due to the presence of the open path produced by a large number of oxygen vacancies in the crystal structure of $Ba_2YCu_3O_{7-x}$. The diffusion coefficient of oxygen vacancy in $Ba_2YCu_3O_{7-x}$ was nearly the same order as that of $La_{2-y}Sr_yCuO_{4-x}$ calculated from the self-diffusion coefficient of oxygen on the assumption of $x=1\times10^{-5}$ by the authors[109].

IV. Studies of chemical reactions

4. 1. Apparatus and method

Several chemical reactions have been investigated in our laboratory, including the oxidation reactions of uranium compounds, iron and iron-alloy, and noble metal alloys, and the reactions between iron and tellurium. The crystal growth from gaseous phase for several uranium and thorium oxides and zirconium carbides also have been studied by means of chemical transport reaction and chemical vapor deposition, respectively.

4. 1. 1. Apparatus used for the reactions

(a) Oxidation

The oxidation of some uranium compounds, iron and iron-alloys and noble metal alloys was carried out by using the apparatus as shown schematically in Fig. 1 of the chapter II. The oxidation rate was determined from the relation between the weight change of the sample and oxidation time.

(b) Reaction with tellurium

The reaction rates between iron and tellurium were measured by using the apparatus as shown in Fig. 51[173]. The silica capsule was placed in the electric furnace which had two controlled heating zones separately: the one for controlling the reaction temperature at iron

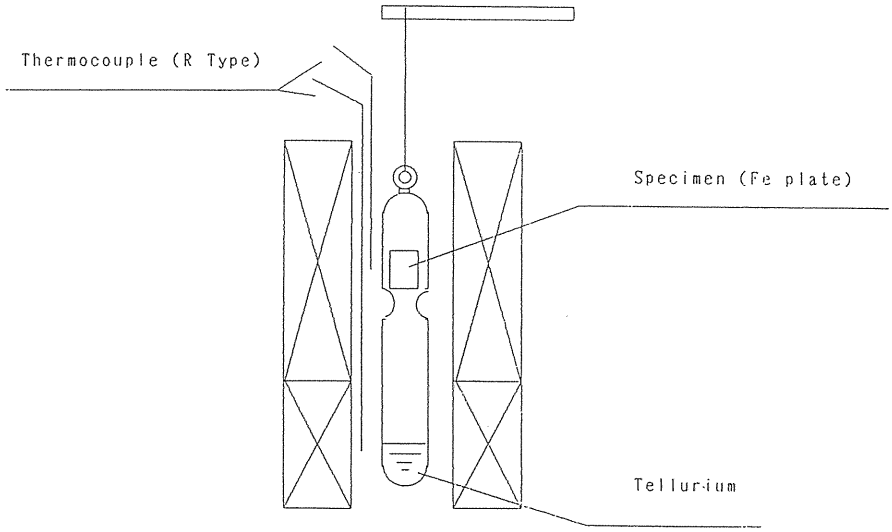

Fig. 51 Apparatus used for the reactions between iron and tellurium[173].

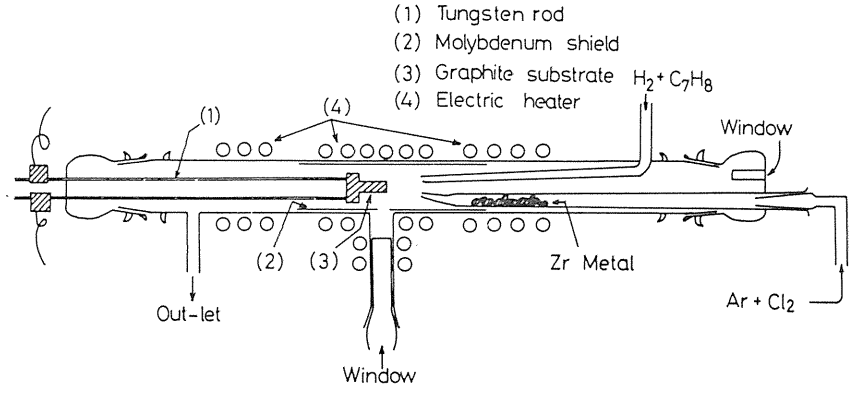

Fig. 52 Main part of the apparatus used for chemical vapor deposition of zirconium carbides[176].

specimen and the other for controlling the temperature of tellurium. The rate constants of the reaction were determined by measuring the weight gain of the iron specimen during the reaction period.

(c) Chemical transport reaction

Uranium and thorium oxides as the starting materials, and the transport reagents such as *HCl* and halogen gases were sealed in a quartz ampoule, and the ampoule was placed in a horizontal tubular resistance furnace with two independent heaters[174,175]. The single crystals were grown in a low temperature side under the temperature gradient.

(d) Chemical vapor deposition

The apparatus used for chemical vapor deposition of zirconium carbides is schematically shown in Fig. 52[176]. Zirconium chloride was produced by the reaction of zirconium metal sponge with chlorine gas which was carried into the reaction zone by a stream of argon gas. The partial pressure of toluene was varied by adjusting the temperature of the toluene saturator, and the toluence gas was carried with hydrogen gas.

The substrate was prepared from high purity graphite by shaping to a cylinder form and two tungsten electrodes were attached at the bottom of the substrate. Several turns of grooves were cut into the side of the graphite cylinder to improve the efficiency of direct heating. The temperature of the substrate was measured by an optical pyrometer through the window.

4. 1. 2. Apparatus for measuring the reaction rate

(a) Thermogravimetric Analysis

The gravimetric measurements were made with a Cahn RG automatic electromicrobalance. The sensitivity of the electrobalance was about 1 μg; at 1000°C there was about 30 μg of peak to peak noise, originating from gas turbulence. Reaction rate was calculated from the plots of weight gain as a function of time. In thermogravimetric analysis, the parabolic rate constant can be measured in the range from 10^{-11} to $10^{-2}\,kg^2m^{-4}s^{-1}$.

(b) Rutherford Backscattering Spectroscopy

In RBS a 1.5 MeV $^4He^+$ and a 1.0 MeV $^1H^+$ ion beams were impinged vertically on the specimen for thinner and thicker oxide films than 300 nm, respectively. The size of the ion beam spot on the specimen was about 1 mm in diameter. Ions backscattered at an angle of 160° were measured with a silicon surface barrier detector. The following equation[177] was used to calculate the thickness:

$$\triangle E = (K\varepsilon(E_0) + \varepsilon(KE_0)/|\cos\theta|)Nt, \tag{30}$$

where $\triangle E$ is the energy loss between incident and backscattered beams, K the kinematic factor, E_0 the incident beam energy, θ the scattering angle (=160°), t the thickness, $\varepsilon(E)$ the stopping cross section per atom at energy E and N the number of atoms per unit volume. For measuring the thickness of iron oxides film, the stopping cross sections of the oxides, magnetite and hematite, were estimated by applying the Bragg's rule of additivity with the stopping cross sections of iron and oxygen. Fig. 53[178] shows the typical Rutherford backscattering spectra when a 1.5 MeV $^4He^+$ beam was impinged on the oxide formed on iron after 6h in various oxygen partial pressures at 573 K. In RBS, the parabolic rate constant can be measured in the range from 10^{-16} to $10^{-10}\,kg^2m^{-4}s^{-1}$.

4. 2. Oxidation

4. 2. 1. Oxidation of UC

Uranium monocarbide is a nuclear fuel of great potential utility for its high melting point, high thermal conductivity, and dimensional stability under irradiation combined with

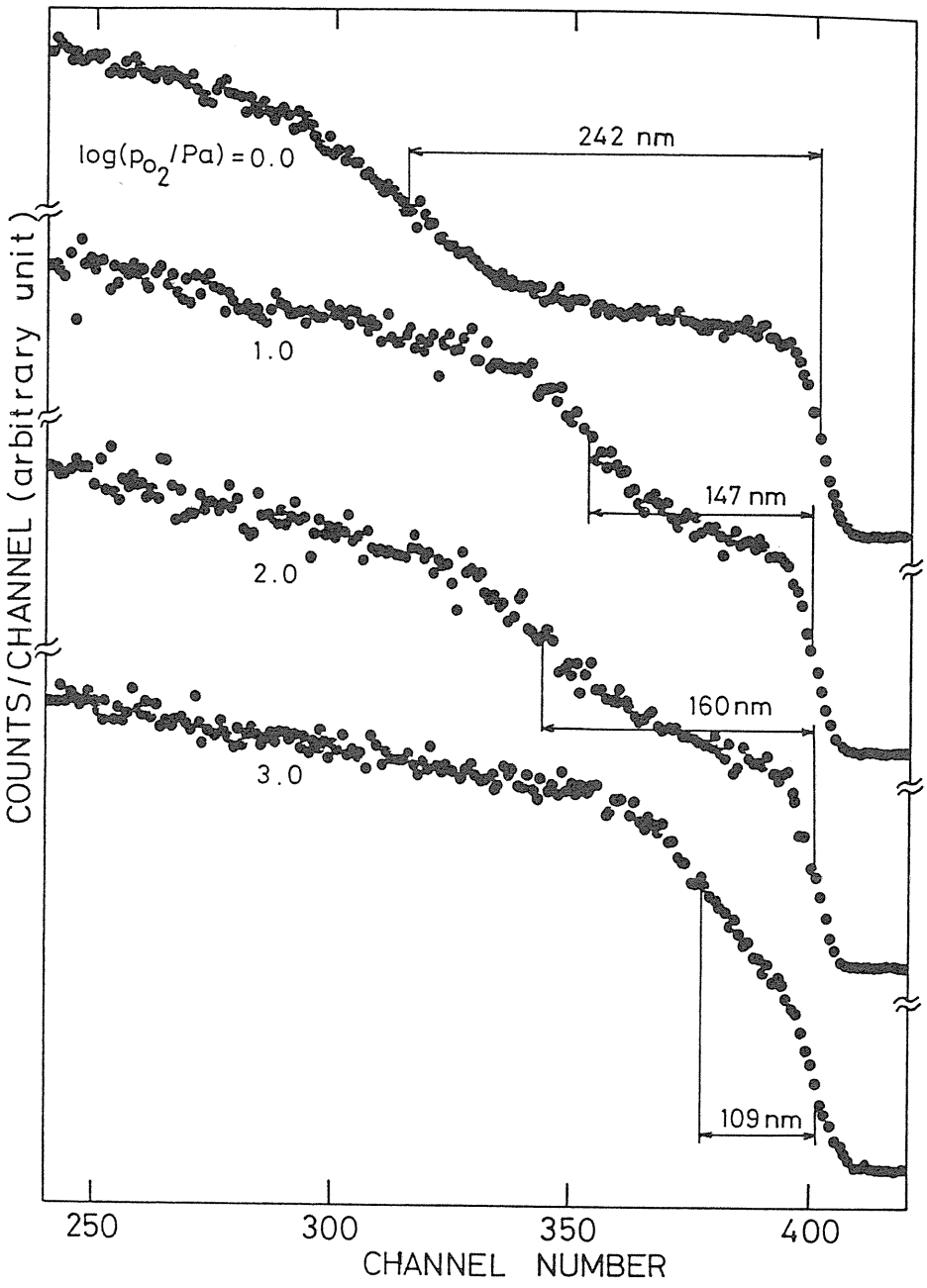

Fig. 53 The typical Rutherford backscattering spectra of oxides formed on iron after 6 h between 1 and 10^3 *Pa* at 573 K[178].

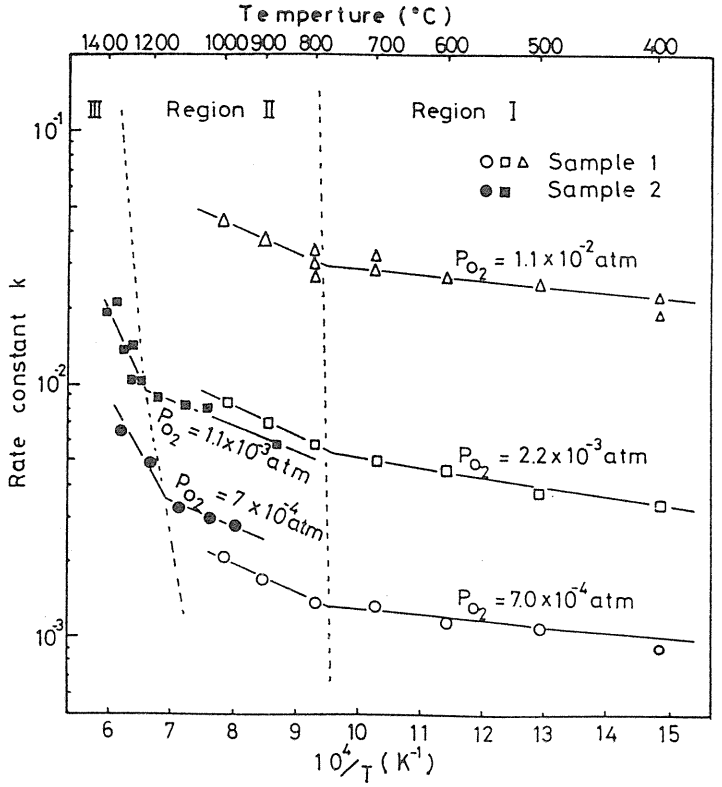

Fig. 54 Arrhenius plots representing isothermal oxidation of UC powder[179].

reasonably high uranium density. However, it reacts rapidly with the ambient atmosphere, particularly with oxygen, nitrogen and water vapor at elevated temperatures. The isothermal oxidation of powdered UC under controlled oxygen partial pressures was carried out by the authors[179] to obtain a better insight into the kinetics of the reaction.

Arrhenius plots are shown in Fig. 54[179], where it is seen that the common slopes separate the temperature range into three distinct regions at each oxygen partial pressure. The mean activation energies derived from these slopes are 6.7, 20.6 and 96.6 kJ/mol for regions I, II and III, respectively.

The relation between reaction rate constant and oxygen partial pressure is shown in Fig. 55[179] which reveals conformity with the relation K=const Po_2^n, with $n \simeq 1$ for the regions I and II, and about 1.6 for region III.

From the activation energy and the oxygen partial pressure dependence of the reaction rate constant, it is suggested that the rate-determining steps of the oxidation reaction for regions I, II and III are given in the following equations (31), (32) and (33), respectively

$$C + O_2 \rightarrow CO_2 \tag{31}$$

$$UC_{1-x}O_x + \{(2 + x' - x)/2\}O_2 \rightarrow UO_{2+x'} + (1 - x)C \tag{32}$$

$$UC_{1-x}O_x + \{(3 + x' - 2x)/2\}O_2 \rightarrow UO_{2+x'} + (1 - x)CO \tag{33}$$

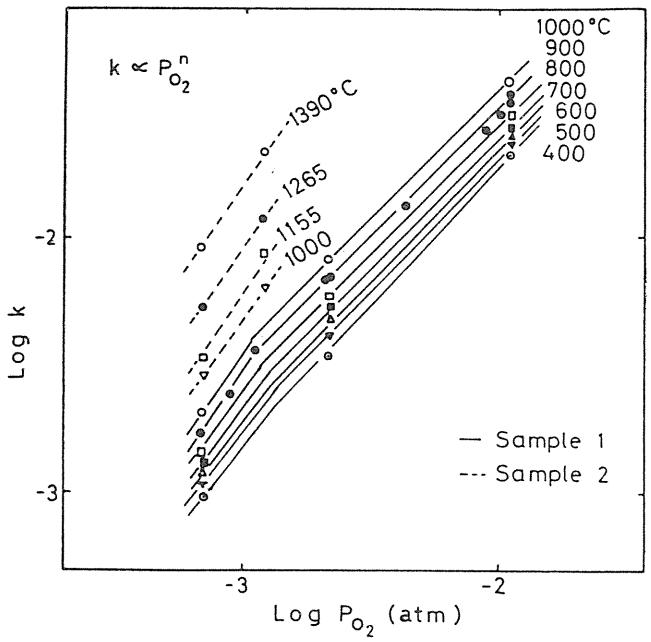

Fig. 55 Oxygen partial pressure dependence of reaction rate constant[179].

4. 2. 2. Oxidation of Iron

The radioactivity buildup in the primary coolant systems of water reactors has been increasing year by year, which is caused by the deposition of the corrosion products released from the iron base structural materials. Water as a coolant has such a low electrical conductivity that the growth of the oxide film as well as the metal dissolution play a major role as the corrosion process. From this point of view we made the study on the oxidation behavior of iron under various oxygen partial pressures around 573 K to clarify the effect of oxygen concentration on the corrosion of carbon steel in the coolant[178].

The thickness of the oxide film formed under various oxygen partial pressures at 573 K is plotted against square root of time in Fig. 56. It is seen from the figure that two-stage oxidation takes place. In the first stage the iron is oxidized very rapidly and then rather slowly in the second stage. The thickness of the oxide film in the first stage of oxidation reaches the maximum around 1 Pa. These results are consistent with those obtained at 543 K by Boggs et al[180]. It is seen from the Fig. 56 that the thickness at all oxygen partial pressures increases linearly with square root of time, which indicates that the oxidation obeys the parabolic rate law in the second stage.

The parabolic rate constant obtained from the slope in Fig. 56 is shown as a function of oxygen partial pressure in Fig. 57(a). Fig. 57(b) indicates the ratio of the magnetite peak area to the total oxide area for the specimen after 24h oxidation at each oxygen partial pressure by means of conversion electron Mössbauer spectroscopy (CEMS) and X-ray diffractometry. It is proposed from Figs. 57(a) and (b) that the mechanism of the oxidation is divided into the following four regions depending on the oxygen partial pressure. (I) 10^{-1} to $10^{-0.5}$ Pa: The growth of magnetite is dominant, and the parabolic rate constant is strongly dependent on oxygen partial pressure. (II) 1 to $10^{0.5}$ Pa: Hematite covers magnetite, but the presence of

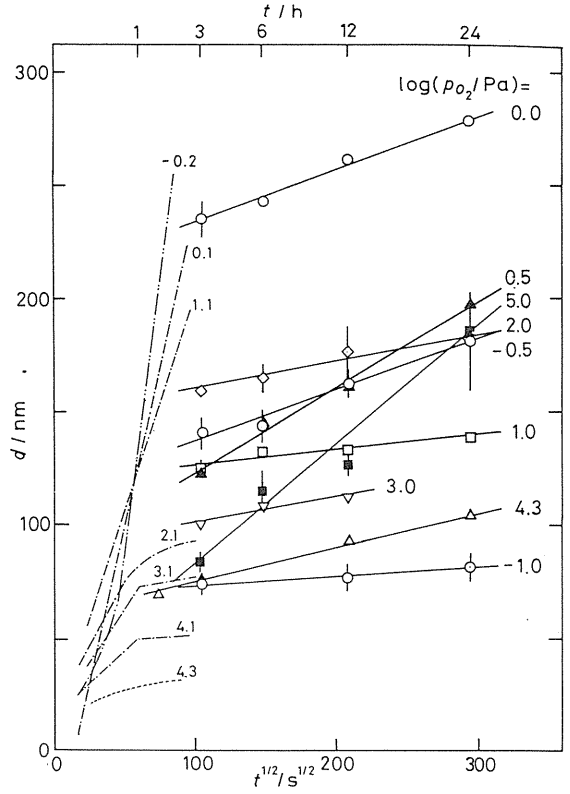

Fig. 56
Growth of oxide film on iron at various oxygen partial pressures at 573 K.
—·—·— Boggs et al.[180] at 543 K,
····· Gulbransen[181] at 573 K,
—··—··— Hussey et al.[182] at 573 K and
—— by the present authors[178] at 573 K.

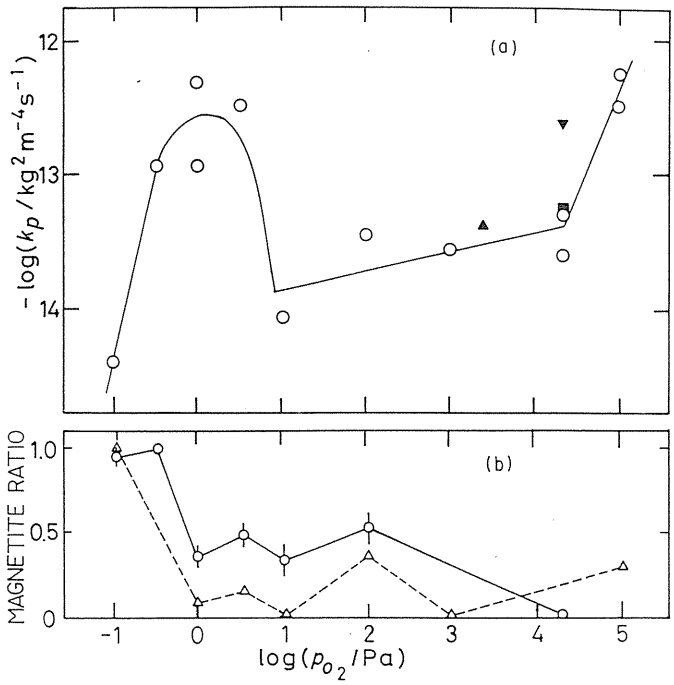

Fig. 57
(a) Parabolic rate constant vs. oxygen partial pressure at 573 K
(▲ Caule et al[183] at 569 K,
▼ Davies et al.[184] at 573 K,
■ Lustman[185] at 573 K and
present authors[178] at 573 K.
(b) Ratio of magnetite peak area to total oxide peak area of oxide formed after 24 h by CEMS ◇ and X-ray diffractometry △[178].

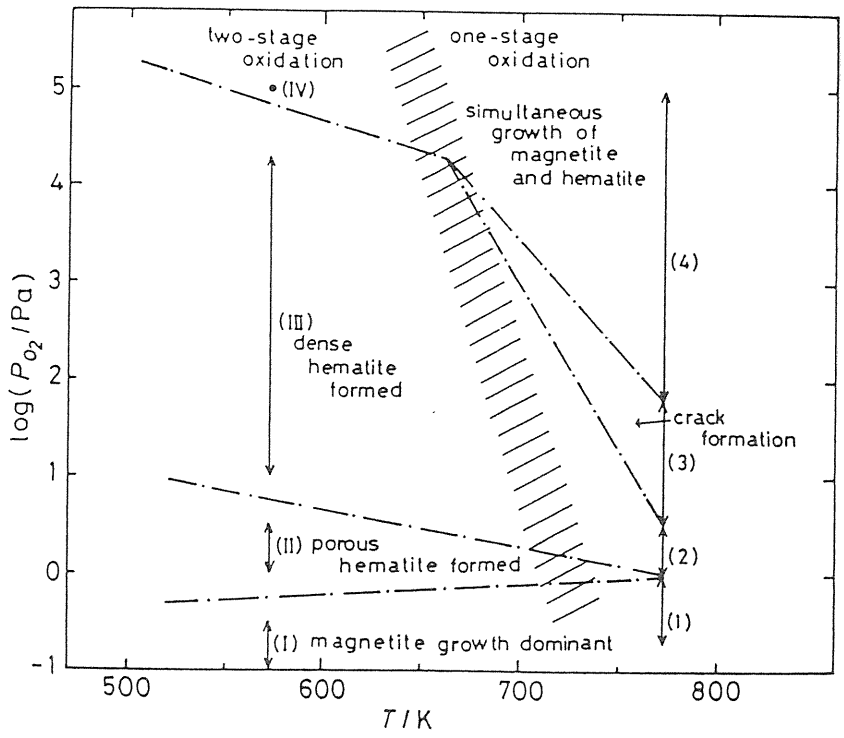

Fig. 58 Schematic representation of area where each oxidation mechanism holds[188].
—·—: Boundary where oxidation mechanism changes
/////: Boundary between one-stage and two-stage oxidations
↔: Range where identical oxidation mechanism holds at each temperature

grain boundaries enhanced the diffusion in oxide, keeping the parabolic rate constants to be high. (III) 10 to $10^{4.3}$ Pa: Hematite as a protective film covers magnetite uniformly so as to keep the parabolic rate constants low regardless of oxygen partial pressure. (IV) 10^{5} Pa: The sharp increase of the parabolic rate constant occurs due to the simultaneous growth of hematite and magnetite.

Fig. 58[178,186-188] shows the schematic representation of the region where each oxidation mechanism at 573 K described above holds, including the results at 773 K. As shown in the figure, the crack formation is observed between $10^{0.5}$ and $10^{1.8}$ Pa at 773 K, but is not found at 573 K.

The parabolic rate constants for the oxidation of iron under water vapor pressure of $10^{3.15}$ Pa at 573 K, together with those without water vapor are shown in Fig. 59(a)[189]. Fig. 59(b) indicates the ratio of magnetite peak area to the total oxide area for the specimen after 24h oxidation at each oxygen partial pressure without and with water vapor by means of CEMS or X-ray diffractometry. The remarkable enhanced oxidation of iron by water vapor was observed especially at the oxygen partial pressure of 10^{-1} Pa, where both magnetite and hematite were observed. On the other hand, for the cases without water vapor the oxide consisted mainly of magnetite in the oxygen partial pressure range of 10^{-1} to $10^{-0.5}$ Pa. It is also seen in Figs. 59(a) and (b) that the parabolic rate constant under water vapor decreases with

increasing oxygen partial pressure from 10^{-1} to $10^{4.3}$ Pa, where the ratio of magnetite to total oxides tends to decrease with increasing oxygen partial pressure. At 10^{5} Pa the parabolic rate constant under water vapor agreed with that without water vapor. The remarkable enhanced oxidation of iron by water vapor especially at the oxygen partial pressure of 10^{-1} Pa may be explained by vapor-phase diffusion of volatile $Fe(OH)_2$ from the metal-oxide interface to the outer layer crystals as proposed by Surman[190], although the solid state diffusion in oxide or through grain boundaries can make small contribution as another diffusion path[178]. The enhanced oxidation by water vapor becomes smaller when the oxygen partial pressure approaches water vapor pressure of $10^{3.15}$ Pa, and finally contribution by vapor-phase transport

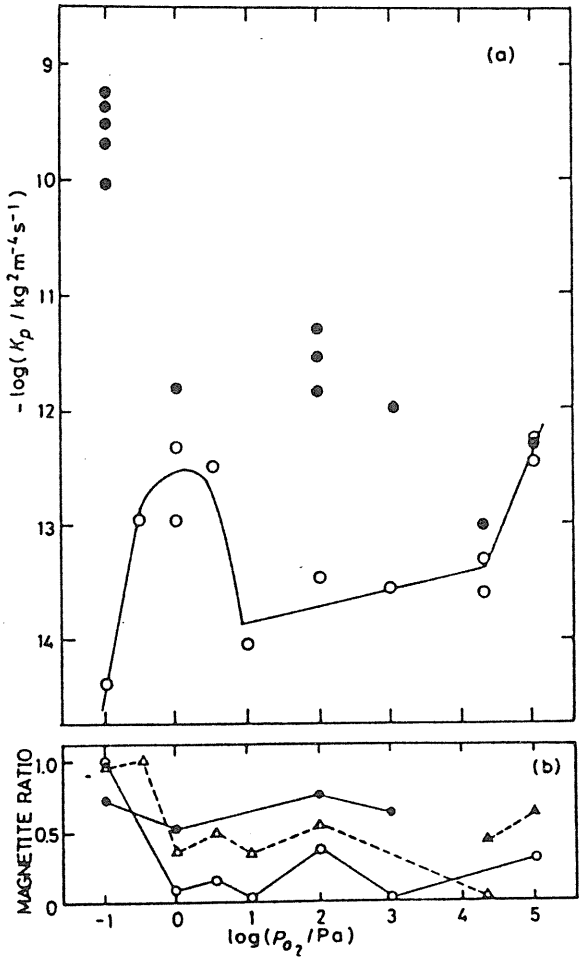

Fig. 59 (a) (above) Parabolic rate constant vs. oxygen partial pressure at 573 K.
○ without water vapor[178]
● with water vapor[189]
(b) (below) Ratio of magnetite peak area to total oxide peak area of oxide formed after 24 h by CEMS (△▲) and X-ray diffractometry (○●).
○△ without water vapor by the present authors[178]
●▲ with water vapor by the present authors[189]

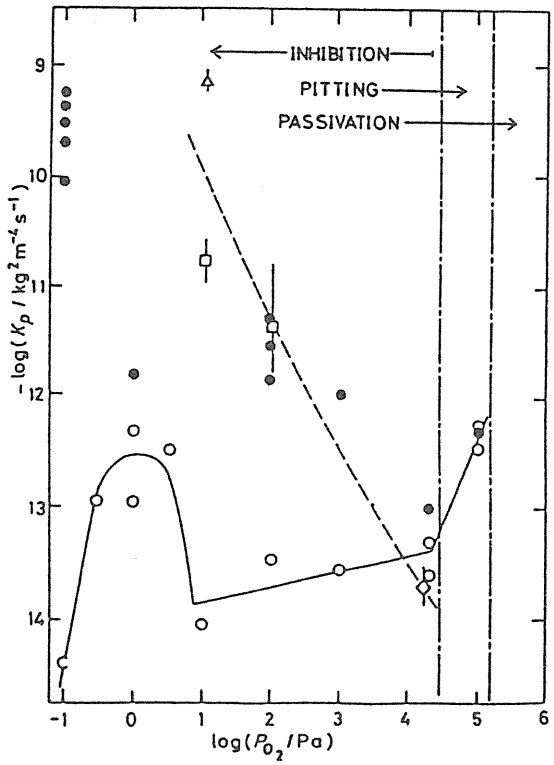

Fig. 60 Comparison between corrosion rate in water and parabolic rate constant in a gas phase without and with water vapor.
△ Tackett et al[193] at 573 K
□ Videm[192] at 588 K
◇ Vreeland et al.[194] at 558 K,
○ without water vapor by the present authors[178] at 573 K
● with water vapor by the present authors[179] at 573 K
----- corrosion rate in water[192-194]
—— parabolic rate constant in a gas phase without water vapor[178]

mechanism may equal to that by solid state diffusion mechanism. In the case of 10^5 Pa($>10^{3.15}$ Pa), solid state diffusion mechanism predominates and the parabolic rate constant with water vapor may be equal to that without water vapor.

The corrosion rate of iron in water can be compared with the oxidation rate in a gas, provided that the amount of metal lost due to the corrosion in water would be converted to the amount of the oxide to be gained. Considering that the oxygen in water is in equilibrium with the oxygen gas over water, the oxygen partial pressure equilibrated with the oxygen concentration in water is evaluated with Henry's constant at 573 K[191]. As a result 1, 10 and 100 ppb oxygen contents in water at 573 K correspond to about 1, 10 and 100 Pa oxygen partial pressure in gas phase, respectively[178]. The comparison of the parabolic rate constant with the corrosion rate in water is shown in Fig. 60. Videm[192] suggested that the corrosion behavior of carbon steel in water around 573 K was divided into three regions; 'inhibition', 'pitting' and 'passivation', depending on the oxygen concentration in water. Three regions for

the corrosion behavior of carbon steel are shown by the converted scale in Fig. 60. As seen in the figure, the corrosion rate in water is larger than the oxidation rate without water vapor in gas phase by about two orders of magnitude, but is closely related to the oxidation rate with water vapor in gas phase. The increase in gas phase oxidation at around 10^5 Pa just corresponds to the boundary between the 'inhibition' and the 'pitting' region in water corrosion. Judging from the condition of the formation of protective film in gas phase, it is suggested that the oxygen concentration in water should be controlled around 10 ppm (10^4 ppb), but in the present reactors the oxygen concentration is maintained to be 20 ~ 60 ppb by addition of oxygen gas into the coolant water.

Radioactivity buildup is caused maily by the deposition of crud on the structural materials. From this point of view, effect of particle size on Mössbauer parameters of α-Fe_2O_3 is studied by the present authors[195]. Both the isomer shift and quadrupole splitting slightly increase with decreasing average particle size, but internal magnetic field decreases due to decreasing relaxation time with decreasing particle size.

Chemical state of cobalt doped in and adsorbed on α-$(Fe_{1-x}Cr_x)_2O_3$ was measured by the present authors[196] using emission Mössbauer spectroscopy. Mössbauer parameters (internal magnetic field, quadrupole splitting and isomer shift) of both α-$(Fe_{1-x}Cr_x)_2O_3$ (x=0, 0.2 and ~ 1.0) doped and undoped with ^{57}Co are in good agreement at room temperature and 77 K, except internal magnetic fields of both α-Cr_2O_3 doped with ^{57}Co and enriched ^{57}Fe. It is thus concluded that ^{57}Fe produced from ^{57}Co occupies the octahedral sites as Fe^{3+} with small distortion from cubic symmetry. Different internal magnetic field of doped α-Cr_2O_3 may be explained by the difference of canting of the spin against the [lll] axis.

By adding zinc ions, the adsorption of Co^{2+} ions on α-Fe_2O_3 particles in aqueous solution is decreased considerably in the pH range of 6.5—9.5 at 303 K, but the internal magnetic field of ^{57}Co adsorbed on α-Fe_2O_3 does not change, although the internal magnetic fields of both samples with and without zinc ions are smaller than that of bulk α-Fe_2O_3 doped with ^{57}Co. This suggests that densities of ^{57}Co ions on the surface of α-Fe_2O_3 may be decreased by the addition of zinc ions and ^{57}Co ions adsorbed on α-Fe_2O_3 are weakly bound on the substrate.

4. 2. 3. Oxidation of fission-produced noble metal alloys

The fission-produced noble metals can be recognized as the important alternative resources to meet a part of the increasing need of noble metals. The recovery and separation of *Ru*, *Pd* and *Mo* from the simulated insoluble residue produced in dissolver solution of spent fuel were studied by various methods such as *Pb* extraction[200,201], dissolution in nitric acid solution[202] and oxidative vaporization[197,203] by the authors. The oxidation behaviors of noble metals and noble metal alloys are, therefore, of importance as a basic information for the oxidative vaporization.

The oxidation behaviors of the fine powders of *Mo*, *Ru*, *Rh*, *Pd* metals and $Mo_{0.45}Ru_{0.45}Pd_{0.10}$ alloy were studied by thermogravimetry, X-ray fluorescence analysis and X-ray diffractometry in the temperature range from 673 to 973 K in air[197]. The weight gain due to oxidation was observed with time for all samples at low temperatures below 773 K. The weight gains of *Mo*, *Ru* and the alloy were observed to be proportional to $t^{1/2}$ (t: time, parabolic law), and those of *Pd* and *Rh* were $t^{1/3}$ (cubic law) and t (linear law), respectively. The parabolic rate constants of *Mo*, the alloy and *Ru* obtained by the authors[197] are shown in Fig. 61[197] in comparison with previous results on *Mo*[198] and *Rh*[199]. The parabolic rate constants of *Mo*, the alloy and *Ru* are seen to be in decreasing order of magnitude. It was concluded from this figure by considering the results by X-ray fluorescence analysis and X-ray diffractometry that $Mo_{0.45}Ru_{0.45}Pd_{0.10}$ alloy was oxidized by the preferential oxidation of *Mo*

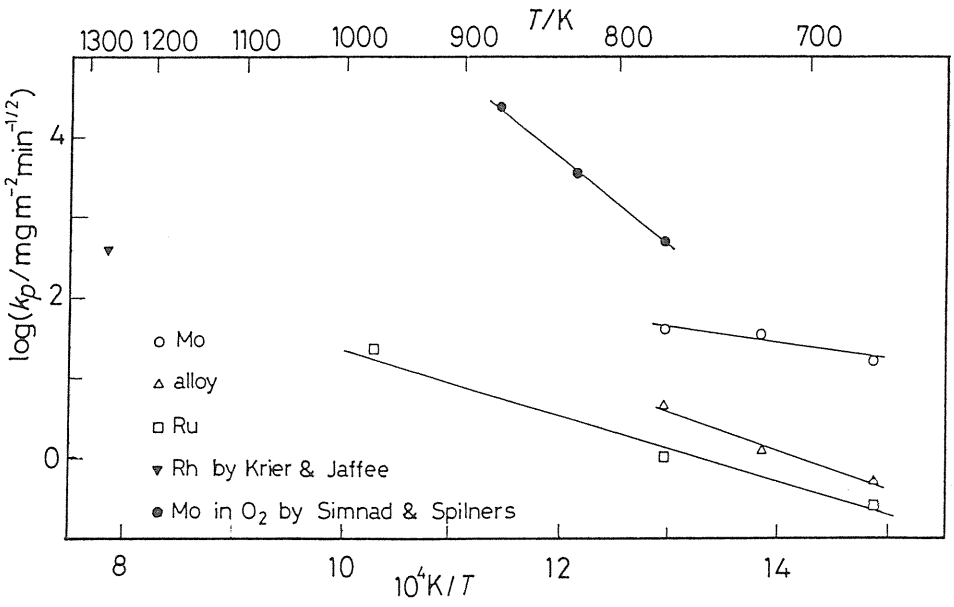

Fig. 61 Temperature dependence of the oxidation rate constants of *Mo*, *Ru* and the alloy ($M_{0.45}Ru_{0.45}Pd_{0.10}$) in air[197].

and *Ru* below 773 K. At 973 K, the weight loss due to oxidative vaporization was seen with time for *Mo*, *Pd* and the alloy. Two regions of the linear weight loss with time were observed in the case of the alloy. From the compositional change of the alloy, it was found that *Mo* and *Ru* were lost preferentially by the oxidative vaporization in both steps, although the vaporization rate of *Mo* was larger than *Ru*.

The oxygen partial pressures for the oxidation of the components, *Mo*, *Tc*, *Ru*, *Rh* and *Pd* in the alloys were calculated from the thermodynamic activity of *Pd* in the *Mo-Ru-Pd* alloys determined experimentally[120] and those of *Mo*, *Tc*, *Ru* and *Rh* in the alloys estimated on the basis of the regular solution model together with the data of the free energy of formation of oxides and are shown in Fig. 62[121], where those for pure metals *Mo*, *Tc*, *Ru*, *Rh* and *Pd* are also shown. As seen in Fig. 62, the magnitude of the oxygen partial pressures for the oxidation of *Pd*, *Rh*, *Ru*, *Tc* and *Mo* are in decreasing order of magnitude. Therefore, it may be said that the selective oxidation of the constituents of the alloys can be caused by selecting the adequate oxygen partial pressure at constant temperature and/or by selecting the adequate temperature at constant oxygen partial pressure[121].

4. 3. Reaction between iron base alloys and tellurium

Tellurium is a corrosive fission product and reacts with the inner surface of fast breeder reactor (FBR) fuel pins made of stainless steel.

It has been shown by the authors[173] that the tellurium uptake curves by iron obeyed the parabolic rate law and the platinum maker remained between the iron substrate and the reaction product in the marker experiments. These facts suggest that the reaction rates are governed by the diffusion of iron in iron tellurides. Fig. 63[173] shows the parabolic rate constants against the reciprocal temperature. The activation energy of the reaction between iron and

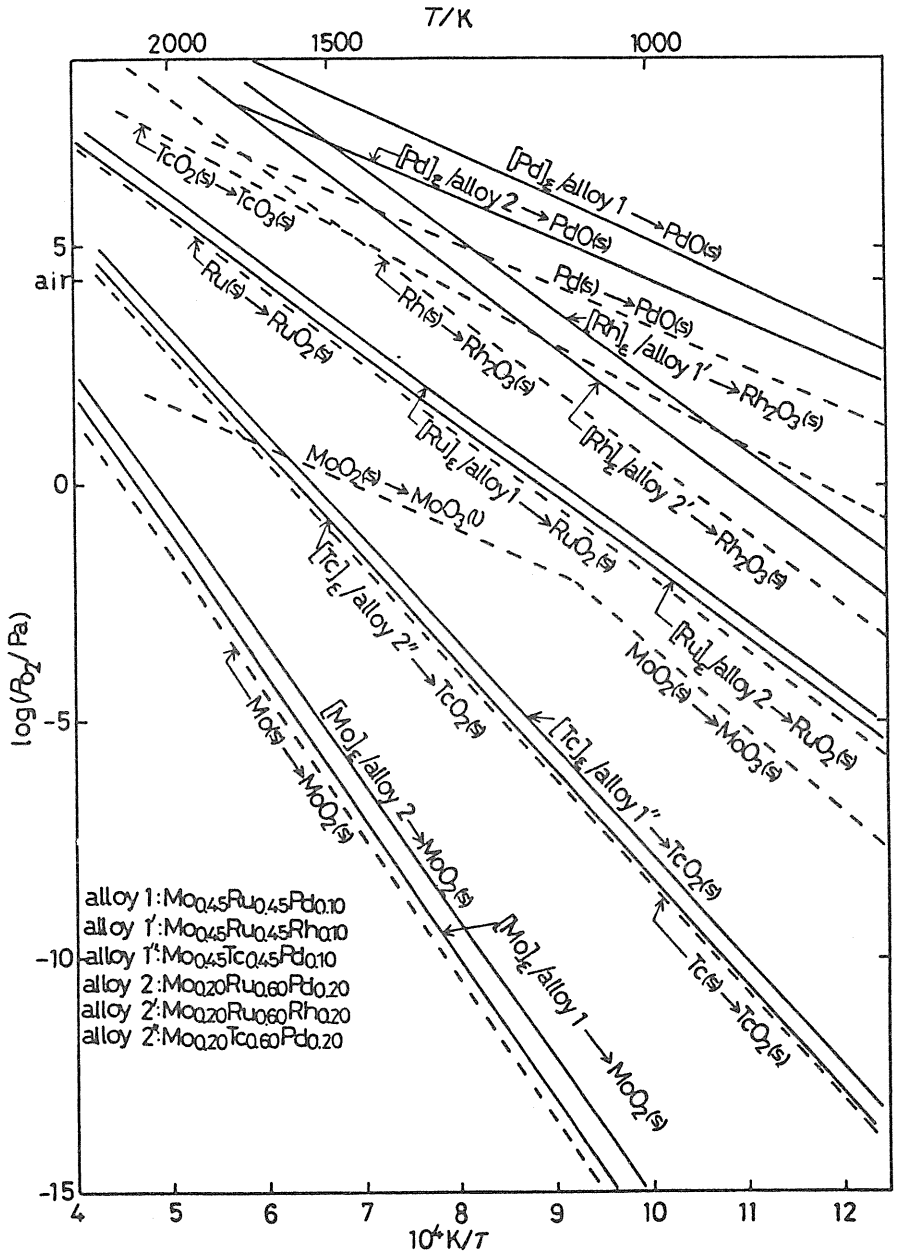

Fig. 62 Oxygen partial pressure for the oxidation of *Mo, Ru* and *Pd* in *Mo-Ru-Pd* alloys, *Rh* in *Mo-Ru-Rh* alloys and *Tc* in *Mo-Tc-Pd* alloys[121].

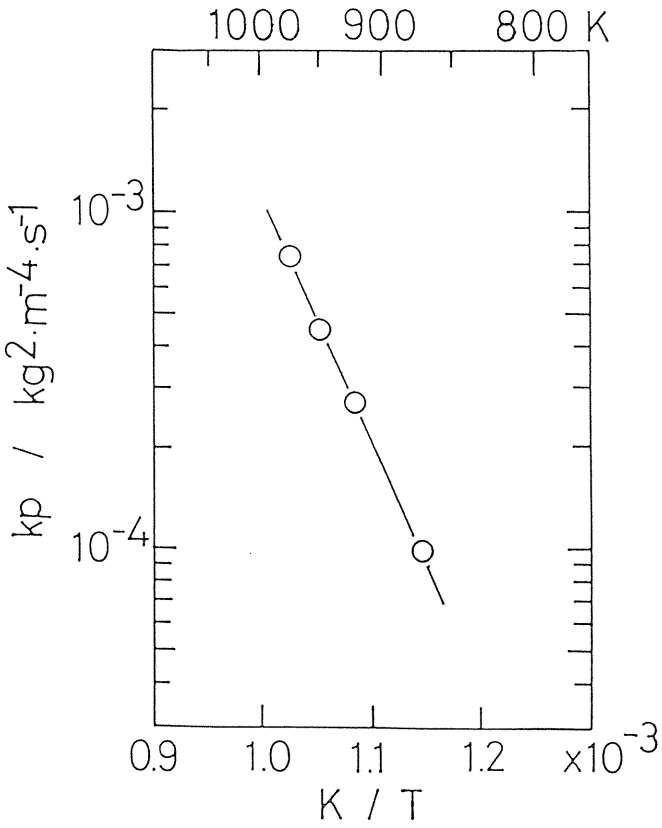

Fig. 63 Parabolic rate constants against the reciprocal temperature for the reaction between iron and tellurium[173].

tellurium was found to be 140 ± 3 kJ/mol, which was in good agreement with that of the diffusion of iron in δ'-iron telluride (161 ± 27 kJ/mol)[160]. The detection of δ'-iron telluride on the surface of specimen was attempted by X-ray diffractometry, but the diffraction pattern showed the presence of the mixture of β- and ε-iron tellurides alone as the telluride. According to the phase diagram[204], however, δ'-iron telluride decomposes to β- and ε-iron tellurides at 792 K, hence, it is considered that δ'-iron telluride formed on the iron is decomposed during the quench.

The reaction rates between iron-chromium (12 at% *Cr*) alloys and tellurium were measured by the authors[205] and it was found that they obeyed the parabolic rate law. The activation energies of the reaction of iron-chronium alloy (up to 12 at% *Cr*)at high temperatures above 930 K were in agreement with that of pure iron. It may be concluded that the rate determining step of the reaction between iron and tellurium is the same as that of the reaction of iron chromium alloys. However, the activation energy of iron-chromium alloy with the chromium content of 12 at% at low temperatures below 930 K is smaller than that at high temperatures above 930 K, probably due to grain boundary diffusion.

4. 4. *Crystal growth*

4. 4. 1. *Chemical transport reactions for UO_{2+x}, $U_{1-x}Th_xO_2$ and $ThSiO_4$*

Single crystals of various uranium oxides, $U_{1-x}Th_xO_2$ solid solution (x up to 0.69) and $ThSiO_4$ were prepared by chemical transport reactions using HCl and halogen gases as transporting agents in this laboratory[206-209].

When UO_2, U_4O_9 and U_3O_8 were transported with HCl gas, the O/U ratios of these oxides before and after transport were unchanged within 0.01 of O/U ratios. The transport rates of uranium oxides depend essentially on the composition of the solid phase as shown in Fig. 64. The transport rate increased about ten times with increase of O/U ratio from UO_2 to U_4O_9 and from U_4O_9 to U_3O_8. It is noted that the transport rates for the O/U ratio between 2.08 and 2.25 were approximately constant, while in the nonstoichiometric UO_{2+x} region the transport rate rapidly increased with increasing O/U ratio from stoichiometric UO_2 to hyperstoichiometric $UO_{2.08}$.

The identification of the gaseous species contributing to the transport reactions was attempted, and the samples rapidly quenched from the reaction temperature to liquid nitrogen temperature were analyzed by X-ray diffractometry[207]. As the results the existences of $UOCl_2$ in UO_2-HCl system and UO_2Cl_2 in U_4O_9-HCl and U_3O_8-HCl system were

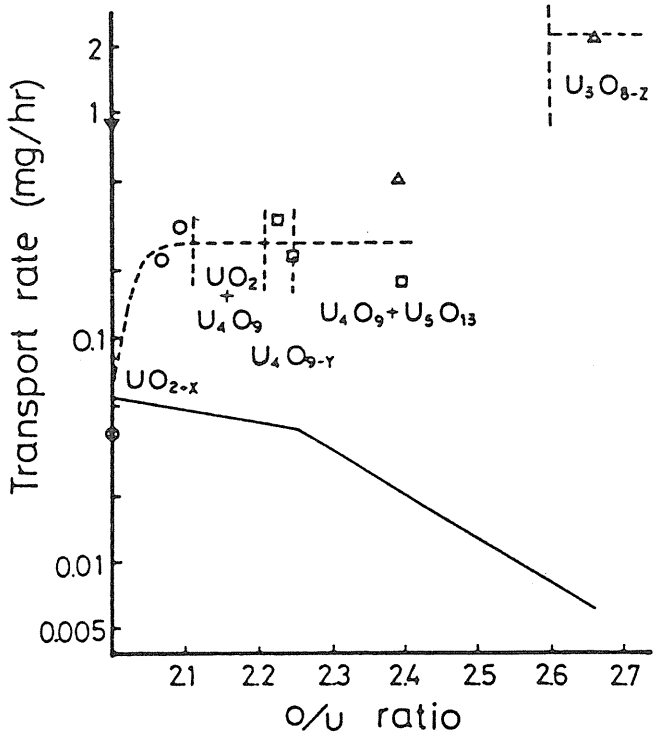

Fig. 64 Relationship between transport rate and O/U ratio of the crystals produced ($P_{HCl} = 3.5 \times 10^5$ *Pa* at 1198 K): (○) UO_2 phase ($0.2 \times 0.2 \times 0.2\,mm^3$); (□) U_4O_9 phase ($0.2 \times 0.2 \times 0.2\,mm^3$); (△) U_3O_8 phase ($1.0 \times 0.1 \times 0.1\,mm^3$), (▽) U-metal addition to UO_2 ($2.0 \times 0.1 \times 0.1\,mm^3$). Solid line shows the calculated rate, assuming only existence of chloride species and H_2O[207].

concluded, but the crystalline UCl_4 was never detected. It was concluded that $UOCl_2(g)$ is the major species in the UO_2-HCl system and the following reaction is to be considered as an essential one:

$$UO_2(s) + 2HCl(g) = UOCl_2(g) + H_2O(g). \tag{34}$$

Similary, UO_2Cl_2 is the major species which affects the transport of U_4O_9 or U_3O_8 with HCl. The following reactions can take place:

$$1/4\,U_4O_9(s) + 2HCl(g) = UO_2Cl_2(g) + 1/4\,H_2O(g) + 3/4\,H_2(g) \tag{35}$$

$$1/3\,U_3O_8(s) + 2HCl(g) = UO_2Cl_2(g) + 2/3\,H_2O(g) + 1/3\,H_2(g) \tag{36}$$

By using halogen gases as well as hydrogen chloride, UO_2 were also transported and the results are shown in Table 6. In the case of Cl_2 gas, the transport rate was very high, and the crystals produced were not UO_2, but U_4O_9 due to the oxidation of UO_2 with oxygen produced by the reaction of UO_2 with Cl_2 gas. Bromine gas was found to be very useful for transporting stoichiometric UO_2. Iodine gas was of less value for the transport of UO_2 and its rate was very low.

Table 6 Chemical transport of UO_2[206].

Transport agent	Pressure (atm at 925 °C)*	Transport time (hr)	Transport rate (mg/hr)	Crystals produced
HCl	1.0 – 3.7	470 – 205	0.014 – 0.038	prisms 0.2 mm^3
Cl_2	4.0	13	23.0	octahedra 2 mm^3
I_2	3.0	163	0.002	microscopic
Br_2	3.0	102	0.40	prisms 0.3 mm^3
Br_2+S_2	2.45+0.18	10	12.5	prisms 1 mm^3

* average temperature.

Single crystals of $U_{1-x}Th_xO_2$ solid solution were synthesized by closed-tube chemical transport using HCl gas as a transport agent[208]. The relations between the contents of the thorium in the source materials and those in the single crystals were shown in Fig. 65. Single crystals with higher content of thorium were produced by using the solid solution of UO_2 and ThO_2 as source material, and the maximum value of x was 0.69. It is also noted that the compositions of crystals produced move to the uranium-rich side with increasing thorium content in the source materials. As the content of ThO_2 increases, the partial pressure of $ThCl_4$ becomes high and thorium would be almost consumed to produce $ThSiO_4$ by the reaction with silica tube wall as follows:

$$ThCl_4(g) + SiO_2(s) \rightleftarrows ThO_2(s) + SiCl_4(g), \tag{37}$$

$$SiCl_4(g) + ThCl_4(g) + 4H_2O(g) \rightleftarrows ThSiO_4(s) + 8HCl(g) \tag{38}$$

When the thorium-content increases and the probable formation of $ThSiO_4$ is not negligible, some amount of $ThCl_4(g)$ would be consumed to form $ThSiO_4$ and the composition of single crystals of the solid solutions produced is expected to move to the uranium-rich side.

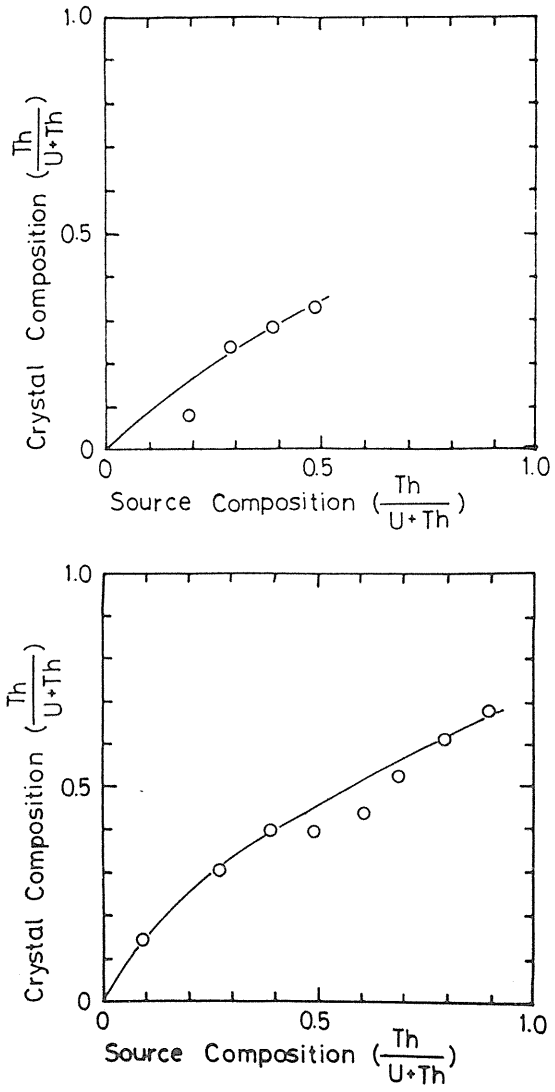

Fig. 65 Variation of crystal composition ($Th/Th+U$) with source composition ($Th/Th+U$):
(a) Source materials are mixtures.
(b) Source materials are solid solutions[208].

4. 4. 2. Chemical vapor deposition of ZrC

Nonstoichiometric zirconium carbide crystals with various composition were prepared by chemical vapor deposition (CVD)[210]. The gaseous mixture of zirconium tetrachloride and argon, and that of toluene and hydrogen were introduced to the reaction zone where a graphite substrate was heated between 1473 and 1673 K. The overall reaction is considered to proceed as

$$ZrCl_4(g) + (1/7)C_6H_5CH_3(g) + (10/7)H_2(g) = ZrC(s) + 4HCl(g) \quad (39)$$

The growth axis was determined as <110> direction by the Laue X-ray method. The whiskers produced have metallic color and their maximum length was 1.8 mm. The deposition rate did not appreciably related to the flow rate of hydrogen, but was proportional to the partial vapor pressures of the toluene gas. The relation between the lattice constants of the deposited crystals and the compositional ratio of carbon and zirconium in the gaseous phase (n_C/n_{Zr}) is shown in Fig. 66, together with the relation between the lattice constants and the composition value of C/Zr *in* ZrC_{1-x} reported by Storms and Griffin[211]. As seen from the figure, the lattice parameter of the crystal produced as a function of the composition ratio n_C/n_{Zr} in the gaseous mixture corresponds to that of the non-stoichiometric zirconium carbide as a function of the compositional ratio C/Zr in ZrC_{1-x}. It is noted that the composition of zirconium carbide whiskers produced by CVD can be changed corresponding to the gaseous composition.

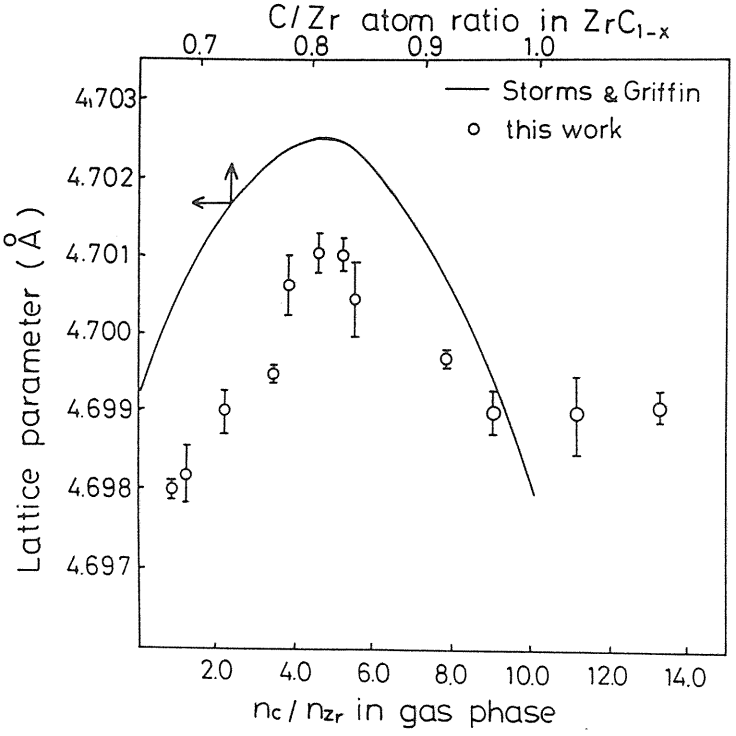

Fig. 66 Lattice constants of the deposited crystals versus compositional ratio of carbon to zirconium in the gaseous phase (n_C/n_{Zr})[210]. The upper curve shows the results of Storms and Griffin[211].

V. Calorimetric studies

5.1. *Heat capacity measurements*

Heat capacity measurements of nuclear reactor materials have been carried out by an adiabatic scanning calorimeter and a direct heating pulse calorimeter in our laboratory and the results in the period from 1968 to 1983 are described in the previous review[1] by the present authors. The studies on heat capacity measurements after the previous review are included in chapter II of this review. As written in chapter II an adiabatic scanning calorimeter was applied for refractory metal oxides of $(V_{1-y}Nb_y)O_{1\pm x}$[85], α-$(Ti_{1-y}V_y)O_x$ solid solution[94] and MoO_2 and MoO_3[98] and for spinel of $Cu_{1-x}Ni_xCr_2O_4$ ($x = 0.0 \sim 1.0$)[102] and for superconducting oxide $Ba_2YCu_3O_{7-x}$[212]. A direct heating pulse calorimeter is used to measure heat capacities of doped UO_{2+x} such as $U_{1-y}La_yO_2$ and $U_{1-y}Gd_yO_2$ (y=0.044 ~ 0.142 mol%)[26,28] and those of metallic fuels $U_{0.80}Zr_{0.20}$ and $U_{0.80}Mo_{0.20}$[111].

5. 2. *Vapor pressure measurements*

The loss of matter owing to vaporization reactions may be the most severe limiting factor in the use of nuclear materials as the nuclear fuels for the nuclear fission reactor and also in the use of the materials as the first wall for the nuclear fusion reactor. In addition to providing the vapor pressure data necessary for the calculation of vaporization loss, the study of vaporization process gives the free energy and enthalpy differences between the products and reactants, from which the nature of high temperature reactions, the energies of chemical bonding in gaseous species, the thermodynamic properties of solids and liquids concerned and phase relation at high temperatures can be determined.

In this section, vaporization studies performed after publishing the previous articles[1] in this memoirs of the Faculty of Engineering are briefly summarized.

Vapor pressure measurements on the various vanadium oxides (*V-O* solid solution, VO, V_2O_3 and their mixtures) in the vanadium-oxygen system were performed by mass spectrometric method in the temperature range 1703-2117 K[86-88] and thermodynamic quantities such as enthalpies of formation for $V(g)$, $VO(g)$ and $VO_2(g)$, dissociation energies of $VO(g)$ and $VO_2(g)$, the partial molar enthalpies and entropies of oxygen in various phases were obtained. Besides thermodynamic quantities, the phase boundaries and the defect structures were also discussed as was described in section II.

Vapor pressure measurements on the $Mo_xRu_yPd_z$ alloys (x=0.20–0.45, y=0.15–0.60, z=0.20–0.40) were measured by mass-spectrometric method in the temperature range 1536-1791 K[119,120]. Palladium vapor was observed as the only gaseous species. The chemical activities of *Pd* in the alloys determined from the vapor pressures of $Pd(g)$ were in good agreement with those calculated on the basis of the regular solution model. Thermodynamic quantities such as the partial molar free energy of mixing, the excess partial molar free energy of palladium and the partial molar enthalpy and entropy of $Pd(g)$ over *Mo-Ru-Pd* alloys were also calculated from the palladium vapor pressures. The vapor pressures over pure metals (*Mo, Tc, Rh, Pd* and *Ru*) and those over several alloys (*Mo-Ru-Pd, Mo-Ru-Rh* and *Mo-Tc-Pd*) were calculated as a function of temperature based on the regular solution model together with the experimental data[121]. The equlibrium oxygen partial pressures for the oxidation of pure metals and alloys were calculated in the same way. The vapor pressures of the gaseous species during oxidative vaporization of the metals and alloys were also estimated as a function of oxygen partial pressure[121].

Vapor pressures of palladium over the *Pd-Zr* solid solution ($Pd(ss)$), and over the two-phase mixtures of $Pd(ss) + Pd_3Zr$ and $Pd_3Zr + Pd_2Zr$ in the *Pd-Zr* system were measured by mass spectrometric method[127]. The free energy of formation of $Pd(ss)$ was obtained by

Gibbs-Duhem integration of the palladium activity. The enthalpies of formation of the intermetallic compounds *Pd_3Zr and Pd_2Zr were also obtained*[127].

Acknowledgment

The authors would like to express our sincere gratitude to the colleagues and the students who collaborated with us in each original work. This review is a sort of summary of these works carried out in our laboratory during the past many years. We are also very indebted to many secretaries for preparing the manuscripts of many papers cited in this review. We wish to express our deep appreciation to them.

References

1) K. Naito, H. Inaba and T. Matsui, Memoirs of Fac. of Eng., Nagoya University **Vol.35**, (No. 1) p.36(1983).
2) K. Naito, T. Tsuji and S. Watanabe, Solid State Ionics **1**, 509 (1980).
3) K. Naito, T. Tsuji and Y. Asakura, J. Nucl. Sci. Tech. **12**, 314 (1975).
4) T. Tsuji, Netsu Sokutei **17**, 41 (1990).
5) K. Naito and T. Tsuji, Kagaku Kogyo **54**, 518 (1976).
6) K. Naito, T. Tsuji, S. Watanabe and H. Sakai, Solid State Ionics **3/4**, 635 (1981).
7) T. Ishii, K. Naito and K. Oshima, J. Nucl. Mater. **35**, 335 (1970).
8) K. Naito, H. Inaba, M. Ishida, Y. Saito and H. Arima, J. Phys. E. Sci. Instrum. **7**, 464 (1974).
9) T. Matsui and K. Naito, J. Solid State Chem. **59**, 228 (1985).
10) K. Naito and N. Kamegashira, Adv. in Nucl. Sci and Technol. **9**, 99 (1976).
11) K. Naito, Ceramics **16**, 881 (1981).
12) K. Naito, T. Tsuji and T. Matsui, in: Non-Stoichiometric Compounds Surface, Grain Boundaries and Structural Defects, J. Nowotny, W. Weppner (Eds), Kluwer Academic Pub., The Netherlands, p.27 (1989).
13) K. Naito, T. Tsuji and T. Matsui, J. Radioanal Nucl. Chem. to be published (1990).
14) T. Matsui and K. Naito, J. Nucl. Mater. **138**, 19 (1986).
15) K. Une and M. Oguma, J. Nucl. Mater. **131**, 88(1985); **110**, 215 (1982).
16) T. Fujino, J. Tateno and H. Tagawa, J. Solid State Chem. **24**, 11 (1978).
17) T. Matsui and K. Naito, J. Nucl. Mater. **136**, 59 (1985).
18) T. Matsui and K. Naito, J. Nucl. Mater. **137**, 212 (1986).
19) S. Aronson and J.C. Clayton, J. Chem. Phys. **32**, 749 (1960).
20) S. Aronson and J.C. Clayton, J. Chem. Phys. **35**, 1055 (1961).
21) T.L. Markin, E.J. McIver, Plutonium 1965 and Other Actinides p.845 (1965).
22) T. Tsuji, T. Matsui, M. Abe and K. Naito, J. Nucl. Mater. **168**, 151 (1989).
23) T. Matsui and K. Naito, J. Less. Common. Met. **121**, 279 (1986).
24) F.A. Kröger, H.J. Vink, in: Solid State Physics, vol. 3, F. Seitz, D. Turnbull (Eds), Academic Press, New York, p.588 (1956).
25) K. Naito, J. Nucl. Mater. **167**, 30 (1989).
26) H. Inaba, K. Naito, M. Oguma and H. Masuda, J. Nucl. Mater. **137**, 176 (1986).
27) H. Inaba, K. Naito and M. Oguma, J. Nucl. Mater. **149**, 341 (1987).
28) T. Matsui, Y. Arita and K. Naito, J. Radioanal. and Nucl. Chem. **143**, 221 (1990).
29) T. Matsui and K. Naito, J. Nucl. Mater. **151**, 66 (1987).
30) K. Naito, J. Nucl. Mater. **51**, 126 (1974).
31) H. Inaba and K. Naito, J. Nucl. Mater. **49**, 181 (1973).

32) K. Seta, T. Matsui, H. Inaba and K. Naito, J. Nucl. Mater. **110**, 47 (1982).
33) K. Naito, T. Ishii, Y. Hamaguchi and K. Oshima, Solid State Commun. **5**, 349 (1967).
34) K. Naito, T. Tsuji and T. Matsui, J. Nucl. Mater. **48**, 58 (1973).
35) H. Blank and C. Ronchi, Acta Cryst. **A24**, 657 (1968).
36) F. Grønvold, N.J. Kveseth, A. Sveen and J. Trichy, J. Chem. Thermodyn, **2**, 665(1970).
37) J. Tateno, J. Phys. Chem. Solids **30**, 1321 (1969).
38) W.A. Young, L.L. Lynds, J.S. Mohl and G. G. Libowitz, NAA-SR-6765 (1962).
39) B.T.M. Willis, J. de Phys. **25**, 43 (1964).
40) T. Ishii, K. Naito, K. Oshima and Y. Hamaguchi, J. Phys. Chem. Solids **32**, 235 (1971).
41) T. Matsui and K. Naito, J. Nucl. Sci. Tech. **12**, 250 (1975).
42) T. Matsui, T. Tsuji and K. Naito, J. Nucl. Sci. Technol. **11**, 317 (1974).
43) T. Matsui, T. Tsuji and K. Naito, J. Nucl. Sci. Technol. **11**, 216 (1974).
44) K. Naito, T. Tsuji and F. Ohya, J. Nucl. Mater. **114**, 136 (1983).
45) R. Sato, H. Doi, B. Ishii and H. Uchikoshi, Acta Cryst. **14**, 763 (1961).
46) K. Naito, T. Tsuji, K. Ouchi, T. Yahata, T. Yamashita and H. Tagawa, J. Nucl. Mater. **95**, 181 (1980).
47) K. Naito, T. Tsuji, T. Fujino and T. Yamashita, J. Nucl. Mater. **169**, 329 (1989).
48) L.M. Atlas and G.J. Schlehman, in: Thermodynamics, vol. II (IAEA, Vienna, 1966) p.407.
49) P. Chereau and J.F. Wadier, J. Nucl. Mater. **35**, 335 (1975).
50) L.M. Atlas, G.J. Schlehman and D.W. Readey, J. Am. Ceram. Soc. **49**, 624 (1966).
51) T. Matsui and K. Naito, J. Nucl. Mater. **132**, 212 (1985).
52) S. Aronson and J. C. Clayton, J. Chem. Phys. **32**, 749 (1960).
53) G. N. Schwaba and F. Bohla, Z. Naturforsch **A14**, 71 (1959).
54) G. U. S. Rao, S. Damdes, R. N. Mehvotra and C. N. R. Rao, J. Solid State Chem. **2**, 377 (1970).
55) N. M. Tallan and R. W. Vest, J. Amer. Ceram. Soc. **49**, 401 (1966).
56) K. Naito, T. Tsuji and K. Une, J. Solid State Chem. **10**, 109 (1974).
57) H. Inaba and K. Naito, J. Solid State Chem. **50**, 111 (1983).
58) H. Inaba and K. Naito, J. Solid State Chem. **50**, 100 (1983).
59) K. Naito, N. Kamegashira and N. Sasaki, US-Japan Joint Seminar on Defects and Diffusion in Solids, Tokyo, Japan (1976).
60) K. Naito and T. Matsui, Solid State Ionics **12**, 1125 (1984).
61) K. Naito, N. Kamegashira and N. Sasaki, J. Solid State Chem. **35**, 305 (1980).
62) T. Matsui and K. Naito, J. Sollid State Chem. **59**, 228 (1985).
63) N. Kamegashira, T. Matsui, M. Harada and K. Naito, J. Nucl. Mater **101**, 207 (1981).
64) T. Matsui and K. Naito, J. Nucl. Mater. **102**, 227 (1981).
65) T. Matsui and K. Naito, Intern. J. Mass Spectr. and Ion Phys. **47**, 253 (1983).
66) T. Matsui and K. Naito, J. Nucl. Mater. **107**, 83 (1982).
67) T. Matsui and K. Naito, J. Nucl. Mater. **115**, 178 (1983).
68) J. M. Wimmer and W. C. Tripp, Aerospace Research Laboratories Report 73-0157 (1973).
69) R. N. Blumenthal, J. B. Moser and D. H. Whitmore, J. Amer, Ceram. Soc. **48**, 617 (1965).
70) P. Kofstad and P. B. Anderson, J. Phys. Chem. Solids **21**, 280 (1961).
71) P. Kofstad, J. Less-Common Met. **14**, 153 (1968).
72) K. Seta and K. Naito, J. Chem. Thermodyn. **14**, 921 (1982).
73) K. Seta and K. Naito, J. Chem. Thermodyn. **14**, 937 (1982).
74) T. Matsui and K. Naito, Netu Sokutei **15**, 27 (1988).
75) V. K. Clusius, P. Franzosini, U. Piesbergen, Z. Naturforsch, Teil **A15**, 728 (1960).
76) V. A. Kirillin, A. E. Sheindlin, V. Ya. Chekhovskoi and I. A. Zhukova, High Temp. **3**, 357 and 801 (1965).
77) P. V. Gel'd, F. G. Kusenko, Izu. Akad. Nauk SSSR, Otdel, Tekh. Nauk, Met. i. Toplivv **2**, 79 (1960).
78) E. G. King, J. Amer. Chem. Soc. **80**, 1799 (1958).
79) E. G. King and A. U. Christensen, U. S. Bur. Mines Rep. Invest. **57**, 89 (1961).
80) R. L. Orr, J. Amer. Chem. Soc. **75**, 2808 (1953).
81) A. G. Alexander and O. N. Carlson, Met. Trans. **2**, 2805 (1971).

82) K. Kosuge, J. Phys. Chem. Solids **28**, 1613 (1967).
83) K. Hiraga and M. Hirabayashi, Trans. Jpn. Inst. Met. **16**, 431 (1975).
84) H. Inaba, S. Tsujimura and K. Naito, J. Solid State Chem. **46**, 162 (1983).
85) T. Matsui, T. Asano, T. Tsuji and K. Naito, Thermochimica Acta in print (1990).
86) W. Banchorndhevakul, T. Matsui and K. Naito, J. Nucl. Sci. Technol. **23**, 873 (1986).
87) W. Banchorndhevakul, T. Matsui and K. Naito, J. Nucl. Sci. Technol. **23**, 602 (1986).
88) W. Banchorndhevakul, T. Matsui and K. Naito, Thermochimica Acta. **88**, 301 (1985).
89) K. E. Frantseva and G. A. Semenov, Teplofizika Vysokikh Temperature **7**, 55 (1969).
90) Y. Takahashi, J. Nakamura and J. F. Smith, J. Chem. Thermodyn. **14**, 977 (1982).
91) V. S. Chernyeav, E. N. Shemnnkov, G. N. Shveuknn, N. V. Gelbd, Izv. Akad. Nauk SSSR, Neorg. Mat. **4**, 728 (1968).
92) S. S. Todd and K. R. Bonnickson, J. Am. Chem. Soc. **73**, 3894 (1951).
93) R. L. Orr, J. Am. Chem. Soc. **76**, 857 (1954).
94) T. Tsuji, M. Sato and K. Naito, Thermochimica Acta. in print.
95) T. Matsui and K. Naito, J. Nucl. Mater. **120**, 115 (1984).
96) T. Matsui and K. Naito, J. Nucl. Mater. **136**, 78 (1985).
97) R. H. Chang and J. B. Wagner, Jr., J. Amer. Ceram. Soc. **55**, 211 (1972).
98) H. Inaba, K. Miyahara and K. Naito, J. Chem. Thermodyn. **16**, 643 (1984).
99) K. Naito, H. Inaba and H. Yagi, J. Solid State Chem. **36**, 28 (1981).
100) H. Inaba, S. Nakashima and K. Naito, J. Solid State Chem. **41**, 213 (1982).
101) T. Tsuji, Y. Asakura, T. Yamashita and K. Naito, J. Solid State Chem. **50**, 273 (1983).
102) H. Inaba, H. Yagi and K. Naito, J. Solid State Chem. **64**, 67 (1986).
103) M. Kataoka and J. Kanamori, J. Phys. Soc. Japan **32**, 113 (1972).
104) K. Kishio, J. Shimoyama, T. Hasegawa, K. Kitazawa and K. Fueki, Jpn. J. Appl. Phys. **26**, L1228 (1987).
105) P. K. Gallaghar, Adv. Ceram. Mater. **2**, 632 (1987).
106) E. T. Muromachi, Y. Uchida, K. Yukio, T. Tanaka and K. Kato, Jpn. J. Appl. Phys. **26**, L665 (1987).
107) K. Yukio, T. Sato, S. Ooba, M. Ohta, F. P. Okamura and A. Ono, Jpn. J. Appl. Phys. **26**, L869 (1987).
108) S. G. Grader, P. K. Gallaghar and E. M. Gyorgy, Appl. Phys. Lett. **51**, 1115 (1987).
109) T. Matsui, K. Naito and S. Hagino, Proceedings of NATO Advanced Research Workshop on "Nonstoichiometric Compounds-Surfaces, Grain Boundaries and Structural Defects: p.471 (Kluwer Pub. Co., F. R. G.) 1989.
110) N. Kamegashira, T. Tsuji, T. Miyamoto and K. Naito, J. Nucl. Mater. **102**, 26 (1981).
111) T. Matsui, T. Natsume and K. Naito, J. Nucl. Mater. **167**, 152 (1989).
112) G. B. Fedorov and E. A. Smirnov, Sov. J. Atom. Energy **25**, 795 (1968).
113) P. Chiotti, V. V. Akhachinsky, I. Ansara and M. H. Rand., The Chemical Thermodyn. of Actinide Elements and Compounds. Part 5, The Actinide Binary Alloys p.196 (IAEA, Vienna, 1981).
114) Y. Takahashi, M. Yamawaki and K. Yamamoto, J. Nucl. Mater. **154**, 141 (1988).
115) L. Leibowitz, E. Veleckis and R. Blomquist, Presented at the US-Japan Joint Seminar on the High Temperature Chemistry of Current Light-Water Reactors and Advanced All-Metal Reactors, June, 1987, Tokyo, Japan.
116) R. C. Westphal, USAEC Report, AECD-3864, 1-4 (1954).
117) H. A. Saller, R. F. Dickerson, A. A. Bauer and N. E. Daniel, Battelle Memorial Institute, Report BMI-1123 (1956).
118) E. L. Francis, UKAEA Report IGR-R/R-287 (1958).
119) K. Naito, T. Tsuji, T. Matsui and A. Date, J. Nucl. Mater **154**, 3 (1988).
120) T. Matsui and K. Naito, Thermochimica Acta **139**, 299 (1989).
121) T. Matsui and K. Naito, J. Nucl. Sci. Technol. **26**, 1102 (1989).
122) J. O. A. Paschoal, H. Kleykamp and F. Thummler, Z. Metallk **74**, 652 (1983).
123) T. Fukuzawa, M. Tanaka, T. Tanabe and S. Imoto, Technol. Rep. Osaka University **34**, 219 (1984).

124) H. Kleykamp, J. Nucl. Mater. **167**, 49 (1989).
125) L. Kaufman and H. Bernstein, Computer Calculation of Phase Diagrams (Academic Press, New York, 1970).
126) M. Yamawaki, Y. Nagai, T. Kogai and M. Kanno, Thermodynamics of Nuclear Materials, 1979, IAEA, vol.1, 249 (1980).
127) S. Stølen, T. Matsui and K. Naito, J. Nucl. Mater, **173**, 48 (1990).
128) D. D. Wagman et al., The NBS tables of Chem. Thermodyn. Prop., (1982).
129) E. H. P. Cordfunke, R. J. M. Konings, G. Prins, P. E. Potter and M. H. Rand, Thermochemical Data for Reactor Materials and Fission Products., ETSN-0005-NL (1988).
130) M. V. Nevitt, J. M. Downey and R. A. Morris, AIME Trans. **218**, 1019 (1960).
131) C. B. Alcock, K. T. Jacob and S. Zador, Zirconium: Physico-Chemical Properties of its Compounds and Alloys, Atomic Energy Review, Spec. Iss. No.6 (IAEA, Vienna, 1976).
132) Hj. Matzke, J. Ottavianim De Pellotiero and J. Rouault, J. Nucl. Mater. **160**, 142 (1988).
133) T. Johnson, C. E. Johnson, C. E. Crouthamel and C. A. Seils, J. Nucl. Mater. **48**, 21 (1973).
134) C. Wagner, Z. Physik. Chem. **B11**, 139 (1930).
135) K. S. Singwi and A. Sjölander, Phys. Rev. **120**, 1093 (1960).
136) R. C. Knauer and J. G. Mullen, Phys. Rev. **174**, 711 (1968).
137) T. Tsuji, Denki Kagaku **47**, 536 (1979).
138) J. R. Manning, Diffusion Kinetics for Atoms in Crystals (Van Nostrand, Princeton, N. Y., 1971).
139) H. S. Carslaw and J. C. Jaeter, Conduction of Heat in Solids (Oxford press, Oxford) p.227 (1959).
140) J. Goldman and J. B. Wagner, Jr., J. Electrochem. Soc. **121**, 1318 (1974).
141) T. Matsui, M. Murata and K. Naito, High Temp. High Press. **19**, 111 (1987).
142) W. Weppner and R. A. Huggins, J. Electrochemi. Soc. **124**, 1569 (1977).
143) W. F. Chu, H. Rickert and W. Weppner, "Fast Ion Transport in Solids" (W. Van Gool ed.), p.182 Noth Holland Pub., Amsterdam (1973).
144) J. Crank, "The Mathematics of Diffusion", p.17, Univ. Press., London, Oxford, (1957).
145) T. Tsuji, K. Tsumura and K. Naito, J. Nucl. Mater. **138**, 215 (1986).
146) R. Dieckmann and H. Schmalzried, Ber. Bunsenges. Phys. Chem. **81**, 344, 414 (1977).
147) A. E. Paladino and W. D. Kingery, J. Chem. Phys. **37**, 957 (1962).
148) L. Himmel, R. F. Mehl and C. E. Birchenall, Trans. AIME **197**, 827 (1953).
149) R. H. Chang and J. B. Wagner, Jr. J. Am. Cer. Soc. **55**, 211 (1972).
150) V. I. Izvekov, N. S. Gorbunov, A. A. B. Zakhrapin, Phys. Met. Metall. **14**, 30 (1962).
151) R. Lindner, Arkiv Kemi **4**, 381 (1952).
152) K. Hoshino and N. L. Peterson, J. Am. Cer. Soc. **66**, C202 (1983).
153) R. Lindner and A. Akerstrom, Z. Physik, Chem. N. F. **6**, 162 (1956).
154) P. Kofstad and K. P. Lillerud. J. Electrochem. Soc. **127**, 2410 (1980).
155) W. C. Hagel and A. U. Seybolt, J. Electrochem. Soc. **108**, 1146 (1961).
156) R. H. Condit, R. R. Hobbins and C. E. Birchenall, Oxid. Metals **8**, 409 (1974).
157) T. Tsuji, N. Uetake, H. Tsuchiya and K. Naito, in: Transport in Nonstoichiometric Compounds, ed. J. Nowotny (Elsevier, Amsterdam, 1982) p.139.
158) T. Tsuji, H. Tsuchiya and K. Naito, Solid State Ionics **35**, 331 (1989).
159) A. T. Howe, P. Coffin and B. E. F. Fender, J. Phys. C. **9**, L61 (1976).
160) M. Magara, T. Tsuji and K. Naito, Hyperfine Interactions, **56**, 1459 (1990).
161) M. Magara, T. Tsuji and K. Naito, to be published.
162) T. Matsui and K. Naito, J. Nucl. Mater. **135**, 149 (1985).
163) H. Furuya, unpublished work (1990).
164) A. S. Bayogln and R. Lorenzelli, Solid State Ionics **12**, 53 (1984).
165) K. W. Lay, J. Am. Ceram. Soc. **53**, 369 (1970).
166) C. Sari, J. Nucl. Mater. **78**, 425 (1978).
167) J. A. Roberson and R. A. Rapp, Trans. Met. Soc. AIME **239**, 1327 (1867).
168) J. F. Marucco, R. Tetot, P. Gerdanian, C. Picard, J. Solid State Chem. **18**, 97 (1976).
169) J. F. Baumard, Solid State Commun. **20**, 859 (1976).
170) N. Ait-Younes, F. Millot and P. Gerdanian, Solid State Ionics **12**, 437 (1984).

171) P. V. Geld and V. D. Lyubimov, Izv. Sib. Ots. Akad. Nauk SSSR, Ser, Khim. Nauk **7**, 79 (1963).
172) K. Fueki, J. Mizusaki, S. Yamauchi, T. Ishigaki and Y. Mima, Reactivity of Solids, (Proceedings of the 10th International Symposium) p.339 (1984).
173) M. Magara, T. Tsuji and K. Naito, Solid State Ionics, **40/41**, 284 (1990).
174) K. Naito, N. Kamegashira and Y. Nomura, J. Crystal Growth **8**, 219 (1971).
175) N. Kamegashira, K. Ohta and K. Naito, J. Crystal Growth **44**, 1 (1978).
176) K. Naito, N. Kamegashira and N. Fujiwara, J. Crystal Growth **45**, 506 (1978).
177) W. K. Chu, J. W. Mayer and M. A. Nicolet: Backscattering Spectroscopy, Academic Press, N. Y. (1978).
178) H. Sakai, T. Tsuji and K. Naito, J. Nucl. Sci. Technol. **21**, 844 (1984).
179) K. Naito, N. Kamegashira, T. Kondo and S. Takeda, J. Nucl. Sci. Technol. **13**, 260 (1976).
180) W. E. Boggs, R. H. Kachik and G. E. Pellisier, J. Electrochem. Soc. **112**, 539 (1965).
181) E. A. Gulbransen, Trans. Electrochem. Soc. **81**, 327 (1942).
182) R. J. Hussey, D. Caplan and M. J. Graham, Oxid. Metals **15**, 421 (1981).
183) E. J. Caule, K. H. Buob and M. Cohen, J. Electrochem. Soc. **108**, 829 (1961).
184) D. E. Davies, U. R. Evans, J. N. Agar, Proc. Roy Soc. London **A225**, 443 (1954).
185) B. Lustman, Trans. Electrochem. Soc. **81**, 359 (1942).
186) H. Sakai, T. Tsuji and K. Naito, Proc. JIMIS-3 127 (1983).
187) H. Sakai, T. Tsuji and K. Naito, J. Nucl. Sci. Technol. **22**, 158 (1985).
188) H. Sakai, T. Tsuji and K. Naito, J. Nucl. Sci. Technol. **26**, 321 (1989).
189) T. Tsuji, K. Okumura and K. Naito: High Temperature Chemistry-IV by Z. A. Munir, D. Cubicciotti and H. Tagawa Eds., The Electrochemical Society Inc. (1988) p.156.
190) P. L. Surman, Corros Sci., **13**, 113 (1973).
191) D. D. Wagman et al: Nat. Bur. Stand. Tech. Note 270-3 Washington, D. C. (1968).
192) K. Videm, 3rd Geneva Conf., vol. 8, 600 (1964).
193) D. E. Tackett, P. E. Brown and R. T. Esper, WARD-LSR (c)-134, Bettis Plant (1955).
194) D. C. Vreeland, G. G. Gaul and W. L. Pearl, Corrosion **17**, 269 (1961).
195) T. Tsuji, K. Naito and K. Ishigure, Phys. Stat. Sol. **82**, K57 (1984).
196) T. Tsuji and K. Naito, Hyperfine Interactions **57**, 2119 (1990).
197) T. Matsui, T. Hoshikawa and K. Naito, Solid State Ionics, **40/41**, 996 (1990).
198) M. Simnad and A. Spilners, Trans. AIME **211**, 1011 (1955).
199) C. A. Krier and R. I. Jaffee, J. Less-Common Met. **5**, 411 (1963).
200) K. Naito, T. Matsui and Y. Tanaka, J. Nucl. Sci. Technol. **23**, 540 (1986).
201) K. Naito, T. Matsui, H. Nakahira, M. Kitagawa and H. Okada, J. Nucl. Mater, to be submitted (1990).
202) T. Matsui, T. Yamamoto and K. Naito, J. Nucl. Mater., **173**, in print (1990).
203) T. Matsui, T. Hoshikawa and K. Naito, J. Nucl. Mater., to be submitted (1990).
204) H. Ipser, K. L. Komarek and H. Mikler Monatsh, Chem. **105**, 1322 (1974).
205) M. Magara, T. Tsuji and K. Naito, to be published
206) K. Naito, N. Kamegashira and Y. Nomura, J. Crystal Growth **8**, 219 (1971).
207) Y. Nomura, N. Kamegashira and K. Naito, J. Crystal Growth **52**, 279 (1981).
208) N. Kamegashira, K. Ohta and K. Naito, J. Crystal Growth **44**, 1 (1978).
209) N. Kamegashira, J. Mater. Sci. **14**, 505 (1979).
210) K. Naito, N. Kamegashira and N. Fujiwara, J. Crystal Growth **45**, 506 (1978).
211) E. K. Storms and J. Griffin, High Temperature Sci. **5**, 251 (1973).
212) T. Matsui, T. Fujita, K. Naito and T. Takeshita, J. Solid State Chem. **88**, in print (1990).
213) H. Blank and C. Ronchi, Acta Cryst. **A24**, 657 (1968).
214) F. Grønvold, J. Inorg. Nucl. Chem. **1**, 357 (1955).
215) T. Matsui, M. Murata and K. Naito, in Chemical Sensors, Proceedings of the First Intern. Meeting on Chemical Sensors, ed. T. Seiyama (Tokyo, Kodansha) p.320 (1983).